

**Development and Characterization of a Custom Syringe Pump for Delivery of Picoliter
Range Liquid Volumes**

BY

BRIAN EDWARD KUNZER

B.S. University of Illinois at Chicago, Chicago, 2004

B.S. University of Illinois at Chicago, Chicago, 2005

THESIS

Submitted as partial fulfillment of the requirements
for the degree of Master of Science in Mechanical Engineering
in the Graduate College of the
University of Illinois at Chicago, 2011

Chicago, Illinois

Defense Committee:

Laxman Saggere, Chair and Advisor

Thomas Royston

Scott Shippy, Chemistry

ACKNOWLEDGEMENTS

This research has been supported by NSF grants 0449352 and 0938072. I would like to express my gratitude to my committee members, Thomas Royston, Scott Shippy, and my advisor Laxman Saggere, for their time and valuable advice.

I would like to thank my labmates including Sandeep Krishnan, Chris Pelzmann, Marina Dubinskaya, Shushi Kabu, and Sasidhar Madugula for their support, advice, and friendship. I would especially like to acknowledge Sandeep Krishnan and Chris Pelzmann for being instrumental in providing research support and brainstorming sessions.

I would also like to acknowledge my family, especially my parents who gave me enough freedom to explore and imagine. Finally, I convey my profound appreciation to my wife, Courtney Leigh Beisel, who has been my greatest supporter and utmost motivator.

TABLE OF CONTENTS

Acknowledgements.....	ii
Table of Contents.....	iii
LIST OF TABLES.....	v
LIST OF FIGURES.....	vi
Chapter 1 - Introduction.....	1
1.1 Background and Motivation.....	1
1.2 Objectives.....	2
1.3 Approach.....	2
1.4 Technical Challenges.....	3
1.5 Thesis Organization.....	3
Chapter 2 - Dispenser Design & Development.....	5
2.1 Review of Existing Dispenser Technology.....	5
2.2 Design Considerations of the Bench-Top Dispenser System.....	6
2.3 Syringe Pump Based Dispenser.....	8
2.4 Dispenser Prototype.....	10
2.5 Configuring the Dispenser System for Delivery to the Tissue.....	12
Chapter 3 - Determination of Dispensed Volume & Flow Rate Through.....	14
Experimental & Theoretical Methods.....	14
3.1 Existing Methods to Measure Volumes and Flow Rates.....	14
3.2 Experimental Measurements.....	17
3.2.1 Calibrating the New Focus® Picomotor Displacements and Velocities.....	17
3.2.2 Volume Characterization for Input Displacement using Meniscus Tracking.....	22
3.2.3 Flow Rate Characterization for Input Velocity Using Meniscus Tracking.....	29
3.2.4 Flow Rate and Volume Characterization Using Plunger Tracking: Equivalence to Meniscus Tracking and Validation of Incompressibility.....	33
3.2.5 Flow Rate Dependence on Insertion into Agarose Gel.....	35
3.2.6 Summary of Results from Experimental Measurements of Hydrodynamic Parameters	39
3.3 Theoretical Modeling of Fluid Conduits in the Dispenser.....	41
3.3.1 Introduction to Hydraulic Circuit Analysis.....	42

3.3.2 Full Model of the Syringe Pump Dispenser and Validation of the Liquid Incompressibility Assumption	44
3.3.3 Simplification of the Model	50
3.3.4 Formulating a Predictive Model of Flow Rates for the Syringe Pump Dispenser with Interchangeable Dispensing Capillaries.....	52
Chapter 4 - Determination of Concentration Profiles Through Experimental.....	54
& Theoretical Methods	54
4.1 Existing Methods to Measure Concentration Profiles	55
4.2 Experimental Technique to Measure Concentration Profiles	56
4.2.1 Basic Theory	56
4.2.2 Experimental Setup and Method.....	57
4.2.3 Image Processing and Conversion of Images into Concentration Profiles.....	62
4.2.4 Results and Discussion	66
4.3 Theoretical Modeling of Concentration Profiles in Agarose Gel	69
4.3.1 Model Space, Elements Used, and Governing Equations.....	69
4.3.2 Physical Properties, Boundary Conditions, and Velocity Input	71
4.3.3 Mesh and Element Refinement.....	74
4.3.4 Results and Discussion	75
4.3.5 Experiment-Model Correlation.....	77
Chapter 5 - Conclusions & Future Work	81
5.1 Conclusions.....	81
5.2 Suggestions for Future Work & Designs	82
CITED LITERATURE	85
APPENDIX.....	90
A.1 Summary of Hydraulic/Electric Circuit Analogy	90
A.2 MATLAB code to run hydraulic circuit analysis.....	91
A.1.1 Full Hydraulic Circuit Model of the Syringe Pump Dispenser.....	91
A.2.2 Simplified Hydraulic Circuit Model of the Syringe Pump Dispenser	93
A.3 MATLAB code to run image processing and analysis	94
VITA.....	99

LIST OF TABLES

TABLE	PAGE NO.
Table I. EVALUATION OF VARIOUS LIQUID VOLUME AND FLOW RATE MEASUREMENT TECHNIQUES AT THE PICOLITER-NANOLITER SCALE.....	16
Table II - PROPERTIES USED IN THE FEA MODEL.....	71
Table III - SUMMARY OF THE ELECTRICAL/HYDRAULIC CIRCUIT ANALOGY [47, 48]	90

LIST OF FIGURES

FIGURE	PAGE NO.
Figure 1 - Breakdown of major components of a fluid dispensing system	6
Figure 2 - (Top) Custom-built syringe pump dispenser, (Bottom Right) syringe connection to dispensing capillary, (Bottom Left) Plunger holding bracket for actuator interface with syringe barrel.	11
Figure 3 - LabVIEW GUI for controlling the actuator, and hence, the plunger movement. Displacement is controlled by inputting a distance and velocity s controlled by setting a velocity. Execution of the planned displacement is then executed by pressing the “Move +” or “Move -” to drive the actuator in the desired direction.	12
Figure 4 - Configuration of the syringe pump dispenser for top side delivery to the tissue in the MEA recording system.	13
Figure 5 - Configuration of the syringe pump dispenser for bottom side delivery to the tissue in the MEA recording system (Cross-sectional view). Chemical species may be introduced through the bottom of the MEA through commercially available perforated MEAs or through custom designed MEAs with thru-hole access.	13
Figure 6 - Measured displacements versus commanded displacements for loaded and unloaded scenarios for the New Focus® actuator. The actuator showed high accuracy and repeatability for both scenarios (error bars plot one standard deviation).	19
Figure 7 - (Left) One drive cycle of the velocity for the New Focus® actuator showing the initial reverse and then forward drive of the actuator. The net displacement of this cycle is ~30 nm in the forward drive direction. (Right) Several drive cycles at a frequency of 10 cycles/second. This is the control parameter that is input into the control interface for the New Focus® actuator.	20
Figure 8 - A calibration plot of the New Focus® actuator's measured velocity for a given input of cycles/second in the control interface.	21

Figure 9 - A comparison of measured velocities for varied input displacements. The New Focus® actuator showed no velocity dependence with actuator displacement. 22

Figure 10 - Illustration of how the volume is measured in the meniscus tracking technique. 23

Figure 11 - The relation between the actuator, plunger, and the volume dispensed..... 23

Figure 12 - Experimental setup of the meniscus tracking technique. 24

Figure 13 - The measured volume (diamond markers) versus the input actuator displacement. A linear fit (equation shown) showed high correlation with the expected calculated volume (square markers). This indicates almost no fluid leakage or actuator/plunger misalignment. 27

Figure 14 - The measured volume (diamond markers) versus the input actuator displacement. A linear fit (equation shown) showed high correlation with the expected calculated volume (square markers). A volume measurement as small as 42 pL was possible with this capillary and the New Focus® actuator. 27

Figure 15 - The measured volume (diamond markers) versus the input actuator displacement. A linear fit (equation shown) showed high correlation with the expected calculated volume (square markers). A volume measurement as small as 9.8 pL was possible with this capillary and the New Focus® actuator. 28

Figure 16 - A calibration plot of the measured flow rate (red markers) in a 152, 99, 75, and 52 μm inner diameter capillary for the input velocity control parameter of the New Focus® actuator. A linear fit (equation shown) of the measured flow rates was achieved for the 152, 99, 75 μm capillaries. However, the slope of the linear plots varied according to the inner diameter of the capillary and measured flow rates were much smaller than the expected theoretical values (blue markers) that were based off the calibration plot in Figure 15. The 52 μm capillary was not linear, possibly due to leakage in the dispensing system. 32

Figure 17 - Comparison between volume measurement techniques for different input volumes. All three methods produced similar results, thus showing the equivalence between the techniques for measuring volumes..... 34

Figure 18 - Comparison between flow rate measurement techniques for different input velocities. All three methods produced similar results, thus showing the equivalence between the techniques for measuring flow rates. 35

Figure 19 – (Left) Experimental setup for measuring the flow rates through plunger tracking while dispensing in the gel. (Right) A platform was used to hold the gel and allow a capillary to be placed adjacent the bottom of the gel or be inserted into the gel. 37

Figure 20 - Plot of the measured flow rate versus the input velocity for three different scenarios: a 75 μm capillary dispensing into air or the same capillary is placed adjacent or fully inserted into an agarose gel. All three scenarios produced similar results. 38

Figure 21 - Plot of the measured flow rate versus the input displacement for three different scenarios: a 75 μm capillary dispensing into air or the same capillary is placed adjacent or fully inserted into an agarose gel. All three scenarios produced similar results for a given displacement, but larger volume injections seemed to effect the flow rate for the gel scenarios. 39

Figure 22 - A schematic on how a fluid conduit can be modeled as an electric circuit. 44

Figure 23 - Image of the fluid path in the syringe pump dispenser 45

Figure 24 - Equivalent circuit of the syringe pump dispenser 45

Figure 25 - A plot of the output flow rate (solid lines) for dispensing capillaries of different inner diameter all with the same input flow rate (circles). The flow rate varies sharply with decreasing inner diameter of the dispensing capillary. 48

- Figure 26 - A plot of the output flow rate (solid lines) for dispensing capillaries of different length all with the same input flow rate (circles). The flow rate varies only with a large increase in the length of the dispensing capillary. 49
- Figure 27 - A plot of the output flow rate (solid lines) for the syringe plunger at different positions (length of barrel conduit) all with the same input flow rate (circles). The flow rate varies very little over the range of the length of the barrel conduit. 50
- Figure 28 - Simplification of the complete dispenser circuit in Figure 26 to the circuit elements that have the largest effect on the system. 51
- Figure 29 - A plot, using the simplified model of Figure 28, of the output flow rate (solid lines) for dispensing capillaries of different inner diameter all with the same input flow rate (circles). The flow rates obtained for this simplified model were nearly identical to the flow rates from the complete model. 51
- Figure 30 - A plot of the slopes obtained in Figure 18 for flow rate dependence on the hydraulic resistance of the capillary. The curve fit a power function. 53
- Figure 31 - Illustration of the principle of the Beer-Lambert Law. An incident light beam will undergo a loss in intensity proportional to the concentration of absorbers in a medium of known thickness. 57
- Figure 32 – (Left) Experimental setup for the calibration of the microscope camera and determining the absorption coefficient, α . (Right) The optics assembly included the fiber optic from the lamp source aligned with the filters and collimating lens. 58
- Figure 33 - The calibration curve that determines the absorption coefficient, α , per unit length. The concentration was varied and the drop in intensity was measured. 59
- Figure 34 - Image of the entire experimental setup for capturing injection profiles in agarose gel during syringe pump dispenser operation. 60

Figure 35 - Closeup of the cuvette containing gel with the dispensing capillary inserted into gel and the capillary tip in the collimated light path..... 61

Figure 36 - Representative image of the videos recorded during dispensing. Notice the blue dye profile developing at the end of the capillary inside the gel. The outer diameter of the capillary is 150.5 μm 62

Figure 37 - Illustration of the space that is captured for image processing and conversion to concentration values..... 63

Figure 38 - (Left) Schematic of the concentration profile is forming at the end of the dispensing capillary in the gel. Incident light will pass through this profile formed by an N number of concentration shells that is the same number of pixels along the z-axis that the profile is imaged on. (Right) The light path ($Z_{k,l}$) varies through each ring of the concentration shell, but can be determined through trigonometry if a symmetric profile is assumed. 64

Figure 39 - Experimentally determined concentration profiles along the axial direction is plotted as a function of time (0.1s time steps). The slowest injection speed resulted in the farthest penetration into the gel even though the same volume was injected for each trial. 67

Figure 40 - Images captured during recording of multiple 1.66 nL injections from the dispensing capillary. (Top) Using an injection velocity of 378.2 $\mu\text{m/s}$, reflux occurs, resulting in volume that does not contribute to the profile at the end of the dispensing capillary. (Bottom) Using an injection velocity of 37.8 $\mu\text{m/s}$, results in a dispensing profile with significantly less reflux. The outer diameter of the capillary is 150.5 μm 68

Figure 41 - The space being modeled is entirely in the gel and is the same space that was analyzed during the experiments (see Figure 37). 70

Figure 42 - Illustration of the model space with the applied initial and boundary conditions. There are a total of two initial conditions applied to the model space, one each for each governing equation, and two boundary conditions applied to each of the five boundaries. 72

Figure 43 - An unstructured triangular mesh was used to cover the 150 X 150 μm model space. 74

Figure 44 - A 2-D contour plot of the concentration in the model space for selected times. Although, initially asymmetric, the profile quickly becomes symmetric. The slow diffusion rate on this timescale is evidenced by the steep concentration gradient along the growing boundary. 76

Figure 45 - A plot, obtained from the FEA model, of the concentration profiles along the axial centerline at the final time step ($t=3.5\text{s}$) for different dispenser input velocities (resulting in different injections velocities). Because the same volume was delivered during the single injected pulse, the same concentration profile was obtained for all injection velocities. 77

Figure 46 - A plot of the concentration profiles along the axial centerline at the final time step ($t=3.5\text{s}$) for different dispenser input velocities (resulting in different injections velocities). An average of the results obtained in Figure 45 from the FEA model is compared with the results obtained from the experiments and imaging processing. The lower injection velocities profiles from the experiment were much closer to the result obtained from the model. 78

Figure 47 - Plots of the concentration profile obtained through the FEA model. The convection dominates the progression of the profile, since almost all of the penetration into the gel occurs during dispensing. The contribution of only the diffusion can be seen in the later time steps after dispensing stops. 79

CHAPTER 1 - INTRODUCTION

The work of this thesis is closely tied to an ongoing larger research project involving a drug delivery system being developed in the Microsystems and Devices Laboratory (MDL) at the University of Illinois at Chicago. This larger research involves presentation of a controlled volume of chemical species, particularly native neurotransmitters, to neural tissue. The specific goals of this thesis will focus on design, construction, and characterization of a bench-top dispenser for discrete volume delivery of these species.

1.1 Background and Motivation

In the MDL, researchers seek to investigate the feasibility of stimulating retinal neurons by chemicals to regain visual acuity lost as a result of photoreceptor degenerative diseases. Stimulation by chemical delivery represents an alternative approach to more conventional electrical based stimulation. For this investigation, an important tool is a bench-top fluid dispenser device that can controllably deliver small discrete chemical volumes on demand. Since a commercially available delivery device does not adequately meet the delivery requirements of this project, a primary goal of this thesis is to build a bench-top dispenser with appropriate dispensing characteristics that meet the above mentioned specifications. Further, both experimental and analytical techniques need to be developed and applied to characterize the dispenser. This characterization must include both hydrodynamic and mass transport considerations. The hydrodynamic parameters of interest are the dispensed volume and flow rate from the dispenser. The mass transport parameters is the density of the chemical species distribution after injection, otherwise known as the injected concentration profile. Since chemical species need to reach a critical threshold concentration in order to transmit a signal or reach a

therapeutic level, the concentration profile provides an indication of the volume being stimulated in the tissue.

1.2 Objectives

There are two primary objectives of this thesis that can be summarized as follows:

- 1) Design and construct a bench-top dispenser that is flexible enough to be used as an investigative tool, yet has high accuracy and repeatability at the nanoliter and picoliter scales.
- 2) Characterize and validate the performance of the dispenser system via experimental and analytical techniques. The latter objective is further divided into using experimental and analytical techniques to characterize either hydrodynamic parameters, such as dispensed volume and flow rate, or mass transport parameters, such as the ejected time developing concentration profile in the target media.

1.3 Approach

The adopted approach to achieve the design and construction objective is to construct a custom syringe pump driven by a precision actuator with interchangeable capillaries as delivery ports. Optical microscopy utilizing a combination of meniscus tracking and syringe plunger tracking will be used to verify dispensed volumes and flow rates with commanded volumes and flow rates. Validation and further insight to calibration of these hydrodynamic parameters will use hydraulic circuit theory to develop a circuit model of all flow components and paths. When testing and characterizing the mass transport parameters, optical microscopy will be used to image ejected dye profiles within agarose gel and convert pixel intensity values to absolute concentration values via application of the Beer-Lambert Law. A finite element model (FEM) of the mass transport during ejection, will then be compared to the experimentally determined

concentration profiles to reveal further relationships between controlled dispenser inputs and resulting profiles.

1.4 Technical Challenges

The challenges associated with the design and construction of the bench-top dispenser is largely attributed to the task of dispensing nanoliter and picoliter liquid volumes repeatedly on demand. Such minute volumes will be easily lost in a dispenser that has even small leaks. Also, adding to this challenge is the small diameter ($<100\ \mu\text{m}$) conduits that inherently cause large pressure drops in the system, requiring a robust fluid driving system to deliver a high amount of pressure (force with the driving mechanism). Yet, the driving mechanism must also be sensitive enough to accurately deliver a minuscule volume reliably. Finally, the dispenser must be flexible in delivering volumes from numerous ports in an arbitrary array from a variety of different port inner diameters for proper investigation on their effect in delivering species to tissue.

For the testing and characterization, the challenges arise from measuring nanoliter and picoliter volumes, nanoliter per second scale flow rates, and absolute mM concentration profiles in the target media. At these scales, imaging techniques are challenging, but are made even more difficult by tracking liquid motion in either conduits or target media, such as aqueous solutions, gels, and tissues. Hence, experimental setups and procedures must be crafted, with these factors in mind, to accurately measure the parameters of interest. Applied theoretical techniques can then be used to validate experimental procedures.

1.5 Thesis Organization

The rationale behind arrival at these approaches and their development and applications are described in the subsequent chapters. Chapter 2 will discuss the design, development, and

construction of the bench-top dispenser. Hydrodynamic related experimental testing and development of a theoretical model for the dispenser are then discussed in Chapter 3. Next, Chapter 4 details an experimental approach for determining ejected profiles in agarose gel that is then compared to a finite element model developed to provide more insight to the behavior of the concentration profile formation. Finally, Chapter 5 discusses conclusions drawn from the research and suggests improvements and future work for these approaches.

CHAPTER 2 - DISPENSER DESIGN & DEVELOPMENT

The need for a bench-top dispenser is first established with a review of existing dispenser technology. This is followed by a discussion of design considerations and then selection of dispenser components based on these considerations. Finally, a syringe pump style bench-top dispenser prototype is constructed and how it addresses design considerations is discussed.

2.1 Review of Existing Dispenser Technology

To approach the above mentioned aim, the engineered delivery device must meet several broad specifications, such as fast (<1 second) discrete dispensing over a wide range of small volumes (picoliters to nanoliters), high accuracy, and excellent repeatability. Additionally, the dispenser must be leak-proof and robust enough to withstand the high pressures and forces involved in dispensing through small flow lines (<100 μm in cross-sectional diameter).

While a wide variety of commercially available pumps and dispensers exist in the market, only a few specialize in dispensing at this scale. The Picospritzer (available from Parker based in Cleveland, OH) is one such dispenser that utilizes a pressurized pneumatic system with a fast acting solenoid valve to deliver pulses of pressure to a micropipette filled with the drug to be delivered. The control parameters of the Picospritzer are the applied pressure and the opening duration of the solenoid valve; however, neither parameter lends itself to be independently related to the total volume being dispensed from the device. Also, the geometry of the micropipette (length and cross-sectional area) must be accounted for when determining the dispensed volume. Indeed, one must separately calibrate dispensed volumes for each micropipette of different geometry based on input control parameters.

Micro-syringe pumps are another type of dispenser used for nanoliter and picoliter scale dispensing. Several companies (Cole-Parmer, Harvard Apparatus) offer syringe pumps, yet these pumps are not designed for fast, discrete volume dispensing and often require minutes of running time before a regular flow rate is achieved. LabSmith offers a stepping microsyringe pump, but has a dispensing resolution of only 5~10 nL. World Precision Instruments (WPI) also has a micro-stepping syringe pump (UMP3 Microsyringe Injector) available. Yet with a bottom motor step resolution of 3.175 μm (a resolution of 580 pL with a 1 μL syringe), picoliter scale dispensing would be unreliable at best, and in fact, the manufacturer recommends to “allow the motor to step forward a good number of steps to prevent errors in volume injecting” [1].

Currently, a commercially available delivery device does not adequately meet the delivery requirements of this project. Also, while some chip based syringe pumps have been suggested in the literature [2-4], they do not allow for rapid prototyping of delivery configurations.

2.2 Design Considerations of the Bench-Top Dispenser System

Any fluid dispensing system can be decomposed into three main subcomponents: a fluid driving system (e.g. a transducer or pressurized source), a reservoir, and a dispensing port (Figure 1).



Figure 1 - Breakdown of major components of a fluid dispensing system

Thus, each of these subcomponents must be chosen so that they function together while accomplishing the design objectives. The design objectives for each component are as follows:

Fluid Driving System

- Must accurately control the volume and flow rate dispensed (for linear actuator, typically requires sub-micron displacement resolutions to dispense picoliter range volumes)
- Must dispense volumes quickly (< 1 second)
- Must allow for control of changing volume or flow rate quickly and easily
- Must have a user interface for control
- Must be adaptable to the fluid reservoir
- Must overcome forces involved with dispensing liquid through small flow lines ($< 100 \mu\text{m}$)

Reservoir

- Must contain a sizable volume ($\sim 1 \mu\text{L}$)
- Must be leak-proof under high pressure (10~1000 psi)
- Must be adaptable to the fluid driving system and the dispensing port
- Must be of small tubular inner diameter ($< 1 \text{ mm}$) to reduce force requirements of actuator

Dispensing Port

- Must be approximately $100 \mu\text{m}$ or less in inner diameter to limit molecular diffusion out of port
- Must be interchangeable or adjustable to allow for ports of different diameters and arrangements without costly reiterations (e.g. microchannels by microfabrication) [2-7]

- Must be leak-proof under high pressure (10~1000 psi)
- Must be adaptable to the fluid reservoir and micro-electrode array (MEA) recording equipment for electrophysiological data acquisition

2.3 Syringe Pump Based Dispenser

With these objectives in mind, a precision actuator driving a syringe with adaptable, interchangeable capillaries was selected for the bench-top dispenser. The main advantage of using a syringe pump at the heart of the dispenser is the direct, often linear relationship between input parameters (actuator displacement and velocity) and dispensing parameters (dispensed volume and volumetric flow rate). Assuming no leakage and liquid incompressibility in a syringe pump delivery system, conservation of mass dictates that the change in volume displaced by a plunger of the syringe pump and the time rate of change of this volume is equal to the volume dispensed and volume flow rate at the end port of the dispensing system. Other advantages of syringe pumps include the ability to handle quick, repeatable, on/off cycles well and no power dissipation during the non-dispensing off state.

Actuator Selection

After a market review of commercially available actuators, the 8301 Picomotor Actuator (New Focus Inc.) was selected for the fluid driving system. This actuator has the following specifications:

- 30 nm step resolution
- 80 nm resolution position feedback optical encoder
- Variable speed control
- 22 N stall force

- LabVIEW® graphic user interface control of displacement and velocity
- Simple integration of multiple, independently controlled actuators

The driving principle behind the actuator is a piezoelectric element that deforms a gripping drive element that makes contact with a threaded drive shaft. The threaded drive shaft rotates, but makes point contact with a spring biased translation stage to drive the stage linearly in the direction of the drive shaft movement. The gripping drive element allows for continued movement through a cycle of slow high friction forward drive mode and a fast low friction reverse mode to reset the position of the drive element on the threaded drive shaft for a net displacement of 30 nm. The cycle repetition speed (cycles/second) can be varied to thereby control the velocity of the shaft.

Syringe as the Reservoir

With a syringe as the reservoir, the syringe plunger allows for easy adaptation with the actuator to complete the fluid driving system. The syringe selected for the dispenser was the 1801 RN 10 μL model from Hamilton Company with the following specifications:

- Gastight syringe rated up to 1000 psi
- Inner barrel/plunger diameter of 460 μm
- Inner barrel volume of 10 μL with zero dead volume
- Removable hub attachment for needles of various sizes (gauges)
- Reinforced plunger rod to reduce bending

Capillaries as Delivery Ports

Fused silica capillaries (FSCs), available from Polymicro Technologies, were selected as the delivery ports for the dispenser with fittings from LabSmith Inc. for providing the connection between the syringe needle and the capillary. These capillaries have the following specifications:

- Wide assortment of inner diameters (2~700 μm)
- Outer diameters available in 850, 360, 150, or 90 μm
- Polyimide coated capillaries are flexible/bendable
- Capillaries can be cut to any length
- Capillaries are transparent if polyimide is burned off
- Capillary end tips can be ground/polished/etched for modified tip geometries
- LabSmith fittings allow for 1000 psi leak-proof connections

Thus, the three components selected, the actuator, syringe, and capillaries, meet or exceed the design objectives. The following section will describe their arrangement into a dispenser prototype.

2.4 Dispenser Prototype

The syringe, actuator, capillaries, and fittings are aligned and mounted using various hardware (Thor Labs Inc., Newport Corporation) (Figure 2). Special attention is made to axially aligning the motor shaft with the syringe plunger. The actuator-plunger interface uses a custom machined adjustable slot clamp that connects the plunger rod and the translation stage of the actuator. The syringe and actuator are also mounted to the same rail for easy alignment between them and positioning of the dispenser as a whole.

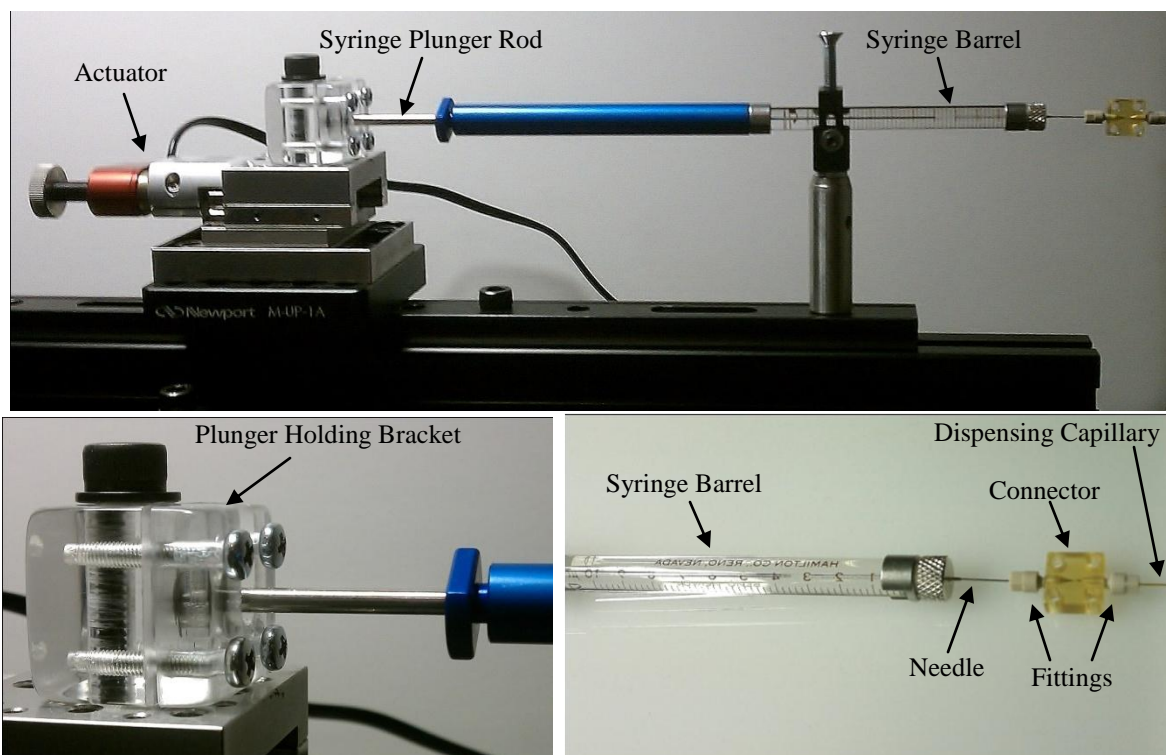


Figure 2 - (Top) Custom-built syringe pump dispenser, (Bottom Right) syringe connection to dispensing capillary, (Bottom Left) Plunger holding bracket for actuator interface with syringe barrel.

The capillary fittings work for all capillaries of 360 μm outer diameter. Although, it is possible to use capillaries of outer diameter smaller than 360 μm if they are inserted and glued into a 360 μm outer diameter capillary with an appropriately sized inner diameter. Two separate capillaries can be connected with two fittings, one for each capillary, and a connector. The connection between the syringe and the dispensing capillary can be made using a 28 gauge needle, with nominal inner and outer diameters of 165 μm and 356 μm , inserted into one of the capillary fittings and then fastened to a capillary connector.

Thus, the syringe pump is now capable of delivering an independent flow of discrete drug volumes to a variety of media, such as in vitro tissue, agarose gel, and aqueous solutions. This can be accomplished by simply inserting the delivery capillary with chosen inner diameter, to the desired media.

The actuator in the bench-top dispenser, and in turn the plunger movement, is controlled through a LabVIEW (National Instruments Corp.) graphic user interface (Figure 3, code provided by NewFocus Inc.) that allows input of both displacement (30 nm resolution) and frequency of 30 nm steps (cycles/second, control of velocity). The actuator/plunger may be driven in either forward or backwards directions.

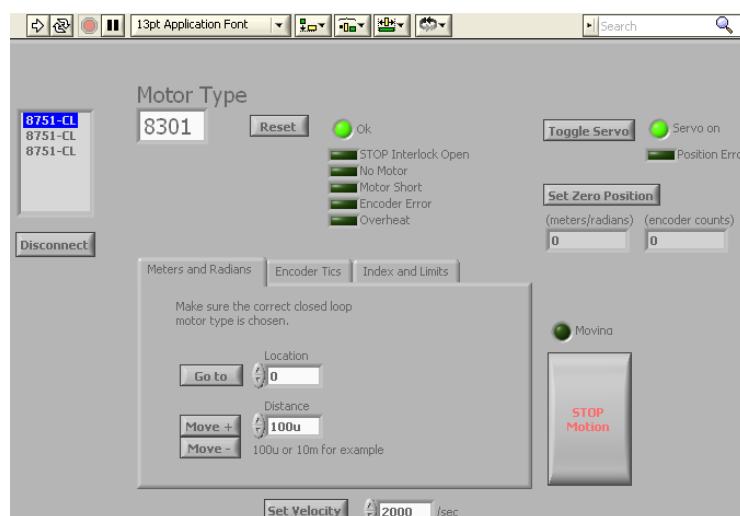


Figure 3 - LabVIEW GUI for controlling the actuator, and hence, the plunger movement. Displacement is controlled by inputting a distance and velocity is controlled by setting a velocity. Execution of the planned displacement is then executed by pressing the “Move +” or “Move -” to drive the actuator in the desired direction.

2.5 Configuring the Dispenser System for Delivery to the Tissue

The interface between the syringe pump dispenser and micro-electrode array (MEA) recording equipment is illustrated in Figures 4 and 5. The chemical may be delivered from either the top side of the MEA (Figure 4) or from the bottom side (Figure 5). It is important to note that delivery to the bottom side of the MEA may require additional modifications such as a custom adaptor plate or a modified or custom built MEA that allows fluid access from the bottom. Additionally, multiple dispenser units may be used to produce a multi-port dispensing array.

Dispensing capillaries may be placed in fixed relation to each other by bundling a group of capillaries together or by using a custom adaptor plate that will hold the capillaries in place.

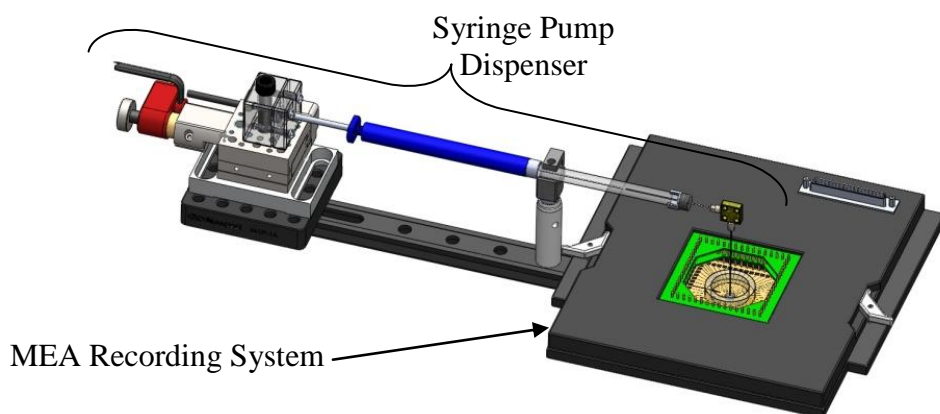


Figure 4 - Configuration of the syringe pump dispenser for top side delivery to the tissue in the MEA recording system.

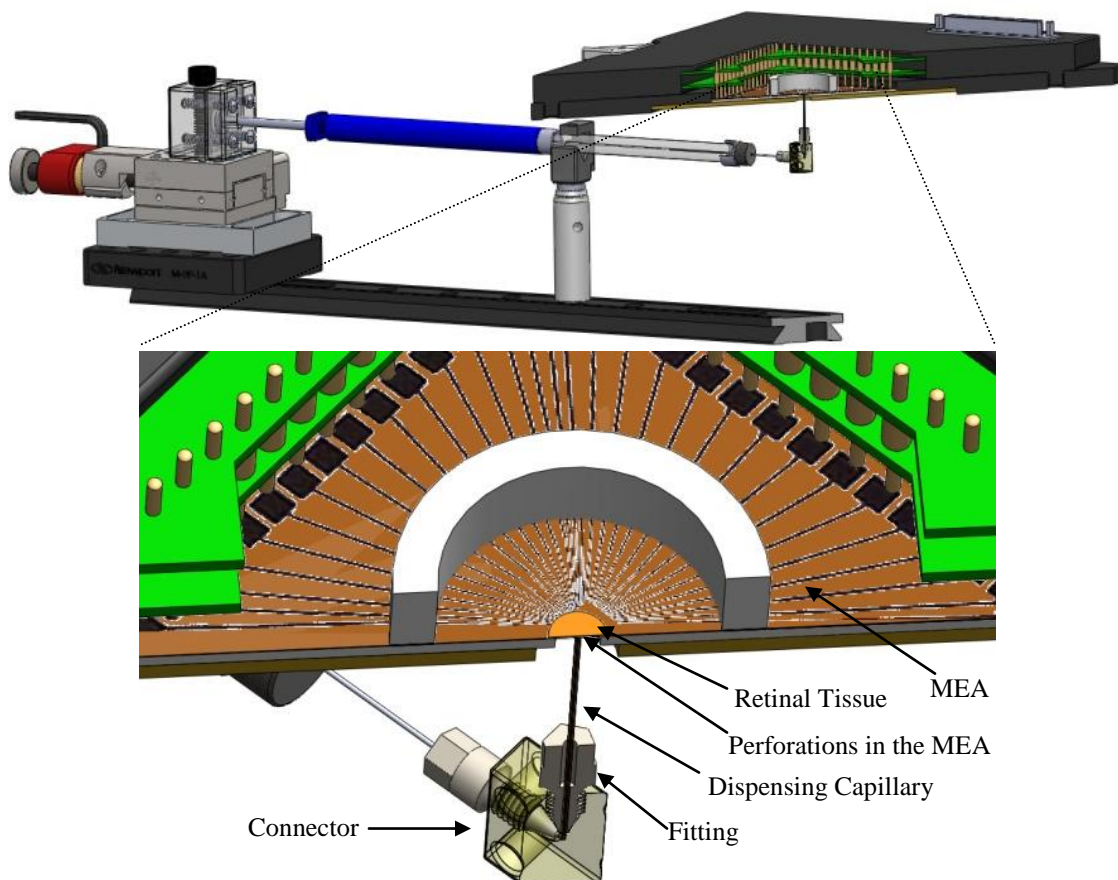


Figure 5 - Configuration of the syringe pump dispenser for bottom side delivery to the tissue in the MEA recording system (Cross-sectional view). Chemical species may be introduced through the bottom of the MEA through commercially available perforated MEAs or through custom designed MEAs with thru-hole access.

CHAPTER 3 - DETERMINATION OF DISPENSED VOLUME & FLOW RATE THROUGH EXPERIMENTAL & THEORETICAL METHODS

This chapter discusses experimental and analytical techniques for measuring and determining hydrodynamic parameters with the goal of calibrating the dispenser input displacements and velocities with the output measurements. Testing and characterization must be done to ensure the accuracy and repeatability of the dispensed volume and flow rate. A review of several different experimental methods for measuring liquid flow rates and volumes at the nanoliter and picoliter scale is first presented as an overview.

After actuator displacements and velocities are confirmed and calibrated, experimental techniques involving both non-contact and contact based methods are used to measure the dispensed volume and flow rate. These measurements are made for both scenarios when the dispensing capillary is either dispensing in a miscible or immiscible medium to investigate liquid-air or liquid-liquid interface effects, if any. The flow rate dependence on insertion into tissue model agarose gel is also investigated.

Finally, a theoretical model based on hydraulic circuit analysis is developed to reveal insight of the flow rate dependence on compliance in the system. The resulting analysis allows for the prediction of flow rates based on actuator inputs and the inner diameter and length of attached dispensing capillaries.

3.1 Existing Methods to Measure Volumes and Flow Rates

Several methods exist in the literature for experimentally measuring both these parameters for dispensing liquids. These methods can be divided into contact and non-

contact based techniques, where contact refers to the dispensed liquid coming into contact and mixing with another miscible liquid.

Non-contact techniques include measuring the size of dispensed droplets or of a displaced meniscus within a delivery tube through light microscopy [2-4, 8-21], fluorescence microscopy [22, 23], or capacitance [5, 24-27] measurements. However, these techniques, due to not actually dispensing and mixing the liquid volume into the target, suffer from the uncertainty of capturing different hydrodynamic effects as contact techniques.

Contact techniques include gravimetric (mass difference) [28-34], velocimetry (particle tracking) [31], pH change [32], flow rate meter [7, 8, 33-35], and fluorescence [28, 36-38] measurements. The advantages and disadvantages of each technique are summarized in Table 1.

Also, proper analysis of a syringe pump delivery system can lead to a predictive model for hydrodynamic parameters, such as volume and flow rate, in relation to input parameters such as plunger displacement and velocity. Since, the delivery conduits will be approximately 100 microns or less, the assumption of laminar flow for aqueous flow is valid even for extreme conditions of high velocities. While the study of laminar flow in conduits have been well studied, the well known theory of Hagen-Poiseuille flow only applies to steady state flows and is not applicable to short discrete volume dispensing or pulsed flow [39]. There is also a need to develop a simple predictive model for the delivery parameters and validate the model with appropriate testing methods.

Table I. EVALUATION OF VARIOUS LIQUID VOLUME AND FLOW RATE MEASUREMENT TECHNIQUES AT THE PICOLITER-NANOLITER SCALE

Measurement Technique	Advantage	Disadvantage
Non-Contact Based		
Microscopy-Based Measurement of Droplet Size [8-16, 21]	<ul style="list-style-type: none"> • Technically simple • Highly accurate 	<ul style="list-style-type: none"> • Requires dispensing into gas or other immiscible medium • Evaporation effects if gas-liquid interface
Microscopy-Based Measurement of Meniscus Displacement In Delivery Tube[2-4, 17-20]	<ul style="list-style-type: none"> • Technically simple • Highly accurate • Reduced evaporation 	<ul style="list-style-type: none"> • Requires dispensing into gas or other immiscible medium • Evaporation effects if gas-liquid interface
Capacitance-Based Measurement of Meniscus Location [5, 24-27]	<ul style="list-style-type: none"> • Easy to integrate on or off chip • Can provide real-time feedback to a dispenser control system 	<ul style="list-style-type: none"> • Must account for evaporation in open wells • Meniscus tracking requires dispensing into gas or other immiscible medium
Contact Based		
Gravimetric [28-34]	<ul style="list-style-type: none"> • Technically simple (change in mass measurement) 	<ul style="list-style-type: none"> • Must isolate dispenser from mass balance • Must account for evaporation • Poor sampling rate due to stabilizing time of scale
Particle Imaging Velocimetry (PIV) [31]	<ul style="list-style-type: none"> • Excellent for visualizing velocity field 	<ul style="list-style-type: none"> • No known method of determining a dispensed volume • Requires appropriate tracers
pH Change [32]	<ul style="list-style-type: none"> • Adaptable to most dispensing systems by sampling target chamber 	<ul style="list-style-type: none"> • Requires mixing of target chamber • Must account for evaporation • Poor sampling rate due to mixing time
Flow Rate Meters [6, 7, 33-35]	<ul style="list-style-type: none"> • Easy to integrate on or off chip • Can provide real-time feedback to a dispenser control system 	<ul style="list-style-type: none"> • Have limited resolution or sampling rate
Fluorescence Microscopy [28, 36-38]	<ul style="list-style-type: none"> • Adaptable to most dispensing systems by examining dispensing port 	<ul style="list-style-type: none"> • No known method of determining a dispensed volume • Require appropriate dyes or tags

3.2 Experimental Measurements

Several experimental techniques were carried out to measure the volumes and flow rates dispensed from the dispenser given input parameters to the control program and the media to which the volume is delivered. The techniques included unloaded displacement and velocity confirmation, meniscus tracking, plunger tracking, and flow rate dependence on capillary insertion into gel.

3.2.1 Calibrating the New Focus® Picomotor Displacements and Velocities

Before any volume or flow rate measurements are taken, it is important to ensure that the actuator is behaving as expected. In other words, a commanded displacement or velocity input to the control program is closely matched to a measured displacement or velocity output. In this way, any error in measuring volume or flow rate will have at least a basis in the error attributed to the actuator itself, and not other components in the dispenser.

Characterizing the New Focus® Picomotor as installed on the syringe dispenser under loading conditions is important for the accuracy of future experiments to be done with the dispenser. Accurate displacements of the linear motor directly correlate to accurate volumes dispensed by the dispenser. Since the actuator lacks any velocity feedback (supplied by an velocity encoder, for example), the actuator could behave variably under loading conditions when dispensing a commanded flow rate. The goal, therefore, is to quantify how the actuator's displacement and velocity behaves under loading.

Actuator characterization was carried out using micro-scanning vibrometer (MSV) equipment (OFV 5000, Polytech Inc.). The length of the dispenser assembly required elevating and clamping the microscope of the MSV on a breadboard platform (Newport Corporation) that is supported by four aluminum rails. The dispenser assembly with the actuator is mounted vertically beneath the platform. The microscope is aligned with one of the thru holes in the breadboard and focused onto the back end of the linear motor's stage.

The actuator is controlled with the software and controller included with the device, which allowed manual “run forward” or “run backward” commands and user input of step size (displacement) and input of cycles per seconds (velocity). First, the linear actuator is characterized without any load. Step sizes of 500 nm, 1 μm , 2 μm , and 10 μm are chosen which correspond to dispensed volumes of 83 pL, 166 pL, 332 pL, and 1.66 nL, respectively. An input velocity of 1000 cycle/sec is also chosen for all step sizes so that all dispensing occurs in one second or less. The steps are manually initiated by clicking the “run forward” button in the controller software with about two seconds or more delay between steps. The MSV equipment and software (displacement card) recorded displacements using a time scan with appropriate resolution.

The linear motor is then characterized under load using an identical procedure as described with the unloaded scenario, although now a filled syringe (with DI water) is loaded onto the dispenser assembly and its plunger is aligned with the linear motor. The dispenser used a two centimeter long capillary with inner diameter of 150 μm for the dispensing port. Before measurements are taken, the motor is run forward until visual confirmation is made that fluid is being dispensed.

The results for both the loaded and unloaded scenarios are plotted in Figure 6 with one standard deviation for error bars. The mean for each displacement matched the commanded displacements closely (percent relative error of <5% for each displacement) and was well within the noise induced measurement error (~150 nm). The New Focus® Picomotor showed excellent repeatability as evidenced by the smaller error bars (standard deviation of ~175nm on par with measurement noise) for the 500 nm, 1 μm, 2 μm, and 10 μm displacements. Therefore, with the use of a position encoder on the New Focus® Picomotor, this dispenser showed no difference between loading scenarios, with very accurate control of displacements.

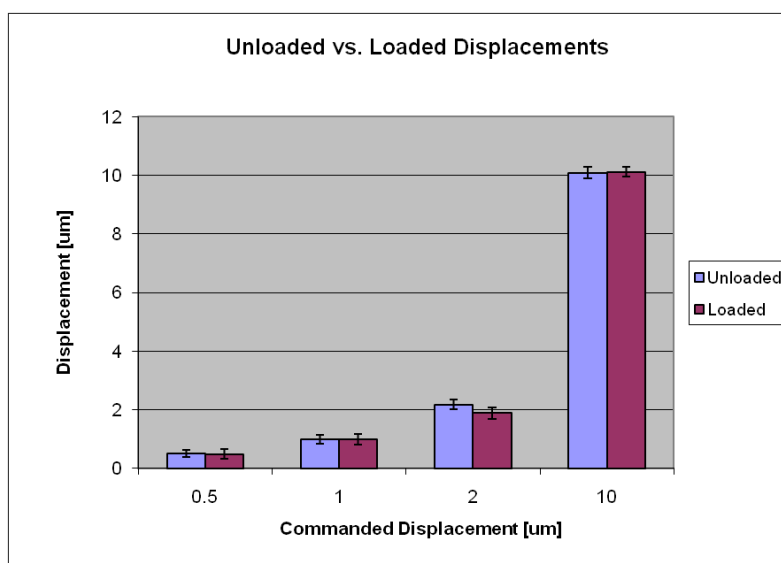


Figure 6 - Measured displacements versus commanded displacements for loaded and unloaded scenarios for the New Focus® actuator. The actuator showed high accuracy and repeatability for both scenarios (error bars plot one standard deviation).

In addition to the size of the steps being measured for displacements, the time taken to reach one step to another was measured to produce an average measured velocity that is calibrated to a speed setting of the actuator that is input into the program. This

speed setting is measured in cycles per second, where cycle refers to one step of the actuator. This single step is approximately 30 nm in net displacement of a sinusoidal velocity control signal, where the actuator is first driven in a direction of travel and then in a direction directly opposed to the direction of travel. (Figure 7) The actuator travels slightly further in the direction of travel than in a reverse direction, leading to the ~30nm in net displacement. Thereby, commanded steps larger than 30 nm consist of multiples of this single step and the speed is thereby controlled by inputting how many of these 30nm steps should be taken every second (cycles/second) to achieve the commanded displacement.

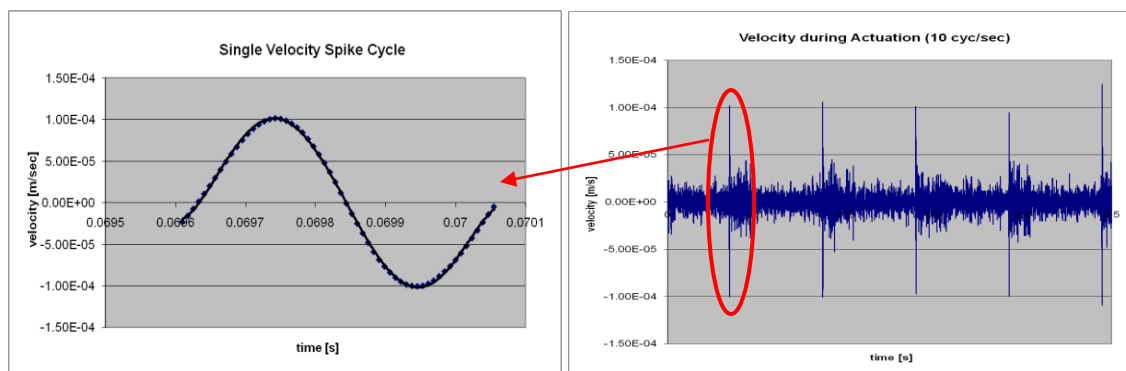


Figure 7 - (Left) One drive cycle of the velocity for the New Focus® actuator showing the initial reverse and then forward drive of the actuator. The net displacement of this cycle is ~30nm in the forward drive direction. (Right) Several drive cycles at a frequency of 10 cycles/second. This is the control parameter that is input into the control interface for the New Focus® actuator.

The measured average velocities' dependence on actuator input displacement and velocity without loading was investigated by two methods: 1) determining the velocity for varying velocities with a constant displacement; 2) determining the velocity for varying displacements with a constant velocity. Figure 8 shows the calibration curve between the input velocity (cycles/sec) and the measured output velocity ($\mu\text{m}/\text{sec}$) for

two sets done by the first method with two different series plotted for two different displacements. The two linear fit data are not statistically different according to an analysis of variance test ($P=0.05$) for the three data points with the same input velocity, and indicate no velocity dependence on input displacement. Figure 9 plots the measured velocity for a single input velocity (1000 cycles/sec) across varying input displacements. This plot shows no velocity dependence on input displacement as well, indicating that the velocity input is indeed a separately controlled parameter for the actuator as expected. The average of the plots yielded a calibration curve of $y=0.0332x$, where y is the output velocity [$\mu\text{m}/\text{sec}$] and x is the input velocity [cycles/sec]. The result of the calibration curve for unloading will be compared to the loading case when flow rates are measured for variable loading conditions, since measurement of flow rates directly provide a better estimation of variable loading effects.

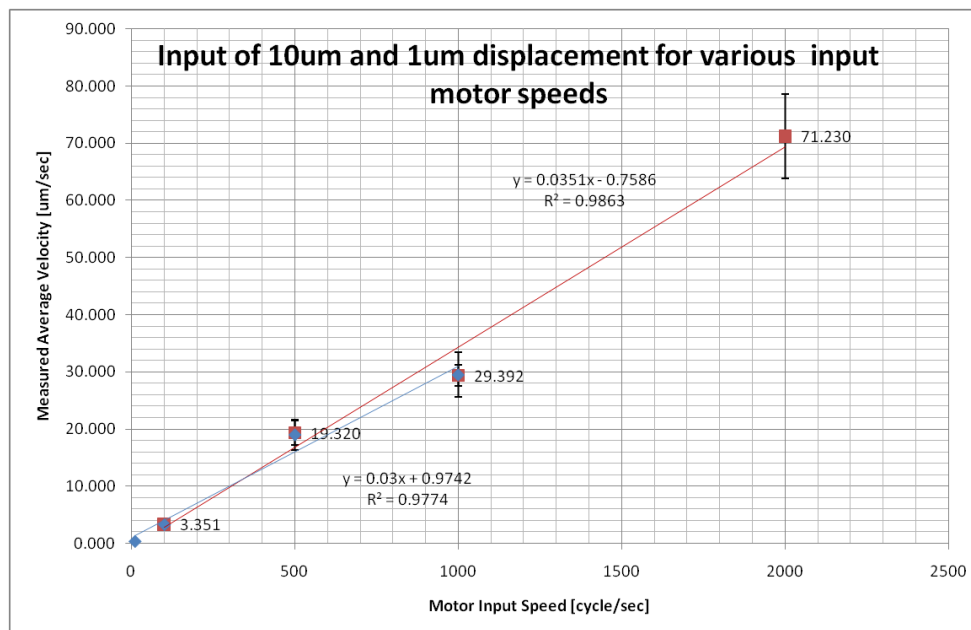


Figure 8 - A calibration plot of the New Focus® actuator's measured velocity for a given input of cycles/second in the control interface.

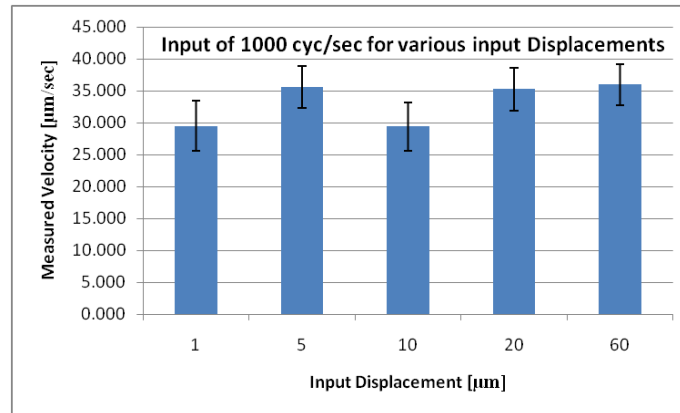


Figure 9 - A comparison of measured velocities for varied input displacements. The New Focus® actuator showed no velocity dependence with actuator displacement.

3.2.2 Volume Characterization for Input Displacement using Meniscus Tracking

Confirming that the actuator's displacements directly translate into expected dispensed volumes is critical in evaluating dispenser operation. Thus, an experiment is devised to measure these dispensed volumes for a given displacement input. The experimental method chosen was meniscus tracking adapted for use with the syringe pump dispenser. Meniscus tracking is very simple to use with the syringe pump since the delivery port capillary is accessible and can be viewed easily (16.875 X maximum magnification with 1 X objective) with a sampling rate as high as the microscope (SMZ 1500 Steroscopic, Nikon Inc.) camera's (10Mpx DS-Ri1, Nikon Inc.) frame rate.

The goal of the experiment is to determine the volume by tracking the meniscus inside the capillary, and correlate the displacement of this meniscus with the displacement input of the motor. (Figure 10) As discussed in section 2.3, the measured dispensed volume in the capillary should be equal to the volume displaced by the syringe plunger by conservation of mass (Figure 11).

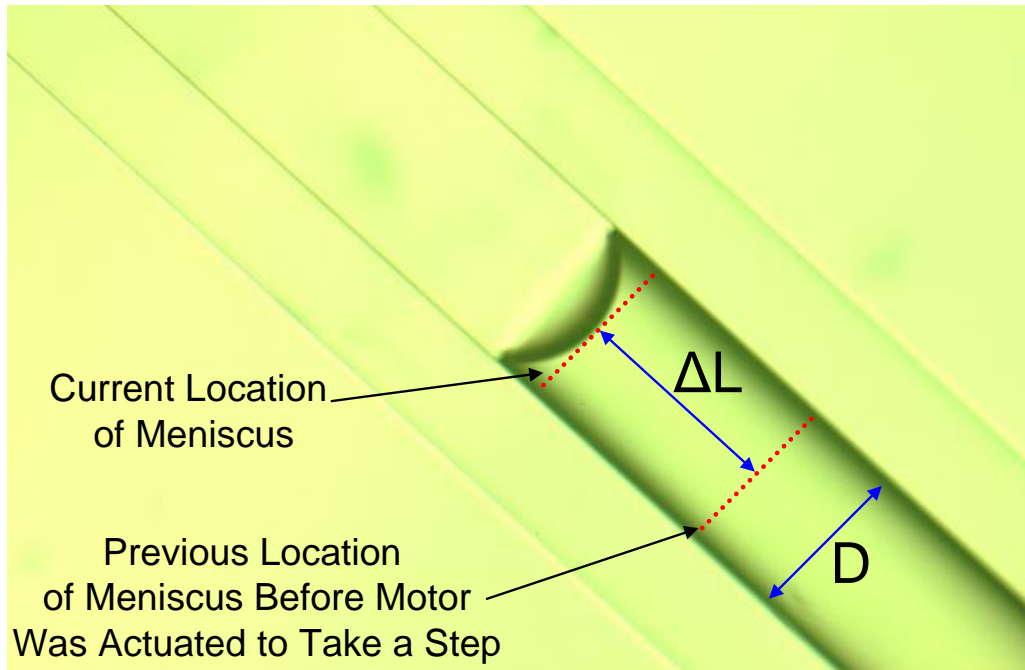
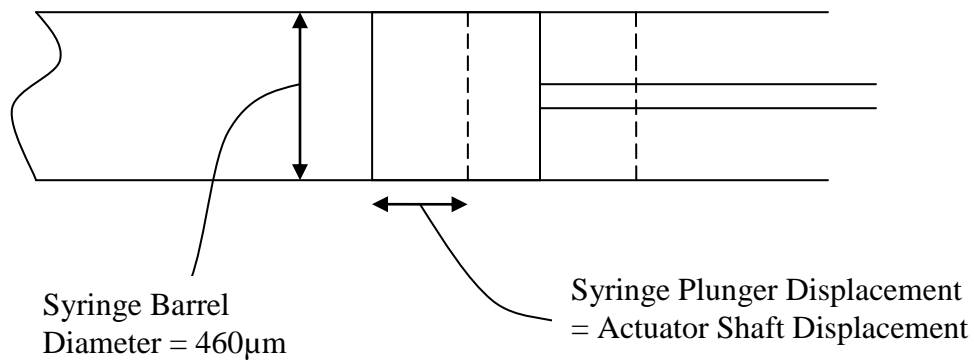


Figure 10 - Illustration of how the volume is measured in the meniscus tracking technique.



$$VolumeDispensed = \frac{\pi}{4} (460 \mu m)^2 \cdot displacement$$

Figure 11 - The relation between the actuator, plunger, and the volume dispensed.

Additionally, evaporation is eliminated if an immiscible liquid is used to form the meniscus or very limited if a liquid-air interface is examined far away from the capillary

tip. Also, there is no need to incorporate any sensors in or very near the flow path, such as with use of flow rate or capacitance sensors. The only real disadvantage is the use of a meniscus that inherently defines this method as a non-contact volume measurement. However, as will be seen in later sections, meniscus tracking can be supplemented with plunger tracking to utilize a contact method of volume and flow rate measurements.

Experimental Setup

The experimental setup consists of attaching a dispensing capillary of desired diameter to the dispenser assembly with the actuator and a filled syringe. The polyimide coating is burned off the tip of the capillary to allow for better transparency. The meniscus formed in the inner diameter of the capillary is then viewed under microscope after being inserted into a transparent silicone oil reservoir or the tip allowed to remain free in air, forming a liquid-air meniscus deep inside the capillary. The experimental setup is shown in Figure 12.

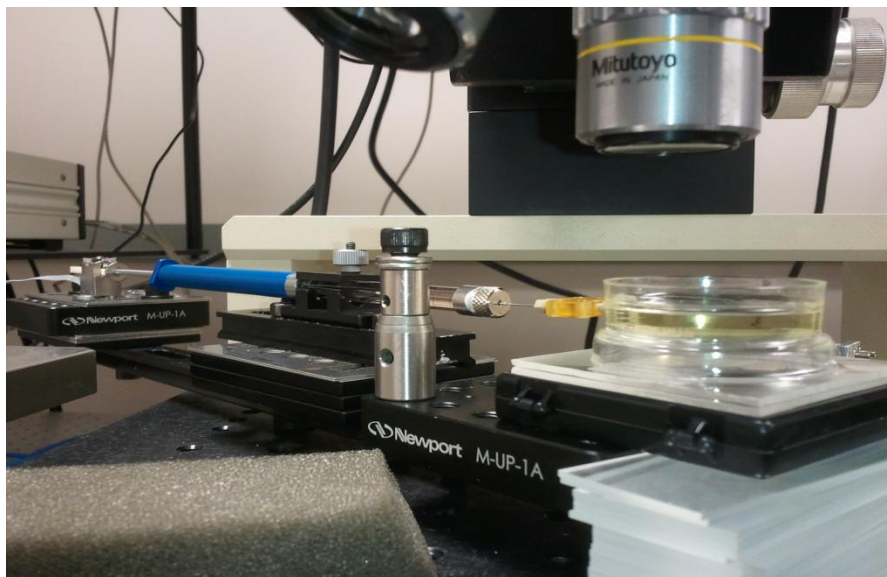


Figure 12 - Experimental setup of the meniscus tracking technique.

The measurements are done using the microscope camera and measurement software (NIS-Elements, Nikon, Inc.) that is calibrated with a reticle. The inner diameter of each different capillary used is measured and after each actuator step, the meniscus is allowed to settle, and the distance the meniscus is displaced is measured and recorded. Measurement of the inner diameter of the capillary is also carried out.

Several precautions and techniques are taken to ensure that accurate measurements are made. It is preferred that the dispensing capillary is inserted into a silicone oil media, which has the benefit of eliminating evaporation that would normally occur at an air-water meniscus near the end of the capillary. Elimination of air bubbles in the flow path is also critical, so syringe filling with de-ionized (DI) water is done with special attention to avoid capturing an air bubble near the plunger or in the needle. Also, before any dispensing and recording of measurements, the entire volume of the flow lines outside the syringe barrel is purged to clear any air that may have been captured making connections between the syringe needle and the capillary.

After all air has been expelled from the system, a small droplet of DI water is formed at the end of the capillary immersed in oil. This droplet is then pulled back into the syringe to form an oil-aqueous meniscus inside the capillary. In the case of the open ended capillary the droplet of DI water formed at the end of the capillary is allowed to evaporate and a water-air meniscus is formed inside the capillary. Measurements are begun only after the meniscus has stabilized and does not move a detectable distance, due to evaporation, for five minutes.

Results

The volumes were measured according to the method above using a silicone oil reservoir and thus, oil-aqueous meniscus tracking. A capillary with two centimeter length and 150 μm inner diameter was used as the delivery port. The results for the measured volumes for various displacements are shown in Figure 13. The theoretical volume is simply the calculated volume from the product of the cross sectional area of the syringe and the input commanded displacement. The measured volumes agreed extremely well with the theoretical volumes. The relative percent error from the mean measured volume was less than 6.4% for each displacement and approximately 3.6% for the calibration curve fit when compared to the theoretical. Repeatability was also very high with low standard deviations of less than 6.6% for all displacements except the 1.25 μm commanded displacement that was 12.1%.

A capillary with two centimeter length and 100 μm inner diameter was used as the delivery port. With use of a smaller inner diameter capillary, evaporation was significantly reduced, thus an air-aqueous meniscus tracking technique was utilized. The results for the measured volumes for various displacements are shown in Figure 14. The measured volumes agreed extremely well with the theoretical volumes. The relative percent error from the mean measured volume was less than 7.4% for each displacement and approximately 4.1% for the calibration curve fit when compared to the theoretical. Repeatability was also very high with low standard deviations of less than 13.3% for all displacements.

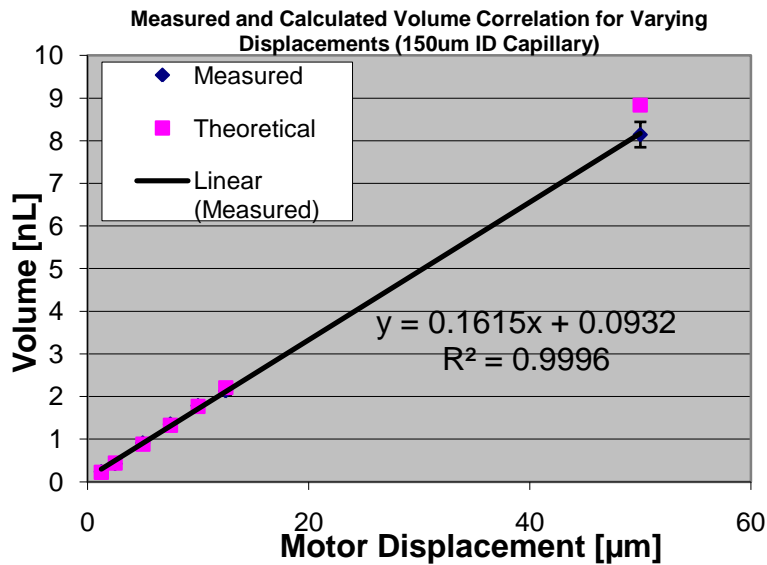


Figure 13 - The measured volume (diamond markers) versus the input actuator displacement. A linear fit (equation shown) showed high correlation with the expected calculated volume (square markers). This indicates almost no fluid leakage or actuator/plunger misalignment.

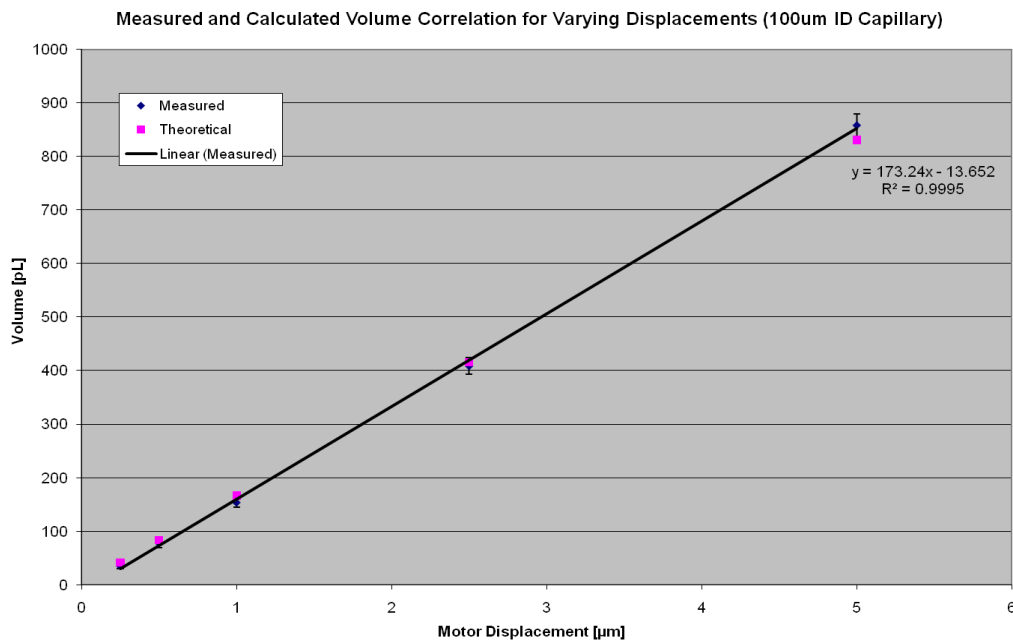


Figure 14 - The measured volume (diamond markers) versus the input actuator displacement. A linear fit (equation shown) showed high correlation with the expected calculated volume (square markers). A volume measurement as small as 42 pL was possible with this capillary and the New Focus® actuator.

A similar procedure was carried out using the same experimental setup for the syringe pump with a capillary of length two centimeters and inner diameter 50 μm replacing the 100 μm inner diameter capillary. As the commanded volumes are scaled down it becomes more difficult to measure a volume change as the cylindrical plug becomes more disc shaped with decreasing volume. Using a smaller diameter capillary allows easier and more precise measurement of the meniscus displacement and also allows for investigation of any scaling effects on the dispensed volume. The results for the measured volumes for these displacements are shown in Figure 15. The relative percent error from the mean measured volume was less than 26.8% for each displacement and approximately 14.1% for the calibration curve fit when compared to the theoretical. Repeatability was good with standard deviations of less than 18.8% for all displacements.

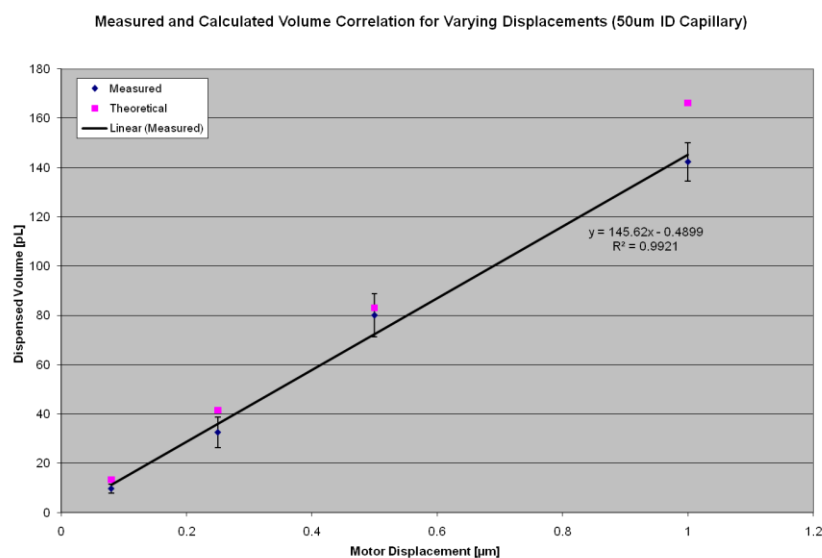


Figure 15 - The measured volume (diamond markers) versus the input actuator displacement. A linear fit (equation shown) showed high correlation with the expected calculated volume (square markers). A volume measurement as small as 9.8 pL was possible with this capillary and the New Focus® actuator.

The higher error and reduced repeatability for this experimental setup are thought to arise from two sources: 1) the smaller 50 μm diameter of the capillary causes increased buildup of pressure during dispensing and small leaks may occur in the system resulting in volume loss; and 2) the small displacements are very near the resolution of the encoder (80nm), which will result in a greater spread of displacements and higher standard deviations. The first source of error, pertaining to volume loss due to leaks, is evidenced by the fact that all four data points in Figure 15 show lower measured volume than the theoretical volumes and three out of the four data points are more than one standard deviation (error bars) below the theoretical points. Evidence of leaks was further provided when a capillary of the same length and inner diameter 10 μm was used (data not shown) with the same experimental procedure. Relative percent errors for the measured volumes were in excess of 75.2% for all commanded displacements and were always lower than the expected theoretical volumes.

Nevertheless, despite leakage in this system for capillaries with small inner diameters under 50 μm , the dispenser was shown to demonstrate dispensing of discrete volumes of 9.7 ± 1.8 pL (mean \pm S.D.) at the 80nm resolution of the New Focus® Picomotor's encoder.

3.2.3 Flow Rate Characterization for Input Velocity Using Meniscus Tracking

Another separate experiment is devised to calibrate the New Focus® Picomotor's input velocity with the measured flow rate with respect to each other. Meniscus tracking is again relied upon to obtain the calibration curves between the input and output parameters. Meniscus tracking to yield the measured flow rate offers the same advantages as it did for the measured volumes and can be utilized with the already established

experimental setup and data acquisition techniques. The only critical difference between the two measurement techniques will be the additional requirement to keep track of time taken for the meniscus to reach one position from another to obtain a measured flow rate.

The experimental setup is identical to the setup for determining measured dispensed volumes with the dispenser utilizing the New Focus® Picomotor and an open-ended capillary to allow tracking of an air-liquid meniscus. Time-lapse videos of the moving meniscus are recorded at a frame rate of approximately 10fps during multiple displacements steps of the actuator. The videos are then examined frame by frame to determine the start and stop times of the meniscus for a single step and the displacement that occurred in that time period. Thus, the velocity is measured as an average, $\Delta x/\Delta t$, and then converted into a flow rate by the product of the average velocity and the cross-sectional area of the capillary's inner diameter. The dependence of the measured flow rate on the inner diameter of the capillary is also investigated. Capillaries of inner diameter 150, 100, 75 and 50 μm are used with measured inner diameters of 152, 99, 75, and 52 μm , respectively. Flow rates are measured at four different velocity inputs for each of the four capillaries to establish a calibration curve with each capillary. The measured flow rates are compared to a theoretical value that is based upon the product of the syringe barrel cross-sectional area and the calibrated velocity obtained during the unloaded condition of the actuator (Figure 8).

The measured flow rates for each capillary and velocity input are plotted in Figure 16. For the 152, 99, and 75 μm capillaries, flow rate dependence on input velocity (calibration curve) was linear; however, for the 52 μm capillary the calibration curve was not linear. Also, for each point on all of the calibration curves, the measured flow rate

was always much less than that predicted for the unloaded velocity of the actuator. Low relative percent standard deviations of less than 20% were achieved for each data point for the 152, 99, and 75 μm calibration plots of the measured flow rates. However, for the 52 μm capillary plot, relative percent standard deviations were over 20% and some of the volumes were shorted, indicating some error introduced from leakage effects in the dispenser system. The volumes dispensed, however, were still very accurate for the 152, 99, and 75 μm capillaries, due in large part to the displacement encoder, indicating no leakage effects that could result in the decrease in flow rate. The dispenser was simply taking longer to dispense the same volume when a load was placed on the actuator, indicating compliance in the actuator or syringe plunger during dispensing. As can be seen in Figure 16, the slope of the calibration plot (0.0058, 0.0025, and 0.0019) can be seen to decrease with decreasing capillary inner diameter (152, 99, and 75 μm respectively). Since a decreasing inner diameter capillary effectively increases the flow resistance or, equivalently, the load on the actuator, one would therefore expect to see a reduced flow rate with a compliant actuator. Section 3.3 will further develop these relations with an appropriate hydrodynamic model of the dispenser and further analysis to explain these experimental phenomena.

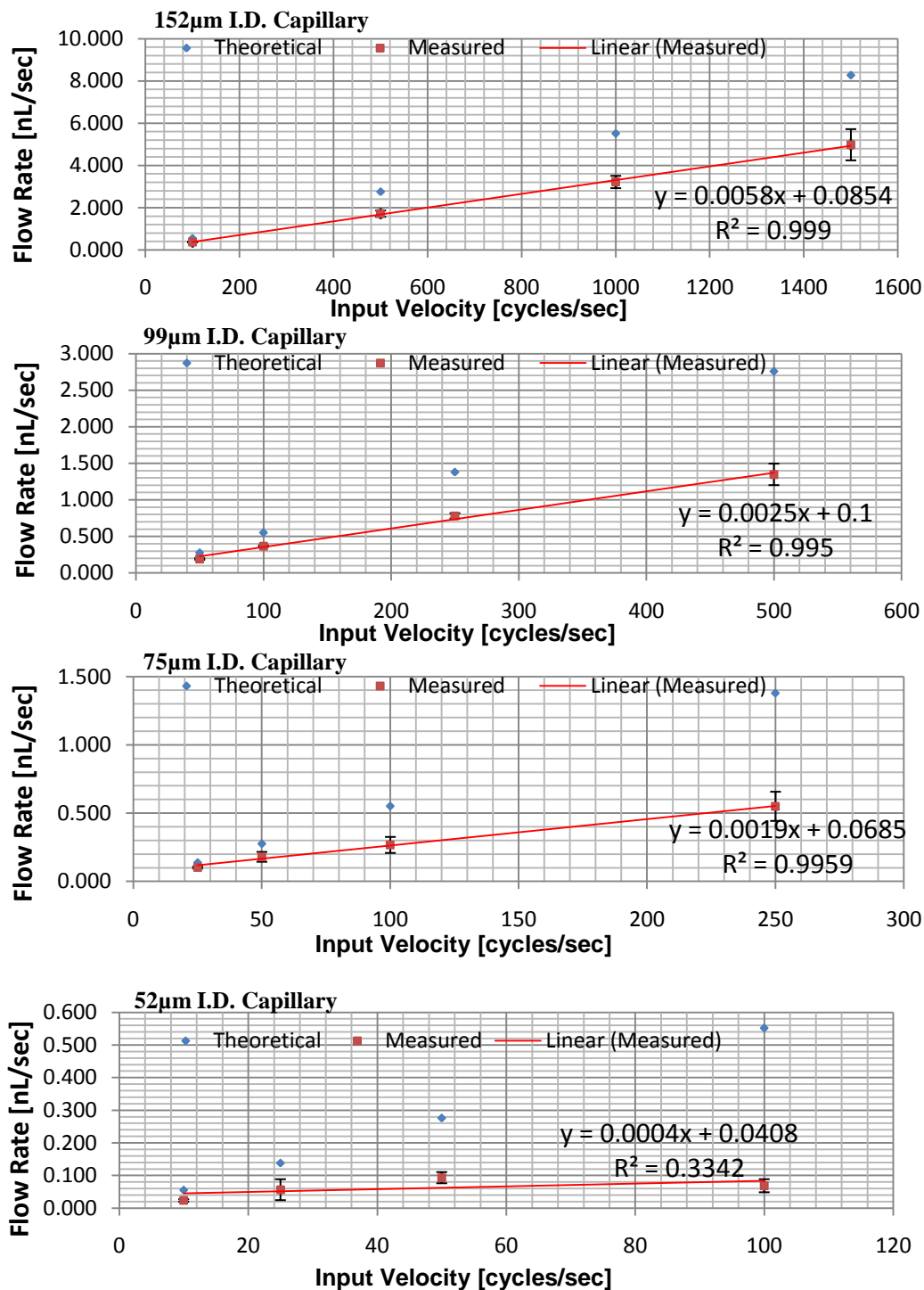


Figure 16 - A calibration plot of the measured flow rate (red markers) in a 152, 99, 75, and 52 µm inner diameter capillary for the input velocity control parameter of the New Focus® actuator. A linear fit (equation shown) of the measured flow rates was achieved for the 152, 99, 75 µm capillaries. However, the slope of the linear plots varied according to the inner diameter of the capillary and measured flow rates were much smaller than the expected theoretical values (blue markers) that were based off the calibration plot in Figure 15. The 52 µm capillary was not linear, possibly due to leakage in the dispensing system.

3.2.4 Flow Rate and Volume Characterization Using Plunger Tracking: Equivalence to Meniscus Tracking and Validation of Incompressibility

Similar to meniscus tracking, tracking of the plunger inside the syringe barrel can provide the same measurements of dispensed volume and flow rate (hydrodynamic parameters) if liquid incompressibility is a valid assumption. However, plunger tracking has the distinct advantage of being capable of contact-based measuring of dispensed volumes and flow rates. In other words, plunger tracking does not require a meniscus and therefore allows free dispensing of discrete volumes into any desired media while measuring the dispensed volume and flow rate. Essentially, the goal of this section is to validate the incompressibility assumption and to prove an equivalence of two experimental techniques, plunger tracking and meniscus tracking, that measure hydrodynamic parameters.

The experimental setup for plunger tracking is identical to the setup for meniscus tracking to measure dispensed volumes and flow rates with the only critical difference that the plunger's movement inside the syringe barrel is tracked instead of the meniscus. However, in an attempt to prove liquid incompressibility and equivalence of plunger and meniscus tracking, three experiments for measuring hydrodynamic parameters are conceived for comparison: 1) meniscus tracking of an air-liquid meniscus in the capillary; 2) plunger tracking with a meniscus in the dispensing capillary (non-contact measurement); and 3) plunger tracking while dispensing into an miscible reservoir (aqueous) with no meniscus in the capillary (contact measurement).

Flow rates and dispensed volumes are measured in the same way as before by recording and analyzing time-lapse videos of either the moving meniscus or plunger all

while using a 75 μm dispensing capillary of two centimeter length. Four different flow rates and four different volumes are compared for each of the three different methods.

Figure 17 shows the comparison of the three different measurement methods for dispensed volume plotted for four different input displacements. The figure shows no distinction between the three methods for any of the measured volumes. As a result of the highly correlated data, an equivalence between the three different volume measurement techniques is demonstrated.

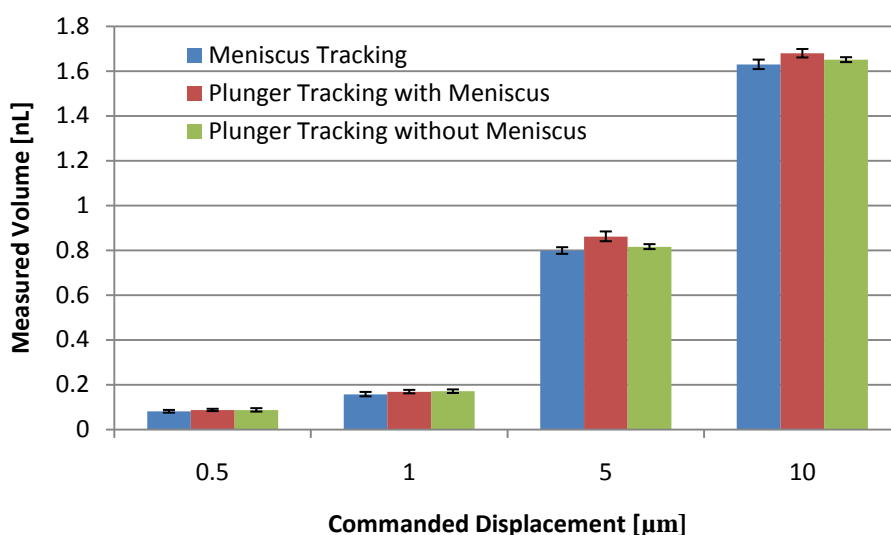


Figure 17 - Comparison between volume measurement techniques for different input volumes. All three methods produced similar results, thus showing the equivalence between the techniques for measuring volumes.

Figure 18 shows the comparison of the three different measurement methods for flow rates plotted for four different input velocities. The figure shows no distinction between the three methods for any of the measured flow rates. Therefore, not only is equivalence between the methods demonstrated, but also the assumption of liquid incompressibility is shown to be quite valid, since there is no discernible difference

between measuring the flow rate at the plunger or downstream near the meniscus. Also, the suitability of plunger tracking as a contact method (without using a meniscus) is also confirmed due to the correspondence between both plunger tracking methods for both hydrodynamic parameters.

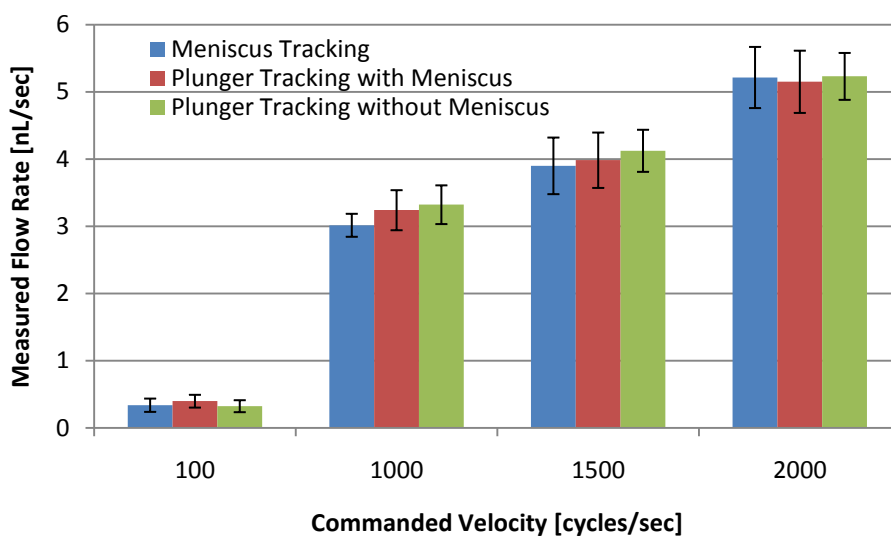


Figure 18 - Comparison between flow rate measurement techniques for different input velocities. All three methods produced similar results, thus showing the equivalence between the techniques for measuring flow rates.

3.2.5 Flow Rate Dependence on Insertion into Agarose Gel

The plunger tracking contact-based method can be used to investigate the dependency of the flow rate on the media of interest. Agarose hydrogel is one such media, due to its similarity to neuronal tissue in both its mechanical and transport properties [40]. Although real neuronal tissue, particularly the retina, has a hydraulic conductivity and diffusivity that are considerably anisotropic [41], isotropic agarose gel still provides a first order experimental model that is much more convenient to obtain and handle. Of primary interest, is how the interface between the dispensing capillary and the tissue, or in this case the gel, affects the delivered volumetric flow rate. To this end, an

experiment is devised to measure and compare flow rates for two different dispensing capillary positions in relation to the gel.

The experimental setup is very similar to the plunger tracking procedure for determining flow rates in section 3.2.4. The only difference in the experimental setup is a platform upon which agarose gel is placed. (Figure 19) The platform has a through hole in its center that allows the dispensing capillary to be inserted through. Agarose hydrogel of 0.6% agarose was prepared by adding 0.6 wt % agarose and 0.9 wt % sodium chloride to de-ionized water at 100°C and stirred for ten minutes with a magnetic stirrer at the same temperature. The gel is then transferred to a storage bottle, sealed and allowed to solidify at room temperature. When a sample volume is required, the storage bottle is heated to 90°C and the desired volume pipette from the storage bottle. For these experiments, a small volume was transferred by pipette to a small mold to create small discs 5mm in diameter with thickness 2mm.

For the experimental procedure, flow rates are measured for three separate loading scenarios: 1) a control scenario where no agarose gel is used and liquid is dispensed from a free capillary; 2) the dispensing capillary is abutted adjacent to the edge of the gel; and 3) the dispensing capillary is fully inserted into the gel. The capillary is positioned either flush with or 1mm above the platform surface and then a gel disc is placed on the platform resulting in either the gel abutting or gel insertion loading scenarios. Special attention is made to visualize dispensing at the end of the capillary with the aid of dyes before flow rate measurements are taken to ensure dispensing is occurring. Plunger tracking inside the syringe barrel is then utilized to determine the flow rate. For each loading scenario, flow rate dependence on input velocity is investigated by

using four different velocities (500, 1000, 1500, 2000 cycles/sec) with a constant displacement of 100 μm . Also, flow rate dependence on input displacement is investigated by using four different displacements (50, 100, 200, 300 μm) with a constant velocity of 1000 cycles/sec.

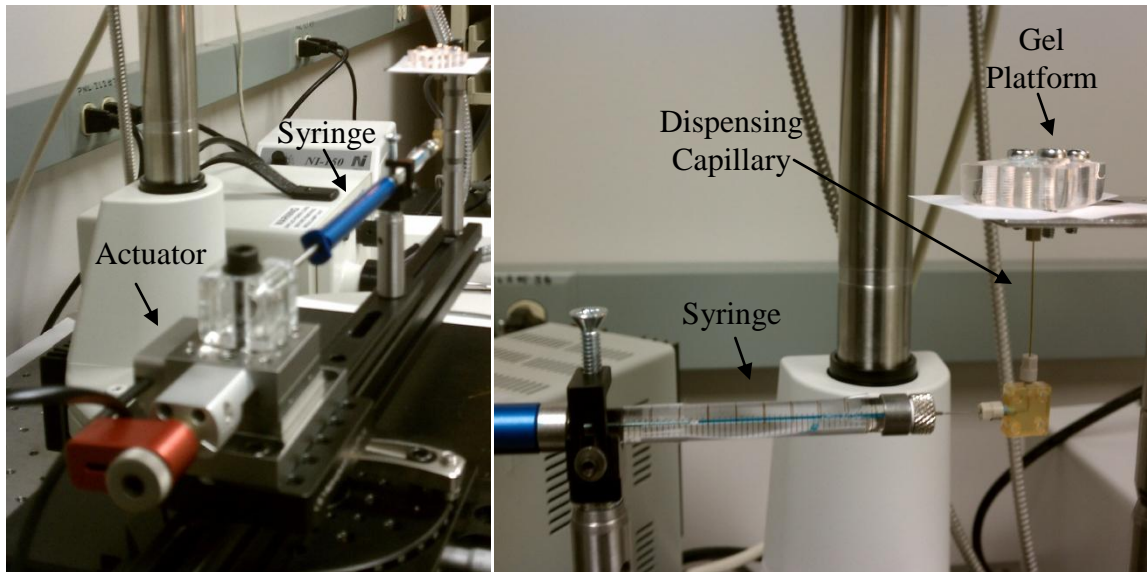


Figure 19 – (Left) Experimental setup for measuring the flow rates through plunger tracking while dispensing in the gel. (Right) A platform was used to hold the gel and allow a capillary to be placed adjacent the bottom of the gel or be inserted into the gel.

The results of the measured flow rate for each of the loading scenarios as the input velocity is varied is shown in Figure 20. All three loading scenarios produced similar calibration plot slopes and no statistical difference was found between the loading scenarios according to an analysis of variance test ($p < 0.05$).

Similarly, as Figure 21 suggests, there was no statistical difference between loading scenarios when the displacement was varied according to an analysis of variance test ($p < 0.05$). This result was somewhat unexpected since the gel was thought to provide significant resistance to flow due to its low hydraulic conductivity. Nevertheless, if the

gel simply deforms and displaces when a discrete volume is dispensed from the capillary, the resistance to flow will be significantly reduced, possibly resulting in an undetectable increase in flow resistance when compared to the control scenario of a freely dispensing capillary without gel.

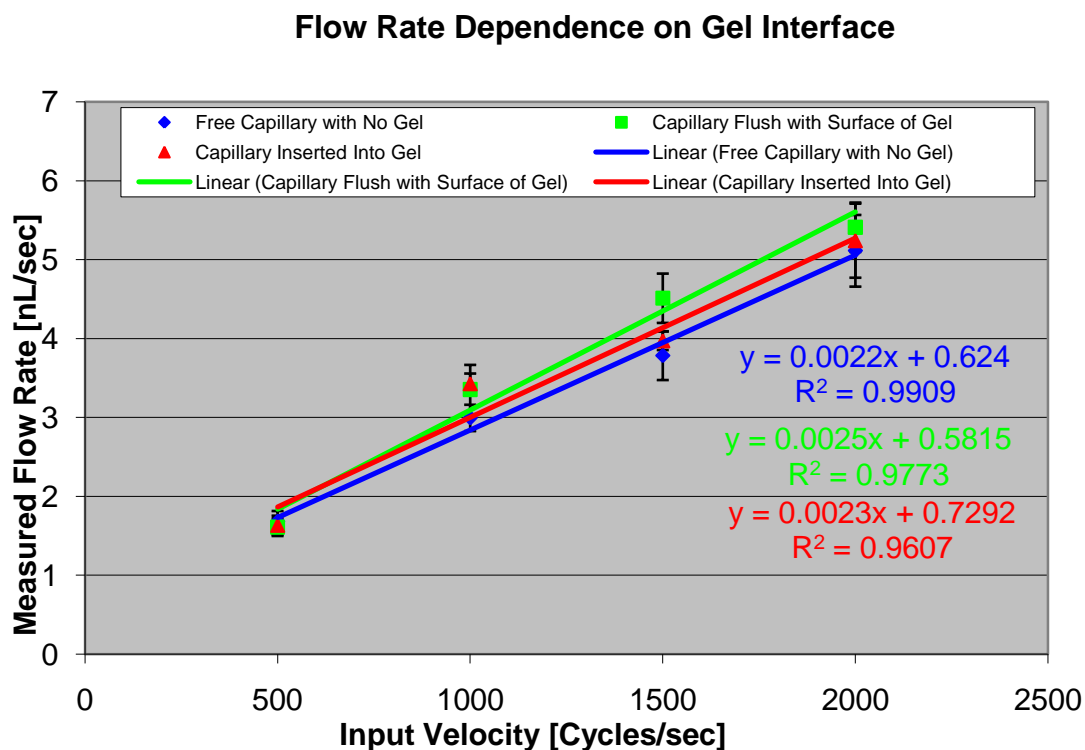


Figure 20 - Plot of the measured flow rate versus the input velocity for three different scenarios: a 75 μm capillary dispensing into air or the same capillary is placed adjacent or fully inserted into an agarose gel. All three scenarios produced similar results.

Supporting this hypothesis of gel deformation during dispensing is the trend seen in Figure 21 with the two gel scenarios as the commanded displacement (amount of volume injected) is increased. The flow rate decreases as the amount of volume injected is increased, indicating that the gel is being deformed and compressed away from the dispensing capillary tip that results in increasing back-pressures as injected volume is increased. This gel deformation phenomena will be explored more in Chapter 4.

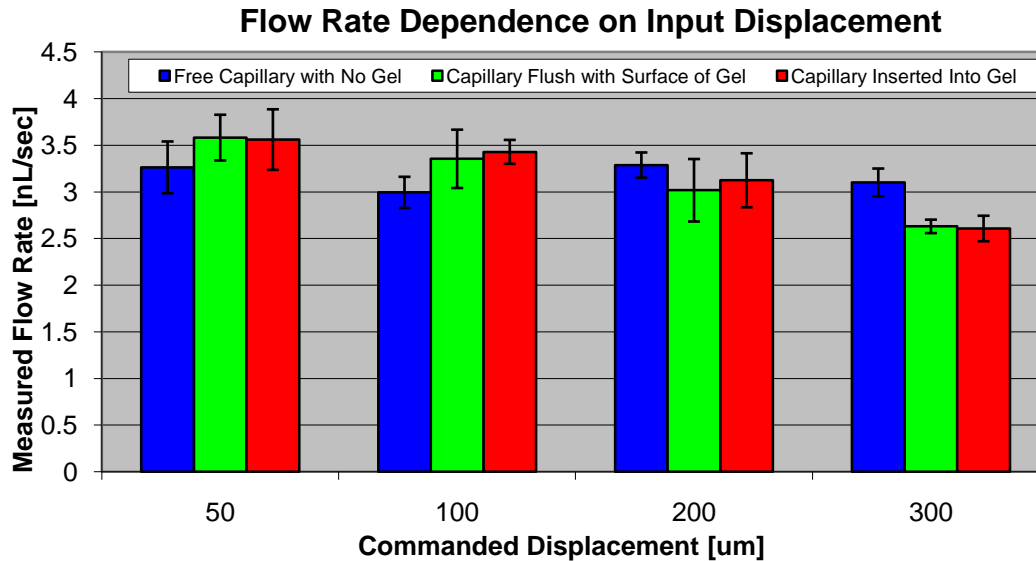


Figure 21 - Plot of the measured flow rate versus the input displacement for three different scenarios: a 75 μm capillary dispensing into air or the same capillary is placed adjacent or fully inserted into an agarose gel. All three scenarios produced similar results for a given displacement, but larger volume injections seemed to effect the flow rate for the gel scenarios.

3.2.6 Summary of Results from Experimental Measurements of Hydrodynamic Parameters

Testing revealed that the volume dispensed was reasonably accurate (only 4.1% relative error with a 100 μm inner diameter capillary in the 100 pL – 10 nL range) with respect to the predicted volume based on actuator displacement. This close match between theoretical and measured volumes at this small scale reveals that accurate alignment of the actuator and syringe, as well as a leak-proof delivery system, was achieved for capillaries of large inner diameter ($>50 \mu\text{m}$). For capillaries of inner diameter 50 μm or less, the increased flow resistance from the capillary resulted in higher pressures in the dispenser causing leakage that produced much smaller than expected volumes. The source of the leak was identified to be the removable needle hub that

secures the needle to the syringe barrel. Also, measured flow rates had a linear dependence on input velocity, yet they had a non-linear dependence on capillary inner diameter.

Characterization also revealed that while the measured flow rates deviated from the predicted values, the flow rates dependence upon input velocity was linear and thus predictable. The deviation of the measured flow rate from predicted values was determined to be mostly due to compliance in the actuator and syringe plunger rod components. This mechanical compliance could be reduced by using a shorter syringe plunger rod to reduce the amount of axial compression during actuation. When using dispensing capillaries of inner diameter 20 μm or less, the amount of hydraulic resistance becomes large enough to cause compliance in the fluid dispensing lines. This compliance may be reduced if the capacitance of the syringe barrel is reduced. The capacitance, in turn, may be reduced by reducing the volume of the syringe barrel. This can be done by either using very small reserve fluid in the syringe already in use or by using a syringe barrel with a much smaller inner diameter, with the latter of two options being more effective at reducing the hydraulic compliance.

Meniscus and syringe plunger tracking proved to be very effective experimental techniques that are capable of measuring very small dispensed volumes in the picoliter to nanoliter range and flow rates over a wide range. The limit for measuring volumes or more directly, the length of the meniscus or plunger displacement, depends on the inner diameter of the dispensing capillary or syringe barrel and the total magnification of the optics in the microscope. In addition to these factors, the measured flow rate also depended upon the frames per second (fps) at which the videos were recorded at during

dispensing, since this determined the accuracy of evaluating start and stop times of the meniscus or plunger movement. However, there is a general trade-off between the quality of videos (number of pixels in a frame) and the rate of fps captured for any camera.

Finally, interface or surface tension effects did not significantly affect measured flow rate values as evidenced by the same values obtained whether or not a meniscus was present (see section 3.2.4). Also, gel resistance seemed to be negligible (see section 3.2.5) or at least it did not have as much of an effect as changing capillary inner diameters.

3.3 Theoretical Modeling of Fluid Conduits in the Dispenser

The experimental work thus far indicates that there is compliance (see section 3.2.3) in the syringe pump dispenser that is affecting the output flow rate. Thus, a model of the conduit lines can reveal insight into whether or not the compliance is a result of compressible fluid or dilatable conduit walls. Also, since the compliance seems to be a function of the resistance to flow when different sized capillaries are used, a formal definition of the hydraulic resistance of a capillary is required. The following theory of hydraulic circuit analysis provides a theoretical framework to address these requirements [42].

Hydraulic circuit theory accounts for compliance from both the fluid compressibility and conduit dilatability by modeling each conduit as a combined resistive and (volume) capacitive element. The fluid conduits are then reduced to a circuit that may be further reduced to a set of linear time dependent ordinary differential equations that can be solved numerically. This numerical approach turns out to be much simpler

and faster than using finite element or difference techniques, since this 1D technique minimizes the number of elements to solve for.

Essentially, the goal of the analysis of this model is to determine the output flow rate, for a given input flow rate (input plunger velocity). Without appreciable compliance in the fluid path, the input and output flow rates will be equal. Thus, the assumption of liquid incompressibility and non-dilatibility of conduit walls will be validated if this result is obtained. For complete understanding of this technique, a brief introduction to hydraulic circuit analysis is first presented.

3.3.1 Introduction to Hydraulic Circuit Analysis

As mentioned in section 3.1, although laminar flow is a valid assumption for micro-scale capillaries, Hagen-Poiseuille flow, which describes laminar flow in capillaries, can only be used for steady state conditions where inertial forces and viscous forces balance out (fully developed flow) [39]. Therefore, for discrete volume dispensing or pulsed flow, dynamics between the driving pulse source and the physical properties and arrangements of the conduits in the circuit must be accounted for. Hydraulic circuit theory accounts for these dynamics as well as compliance effects in the dispensing system due to compressible fluids and compliant conduits.

Hydraulic circuit theory [42] is essentially the hydrodynamic analog of electric circuit theory. Fluid volume, in replace of electronic charge, is what flows in a hydraulic circuit and is driven to flow by a hydraulic potential, i.e. a pressure difference. The analogy is summarized in Appendix A.1.

A conduit of any given size or shape can be appropriately modeled as a resistor with its hydraulic resistance, R_H , equivalent to:

—

where μ is the dynamic viscosity of the fluid in the conduit, L is the length of the conduit, A is the cross sectional area of the conduit, and r_H is the hydraulic radius of the channel, which is $r_H = 2A/P_W$, where P_W is the perimeter of the cross section. For a conduit of circular cross section, such as with a glass capillary, the hydraulic radius is simply the radius, r , of the conduit, thus the hydraulic resistance can be simplified:

—

Compliance in the hydraulic circuit may also be modeled for each conduit as a capacitor and has two sources of capacitance: 1) capacitance contributed from the compression of fluid volume under pressure in the conduit; and 2) capacitance contributed from the dilation of the conduit walls under pressure. The capacitance due to fluid compressibility can be modeled as:

— ——— —

where β is the compressibility or inverse of the bulk modulus, K , of the fluid. The capacitance due to conduit wall dilation can be modeled as:

— ——— —

where D is the dilatibility or inverse of the Young's modulus, E , of the enclosing conduit wall material. Finally, the flow rate, Q_C through a hydraulic capacitor may be determined from the hydrodynamic analogy of the current through a capacitor:

— — — — —

In summary, a single conduit can therefore be represented by a resistor in parallel with two capacitors in parallel, which can be simplified to a single capacitor in parallel with a resistor (Figure 22).

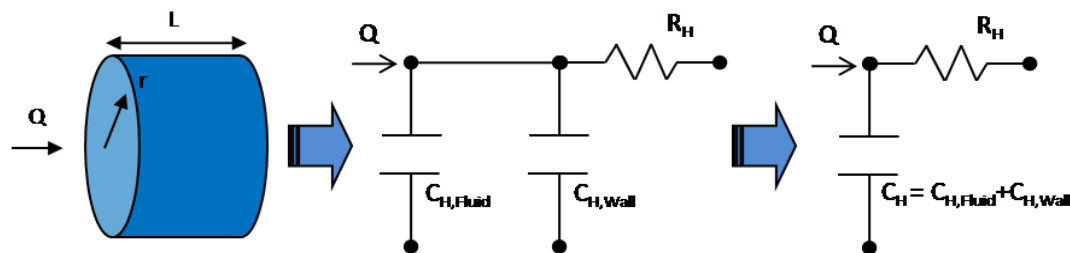


Figure 22 - A schematic on how a fluid conduit can be modeled as an electric circuit.

3.3.2 Full Model of the Syringe Pump Dispenser and Validation of the Liquid Incompressibility Assumption

Having described the analytical framework that is necessary to perform circuit analysis on a hydraulic system, this framework is now applied to model the syringe pump dispenser and investigate its dynamic response to various inputs. There are four separate conduits in the syringe pump dispenser that make up the fluid flow path. These consist of the syringe barrel, syringe needle, connector, and the dispensing capillary (Figure 23). Each of these conduits may be modeled as having a resistive and capacitive component,

and the conduits are placed in series to define the fluid flow path as a hydraulic circuit, as is shown in Figure 24. Thus, four nodes are defined with the flow rate from the plunger (the system input) inputted into the first node.

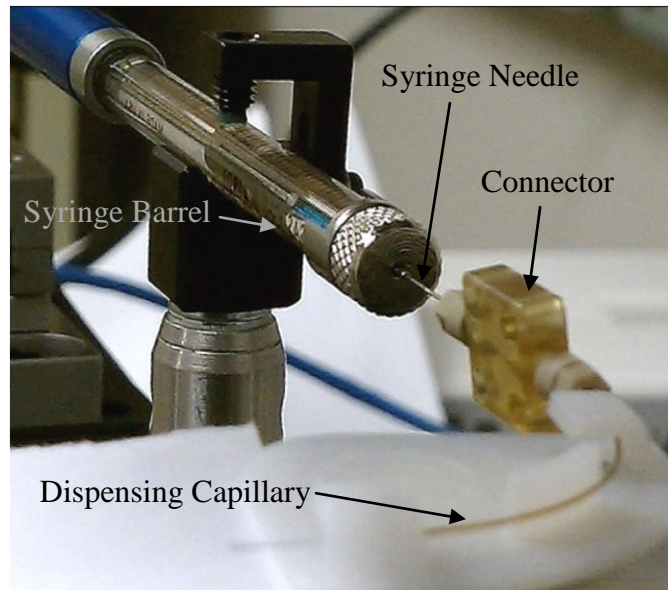


Figure 23 - Image of the fluid path in the syringe pump dispenser

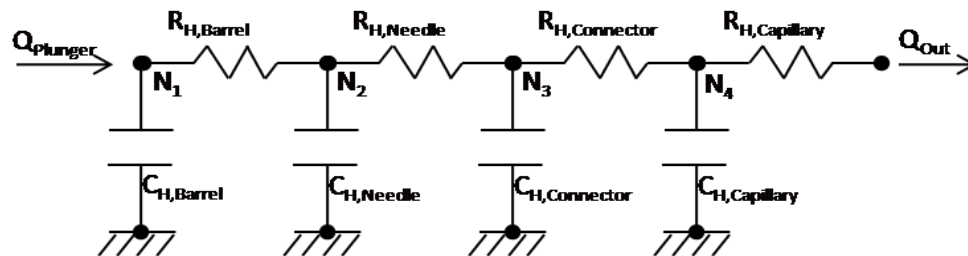


Figure 24 - Equivalent circuit of the syringe pump dispenser

Since the goal is to determine the output flow rate given an input flow rate, a set of equations describing the system must be solved for. This can be done by first applying Kirchoff's current (flow rate) law to each of the four nodes to obtain a set of four coupled equations:

At N_1 :

At N_2 :

At N_3 :

At N_4 :

Substituting in the definitions for flow rates across resistors and capacitors:

$$\begin{aligned}
 & \frac{dP_1}{dt} = \frac{1}{C_1} (Q_{in} - Q_{R1} - Q_{C2}) \\
 & \frac{dP_2}{dt} = \frac{1}{C_2} (Q_{C2} - Q_{R2} - Q_{C3}) \\
 & \frac{dP_3}{dt} = \frac{1}{C_3} (Q_{C3} - Q_{R3}) \\
 & \frac{dP_4}{dt} = \frac{1}{C_4} (Q_{R3} - Q_{R4})
 \end{aligned}$$

where $P_1, P_2, P_3,$ and $P_4,$ are the pressures at nodes $N_1, N_2, N_3,$ and $N_4,$ respectively. Thus, with a known input ($Q_{Plunger}$), there are four equations and four unknowns ($P_1, P_2, P_3,$ and P_4). Solving for the time derivative of each pressure ($\frac{dP_1}{dt}, \frac{dP_2}{dt}, \frac{dP_3}{dt},$ and $\frac{dP_4}{dt}$) yields:

$$\begin{aligned}
 & \frac{dP_1}{dt} = \frac{1}{C_1} (Q_{in} - \frac{P_1 - P_2}{R_1} - \frac{P_1 - P_2}{R_2}) \\
 & \frac{dP_2}{dt} = \frac{1}{C_2} (\frac{P_1 - P_2}{R_2} - \frac{P_2 - P_3}{R_3} - \frac{P_2 - P_3}{R_4}) \\
 & \frac{dP_3}{dt} = \frac{1}{C_3} (\frac{P_2 - P_3}{R_4} - \frac{P_3 - P_4}{R_5}) \\
 & \frac{dP_4}{dt} = \frac{1}{C_4} (\frac{P_3 - P_4}{R_5} - \frac{P_4 - P_5}{R_6})
 \end{aligned}$$

This set of linear first order ordinary differential equations can be easily solved with an appropriate numerical solver. To this end, a program (see Appendix A.2) was written in MATLAB® defining this set of equations and the pressure at each node as a function of time was solved with the ode15s solver for various input velocities and various lengths and inner diameters of the interchangeable end capillary. The output flow rate for all time can then be found by the simple relation $Q_{\text{Out}} = P_4/R_{\text{H,Capillary}}$. The input flow rate into the system is a step input function whose integration thereof is equal to a discrete volume pulse of 1.66 nL (typical value for a dispensed volume used in a following study, see section 4.2). To ease the numerical simulation and to more realistically capture how the actuator behaves, the input flow rate step function was approximated as a logistic step function of the form:

$$Q_{\text{In}} = a \left[\frac{1}{1 + \exp\left(-\frac{t - t_{\text{ON}}}{b}\right)} - \frac{1}{1 + \exp\left(-\frac{t - t_{\text{OFF}}}{b}\right)} \right]$$

where a is the peak (plateau) of the step function, b controls the rise and fall times, and t_{ON} and t_{OFF} are the on and off times of the step function.

Of particular interest is how small of an inner diameter of the capillary can be used when the actuator is driven at its fastest speed (2000 cycles/second or $\sim 71 \mu\text{m}/\text{sec}$, see Figure 8) without having any significant compliance in the fluid system. To reduce the amount of compliance in the system, the lowest resistance is desired. Hence, for a capillary of given inner diameter, the shortest possible length will result in the smallest resistance. The smallest capillary length that is feasible for use with the fittings is one centimeter (the length of the fitting itself). Therefore, Figure 25 shows a plot of how the inner diameter affects the output flow rates for an input speed of $71 \mu\text{m}/\text{sec}$ with a

capillary of length 1.0cm and a barrel length of 2.0 cm. Above an inner diameter of 20 μm for the dispensing capillary, the output flow rate shows very little deviation from the input flow rate, indicating very little compliance in the system and validating the liquid incompressibility assumption for capillaries above these values. Below an inner diameter of 20 μm , the compliance can be seen to have a very strong dependence on the inner diameter.

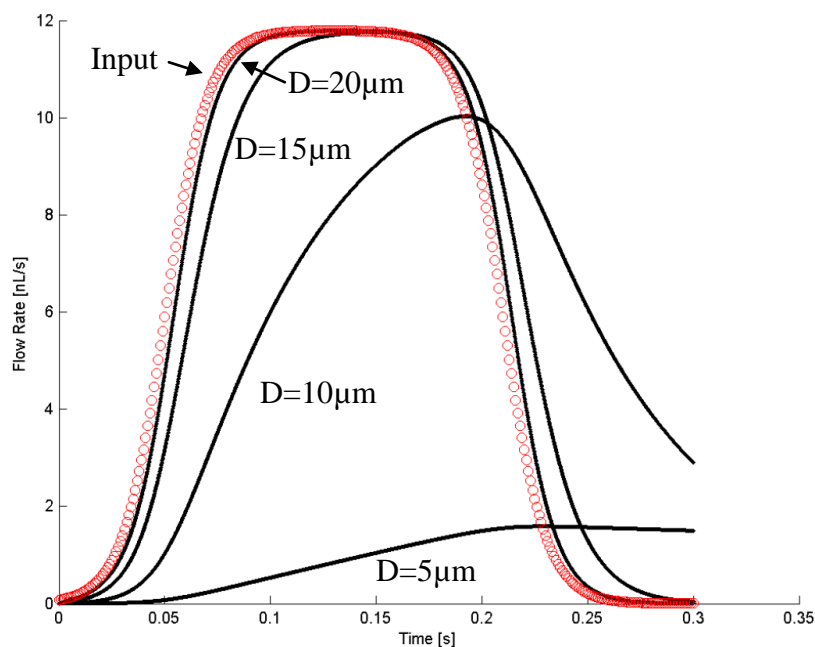


Figure 25 - A plot of the output flow rate (solid lines) for dispensing capillaries of different inner diameter all with the same input flow rate (circles). The flow rate varies sharply with decreasing inner diameter of the dispensing capillary.

Figure 26 shows the output flow rate dependence on the length of the capillary for the same input velocity and barrel length and a capillary inner diameter of 20 μm . The effect of capillary length is much less significant than the capillary's inner diameter. The length of the capillary needs to be on the scale of a meter or more for compliance effects to be noticed for the output flow rate. This result is not too surprising given that the

hydraulic resistance has a linear dependence on length, but has an inverse dependence on the radius of the capillary to the fourth power.

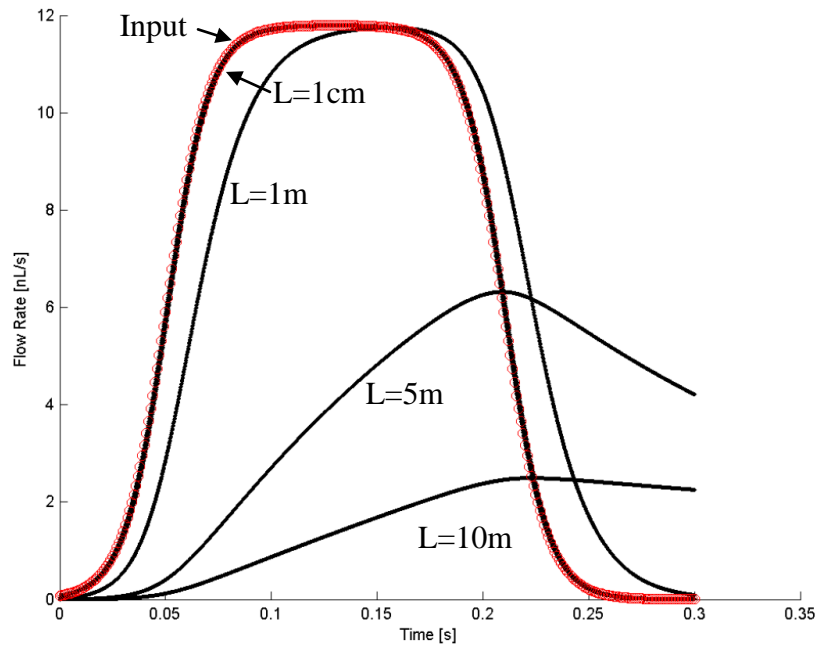


Figure 26 - A plot of the output flow rate (solid lines) for dispensing capillaries of different length all with the same input flow rate (circles). The flow rate varies only with a large increase in the length of the dispensing capillary.

The final parameter that can be varied is the plunger position in the syringe barrel or in other words, the length of the barrel as a conduit. The length of the barrel has a range of only 0-6 cm. Again, the same input velocity $71 \mu\text{m}/\text{sec}$ and a capillary inner diameter of $20 \mu\text{m}$ are used in this demonstration. As can be seen in Figure 27, the output flow rate has little dependence on the length of the syringe barrel if the plunger is moved to its maximum barrel length of 6 cm.

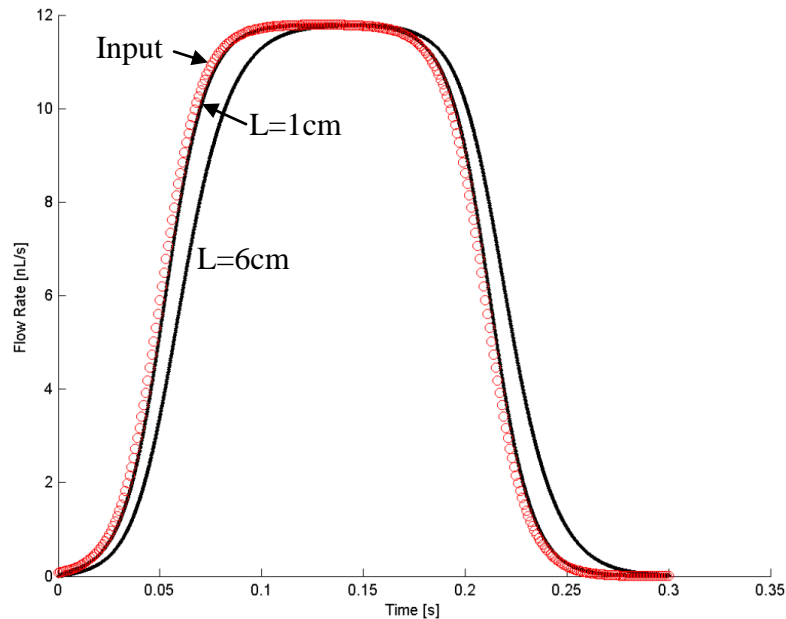


Figure 27 - A plot of the output flow rate (solid lines) for the syringe plunger at different positions (length of barrel conduit) all with the same input flow rate (circles). The flow rate varies very little over the range of the length of the barrel conduit.

3.3.3 Simplification of the Model

Looking at the capacitances of the four conduits, one readily finds that capacitance of the barrel is at least an order of magnitude larger than the rest of the capacitances ($C_{H,Barrel} \gg C_{H,Needle}, C_{H,Connector}, C_{H,Capillary}$). Similarly, the resistance of the capillary is at least an order of magnitude larger than the rest of the resistances ($R_{H,Capillary} \gg R_{H,Needle}, R_{H,Connector}, R_{H,Barrel}$). These relations are due to the much larger volume contained in the syringe barrel and the much smaller radius of the capillary. Therefore, the syringe pump dispenser system can be reduced to a simple circuit comprising a single capacitor ($C_{H,Barrel}$) and a single resistor ($R_{H,Capillary}$) in parallel (Figure 28).

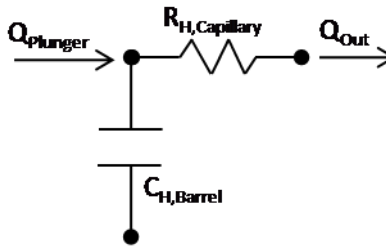


Figure 28 - Simplification of the complete dispenser circuit in Figure 26 to the circuit elements that have the largest effect on the system.

As before, Kirchoff's current law can be applied at the input node to obtain a single differential equation. This is solved again with the same numerical solver (see Appendix A.2), and the output flow rates are plotted in Figure 29 for capillaries of different inner diameter for the same input velocity, barrel length, and capillary length, as was plotted for Figure 25. A comparison between Figures 25 and 29 reveals that this simplified model is a good approximation for the full model described in the previous section.

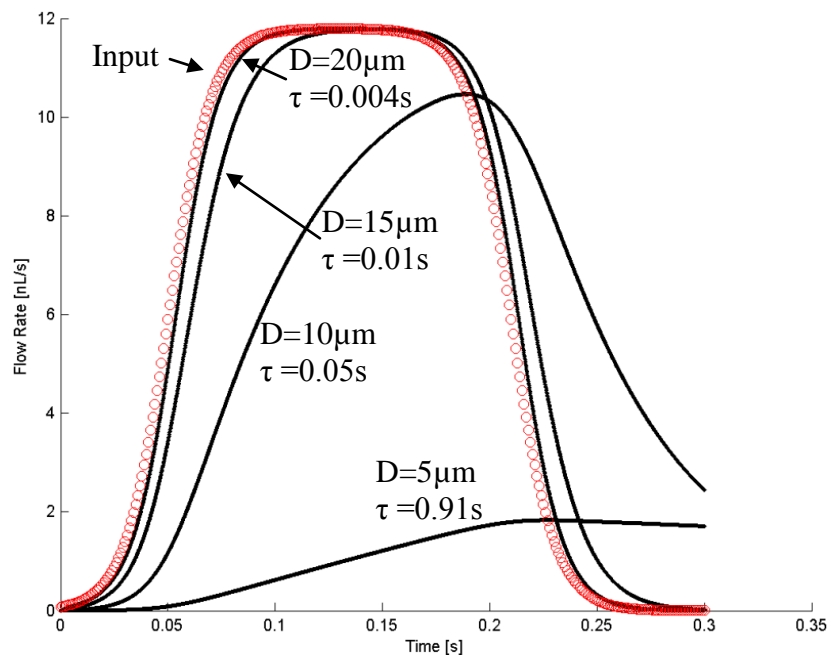


Figure 29 - A plot, using the simplified model of Figure 28, of the output flow rate (solid lines) for dispensing capillaries of different inner diameter all with the same input flow rate (circles). The flow rates obtained for this simplified model were nearly identical to the flow rates from the complete model.

This simple RC circuit has the benefit of predicting how the output flow rate will be affected by way of a simple parameter, the time constant, τ . It is well known from electrical circuit analysis that a parallel RC circuit's response to a constant current step function is simply an exponential rise dependent on the time constant [43], or in the hydraulic analogy:

Therefore, one can expect the output flow rate to lag behind and have a smaller peak flow rate than the input flow rate when the time constant is on the same order as the dispensing time for the discrete volume. However, one can safely assume there is no compliance in the dispenser, at least from the fluid system, if the time constant is much smaller than the dispensing time.

3.3.4 Formulating a Predictive Model of Flow Rates for the Syringe Pump Dispenser with Interchangeable Dispensing Capillaries

Turning attention back to the experiments conducted in section 3.2.3 for determining flow rates, the time constants determined for the 152, 99, and 75 μm inner diameter capillaries are 7.68×10^{-6} , 3.45×10^{-5} , 7.47×10^{-5} seconds, respectively, which were based on capillary length, inner diameter, and plunger position. With such small time constants, there is very little contribution to compliance from compressible fluids or dilatable conduits. This is supported from the experiments done in section 3.2.4 that confirmed there is no difference between measured flow rates from the plunger and meniscus tracking techniques, indicating no compliance in the fluid path for relatively large inner diameter ($>50 \mu\text{m}$) capillaries.

Yet, there is a significant difference between the calibrated input velocity of the actuator and the speed of the plunger that shows up as a reduced flow rate at the output. Therefore, the compliance must come from a compression of the mechanical linkage between the actuator and the plunger and/or from compliance in the actuator itself. This mechanical compliance also depends on the resistance of the capillary. Thus, it is proposed that the velocity of the plunger is not just a function of the cycle/second input of the actuator, but also a function of the hydraulic resistance of the conduit:

The flow rate can therefore be found through fitting the experimental data to an appropriate formula. Figure 30 shows a plot of the slopes of Figure 18 versus the hydraulic resistance of each capillary. A power function proved to be the best fit for this curve and thus, the flow rate may be determined from:

where $R_{H, \text{Capillary}}$ is in m^3/Pa , V_{Input} is in cycles/sec, and Q_{Out} is in nL/sec.

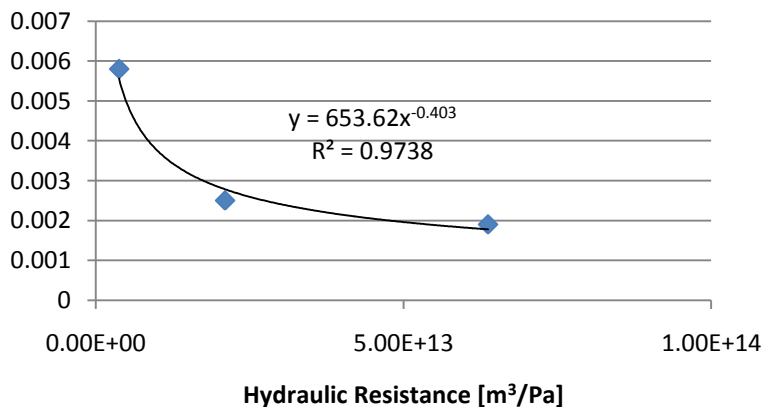


Figure 30 - A plot of the slopes obtained in Figure 18 for flow rate dependence on the hydraulic resistance of the capillary. The curve fit a power function.

CHAPTER 4 - DETERMINATION OF CONCENTRATION PROFILES THROUGH EXPERIMENTAL & THEORETICAL METHODS

This chapter discusses experimental and analytical techniques for imaging and determining ejection profiles from the dispenser and how the images may be converted into concentration profiles. There is great significance in knowing the concentration profile of an injected species in the target media (e.g. neuronal tissue), since it reveals the spatial extent of the target media that will be effected by the species. Additionally, knowledge of the profile could indicate whether or not the tissue is displaced during the dispensing event, which can limit the role convection plays during dispensing.

Existing experimental methods are briefly discussed to provide a background. A noninvasive imaging technique is chosen to examine what the delivery of the chemical species looks like as it is injected from the dispensing capillary to a tissue model, such as agarose gel. A brief review of the methodology is presented for complete understanding along with the modifications to this approach for it to be usable with the present application. The goal is to determine how injected species will diffuse and convect, the two modes by which molecules move in a fluid solution, from the dispenser into the target media for different hydrodynamic parameters. This amounts to knowing the concentration profile of the species in the target media as a function of time before, during, and after a discrete injected volume of known concentration from the dispenser. Methods are developed to convert the recorded images into a time developing concentration profile.

A theoretical finite element model (FEM) of the concentration profile developed from an ejection is then compared to the experimentally obtained values. Experiment-model correlation is discussed along with explanations for discrepancies.

4.1 Existing Methods to Measure Concentration Profiles

Experimentally obtaining a concentration profile of an injected discrete liquid volume with a particular concentration of therapeutic species into a complex aqueous-based medium such as a hydrogel or organic tissue, would be very desirable. Such knowledge of the species concentration profile in the delivery medium would allow for tailoring of dispensing volumes and flow rates to achieve desired therapeutic levels at known distances from the delivery port.

Yet few techniques are available to determine the absolute local concentration of a diffusing species in medium. Perhaps, the most direct approach is through chemical sampling by use of small capillaries inserted near the injected profile [44]. However, this technique requires high precision placement of the sampling capillary, interferes with the diffusing species in the profile, and must account for the diffusion occurring in the sampling capillary on its way to a detector before an absolute concentration can be determined. On the other hand, less intrusive optical techniques based on fluorescence microscopy may also be used to determine concentration profiles [45]. However, most of these techniques are only capable of obtaining relative concentration profiles, and only very limited examples have been able to determine an absolute concentration level of the diffusing species [40].

Developing a predictive model for the mass transport of a diffusing species based on particular dispensing parameters would also be very advantageous for the larger investigation

aims. Validating the mass transport model with a developed experimental tool for measuring concentration profiles would provide a significant advancement for investigators.

4.2 Experimental Technique to Measure Concentration Profiles

Very few experimental techniques exist for determining an absolute concentration and even fewer non-invasive techniques exist. One such non-invasive technique, developed by Sindhwani et al. [40] is used here with significant modifications for use with discrete dispensing at much smaller time and spatial scales.

4.2.1 Basic Theory

To determine the concentration of a diffusing species in a media, the Beer-Lambert Law may be utilized. The Beer-Lambert Law simply relates the concentration of a species in a media to the amount of light that is absorbed [46] in the following relation:

—

where A is the absorbance or attenuation, I the output or measured intensity of the light, I_0 the input or source intensity of the light, μ the attenuation coefficient, C the concentration of the light absorbing species, and L is the path length of the light through the media with species of concentration C (Figure 31).

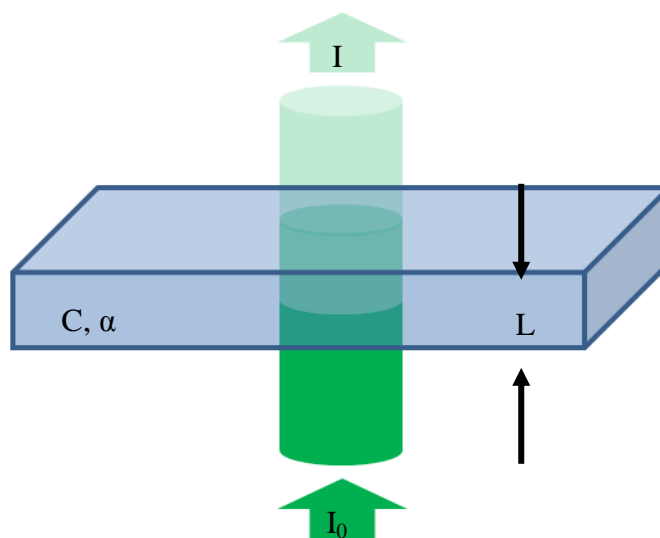


Figure 31 - Illustration of the principle of the Beer-Lambert Law. An incident light beam will undergo a loss in intensity proportional to the concentration of absorbers in a medium of known thickness.

Assuming α , L , and I_0 are known or can be determined, one can then measure the output intensity, I , to determine the concentration of the species in the media. However, several assumptions are made when using this relation that include: 1) a medium with homogeneously distributed species; 2) the species consists of independently acting absorbers that do not scatter incident radiation; 3) the intensity ratio I/I_0 is in the range 0.1 to 1.0, to avoid having too high of a concentration or medium thickness that results in absorbers shadowing each other; 4) the incident light is monochromatic to ensure absorption by the species near a peak absorption wavelength and to reduce scattering; 5) the incident light is collimated perpendicular to the medium so that adjacent rays of light travel the same path length through the medium [46].

4.2.2 Experimental Setup and Method

The target media of interest in this experiment is 0.6 %wt agarose gel and is prepared using the method described in section 3.2.5. The gel is poured and molded into small custom built glass cuvettes with dimensions 6 X 25 X 75 mm. The species used for testing is

bromophenol blue (BRB). BRB has a peak absorption wavelength at 579 nm. Accordingly, a mercury lamp source is used which has a peak emission at 575 nm. The other peaks are filtered out using two bandpass (50 nm width) linear filters (Edmund Optics Inc.) that allow light at 550 nm and 600 nm peaks to pass, thereby creating a 575 nm light source. Also, an aspheric collimating lens (ThorLabs Ltd.) is used to collimate the light that is incident on the cuvettes. Therefore the light travels through several elements, starting from the lamp source, fiber optic, 550 nm and 600 nm bandpass filters, collimating lens, glass cuvettes with the gel sample, through the optics system in the microscope (SMZ 1500 Stereoscopic, Nikon Inc.), and finally to the microscope camera (10Mpx DS-Ri1, Nikon Inc.) where the intensity at each pixel is measured (Figure 32).

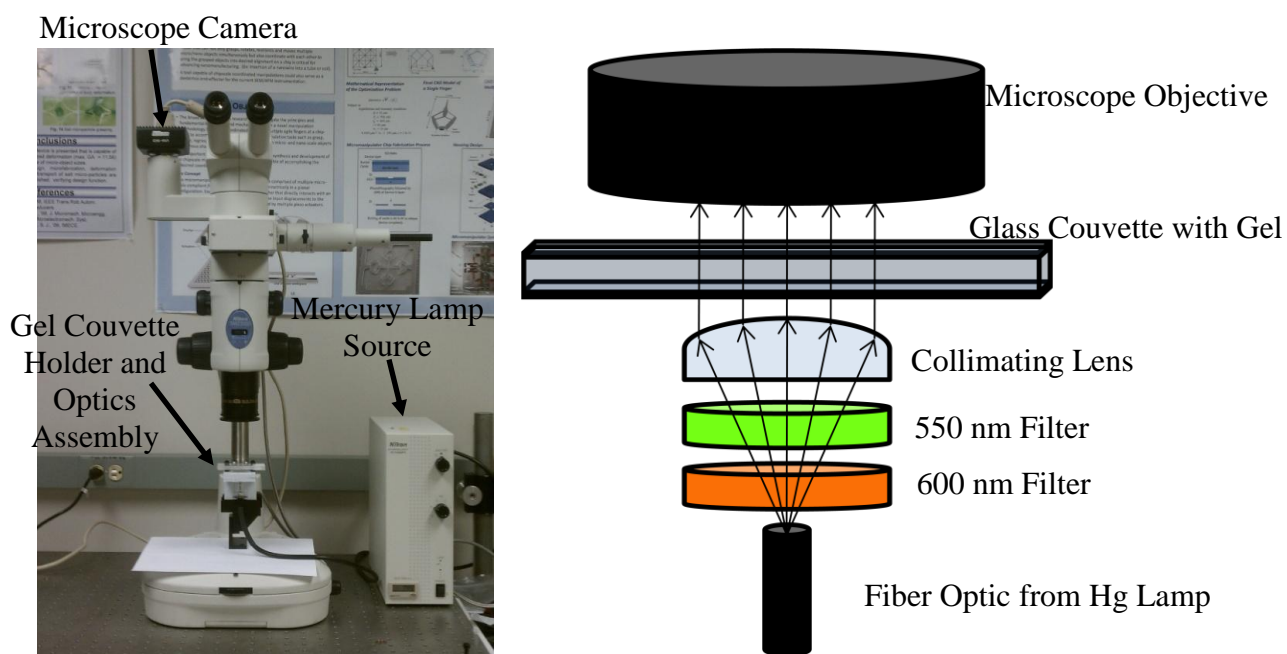


Figure 32 – (Left) Experimental setup for the calibration of the microscope camera and determining the absorption coefficient, α . (Right) The optics assembly included the fiber optic from the lamp source aligned with the filters and collimating lens.

Since each camera may vary in its capturing characteristics [46], a calibration curve for determining the attenuation coefficient per length of media, α , must be determined. For this calibration test, the cuvettes are loaded with a clear gel or a BRB dyed gel of known concentration. The clear gel in the cuvette is placed with the 6 mm thickness perpendicular to the optical path of the incident 575 nm light and an image is captured of the light through the gel. This image and the pixel intensities associated therewith are used as the initial intensities, I_0 . It is important to note that this reference intensity image does not reach the maximum intensity value (255 for 8 bits per pixel scale) for any of the pixels. Next, four different 0.6 wt% agarose gels having four different homogenous BRB concentrations (0.005, 0.010, 0.015, and 0.020 wt%) are loaded into the cuvettes and are similarly placed into the light path and images recorded and the intensity value determined for each pixel, I . All the recorded images are imported into Matlab® (The MathWorks Inc.), converted to grayscale, cropped to the area of the focal plane where measurements will be made, and the value of the expression $-\frac{1}{L} \ln(I/I_0)$ is evaluated for each pixel in each of the four images. These values are then averaged amongst pixels of the same image and plotted against the known concentration of the gels with one standard deviation plotted for error bars (Figure 33).

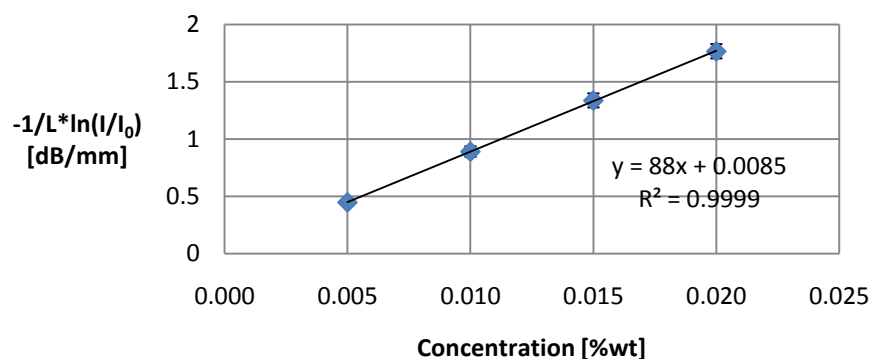


Figure 33 - The calibration curve that determines the absorption coefficient, α , per unit length. The concentration was varied and the drop in intensity was measured.

Having calibrated the camera to determine a value for α , this experimental approach may now be applied to examine injected profiles of unknown concentrations. The experimental setup is kept the same, except now clear 0.6 %wt agarose gels are loaded into the glass cuvettes and a 75/150 μm inner/outer diameter capillary is attached at one end to the syringe pump dispenser (Figure 34). The time constant for this capillary attached to the dispenser was determined to be 74.7 microseconds, which validates fluid incompressibility for this system. The other end of the capillary is then slowly inserted with a micro-positioner into the center of the gel in the cuvette until the capillary tip is brought into the center of the field of view of the microscope (Figure 35).

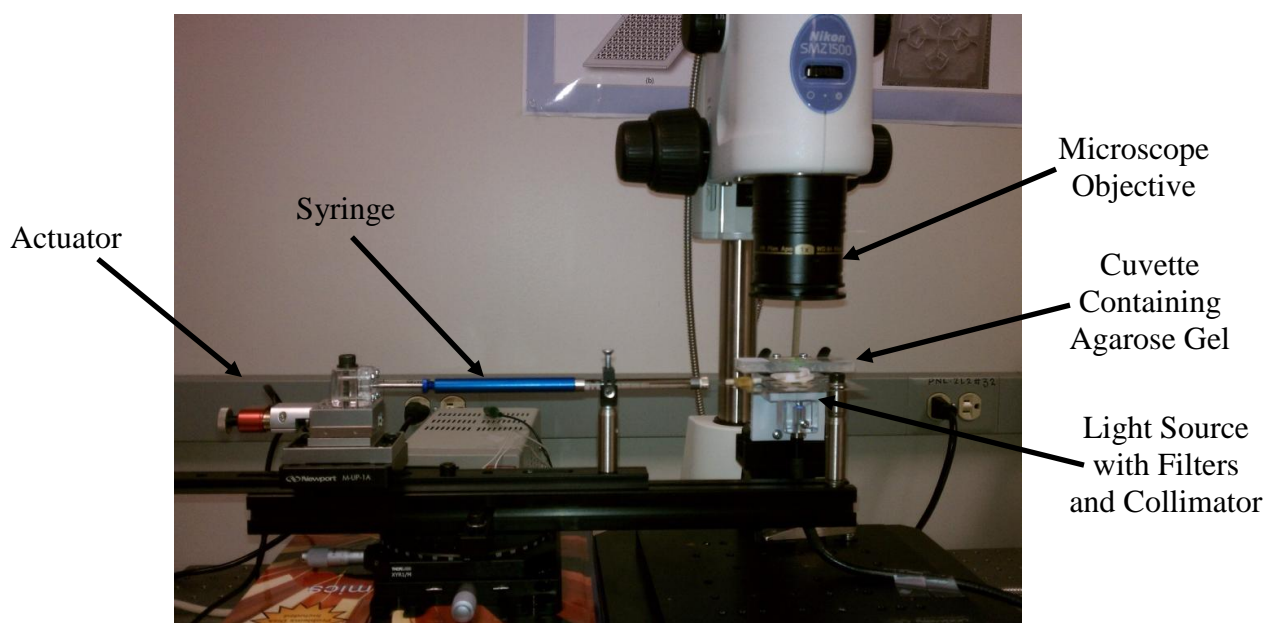


Figure 34 - Image of the entire experimental setup for capturing injection profiles in agarose gel during syringe pump dispenser operation.

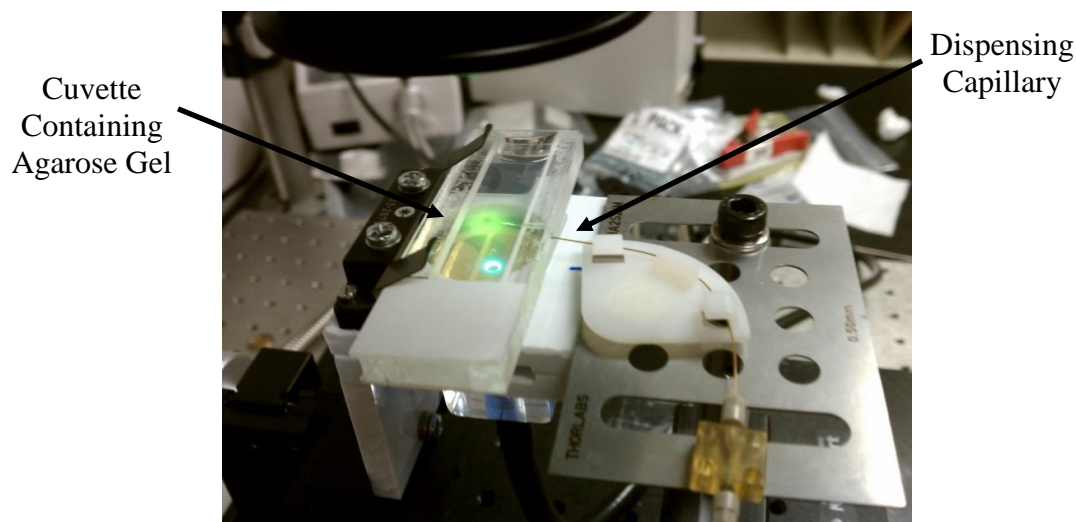


Figure 35 - Closeup of the cuvette containing gel with the dispensing capillary inserted into gel and the capillary tip in the collimated light path.

The syringe pump dispenser, having been loaded with 0.42 %wt. BRB solution (the concentration, C , is scaled in appropriate relation to the much smaller expected path length, L , so that the same linear region of attenuation plotted in Figure 33 is achieved), was commanded to displace the syringe plunger $10\ \mu\text{m}$ that corresponds to a dispensed volume of $1.66\ \text{nL}$. This volume was chosen based on preliminary investigations that revealed it to be the smallest volume that was reliably detectable given the capillary insertion and magnification constraints of the positioning and microscope systems, respectively. The input velocity of the actuator to the system was $100\ \text{cycles/second}$ that corresponds to a plunger velocity of $10\ \mu\text{m/sec}$ or a flow rate of $0.5\ \text{nL/sec}$. Multiple $1.66\ \text{nL}$ pulses, separated by three seconds, were delivered to the gel. Videos of the ejections were recorded at a frame rate of approximately $10\ \text{fps}$ (Figure 38). The input velocity, and hence the flow rate, were then varied for a total of five trials that used input velocities of 100 , 250 , 500 , 1000 , and $2000\ \text{cycles/sec}$ that correspond to 37.8 , 94.5 , 189.1 , 378.2 , and $756.4\ \mu\text{m/sec}$, average injection velocities, respectively.

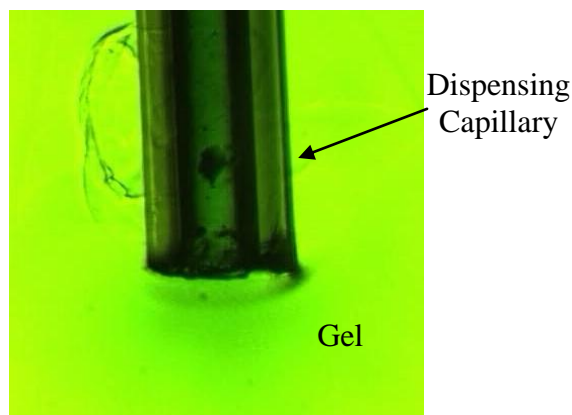


Figure 36 - Representative image of the videos recorded during dispensing. Notice the blue dye profile developing at the end of the capillary inside the gel. The outer diameter of the capillary is 150.5 μm .

4.2.3 Image Processing and Conversion of Images into Concentration Profiles

The first step in the image processing sequence is to splice the recorded videos of the 1.66 nL injections at input velocities of 100, 250, 500, 1000, and 2000 cycles/sec into a series of 640X512 pixel image frames at a frame rate of 10 fps. Next, these images are edited to identify exactly when dispensing starts and ends for the initial discrete volume injection. About two seconds of frames immediately before the dispensing start time are also included for use as a noise filter, which will be discussed in more detail below. These images, taken together, form the complete image set.

A MATLAB® program (see Appendix A.3) is written to import the image set and perform the remaining image processing techniques. All of the imported images are converted to grayscale, cropped to a 150 X 150 pixel image in the region of interest, rotated 180°, and then stored in a three dimensional matrix that lists the intensity value for each pixel in a 2D image for all images that are time sequenced in the third matrix dimension. The resolution of the images is approximately 1 μm /pixel. The region of interest, therefore, is a 150 X 150 μm 2D axis-

symmetric space from the centerline of the capillary (Figure 37), since the ejection profile is assumed to be symmetric.

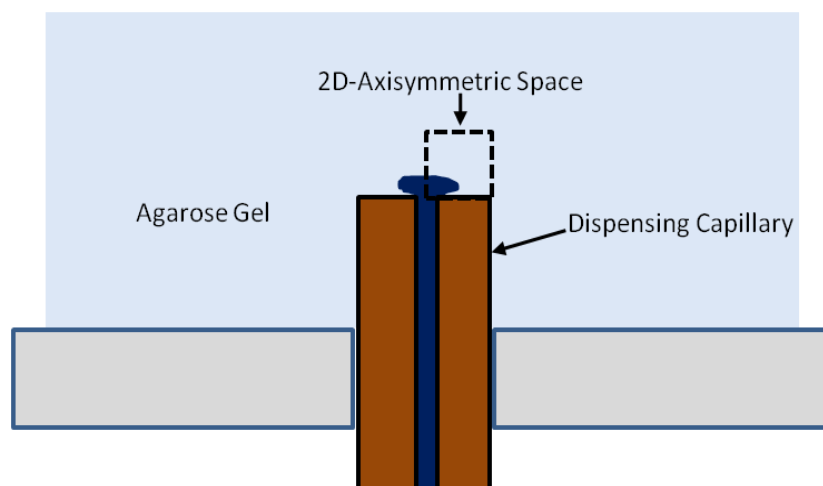


Figure 37 - Illustration of the space that is captured for image processing and conversion to concentration values.

Since the concentration value for a pixel is based on a relative change in intensity at that pixel, the resulting concentration image will be very sensitive to any sharp changes in intensities. These sharp changes in intensities often occur at edges that bound light and dark areas, such as where there are wrinkles or deformations in the gel caused by the capillary insertion. When there is mechanical noise, such as micro-motion or vibrations that cause these edge areas of the image to move amongst neighboring pixels, this will appear as a rapid change in concentration, even though physically, no such change is occurring. In order to reduce this error, the initial pre-dispensing images that comprise the first two seconds of the image set are sampled for noise. The standard deviation of each pixel across images in this time period is determined. The rest of the images in the image set that occur during dispensing have a filter based on the standard deviation applied to each pixel in them ($I_{m,n,j}$ is the intensity value of the pixel in the m^{th} row, n^{th} column, of the j^{th} image):

If: $I_{m,n,j} < (I_{m,n,j-1} - \text{STDEV}(I_{m,n}))$

Then: $I_{m,n,j} = I_{m,n,j}$ (accept the intensity value at this pixel for the current image)

Else: $I_{m,n,j} = I_{m,n,j-1}$ (reject the intensity value at this pixel, set equal to previous image)

Therefore, the noise filter defines that the change in intensity between images at two different times must be greater than the standard deviation of the noise images in order to be accepted as a true value of the intensity change.

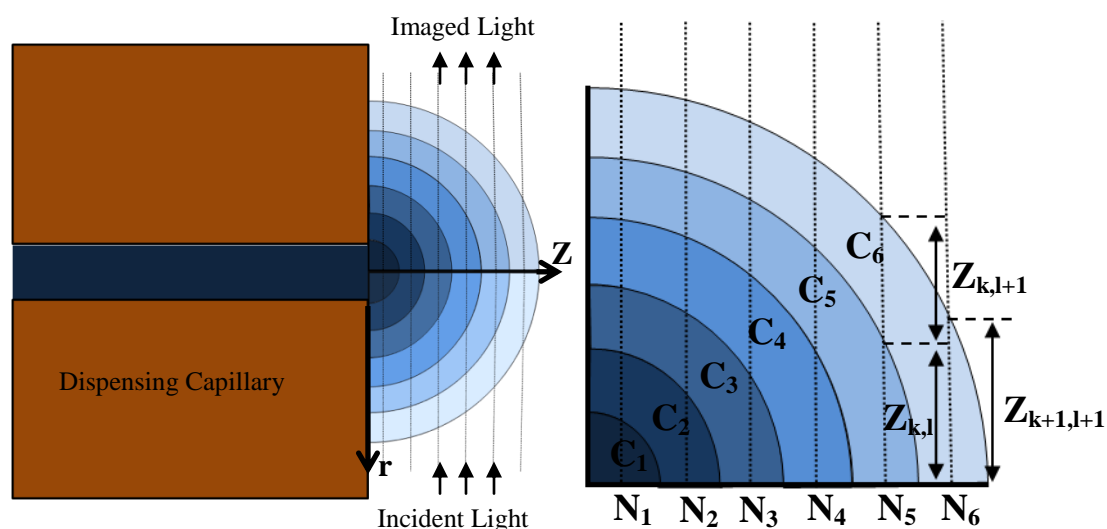


Figure 38 - (Left) Schematic of the concentration profile is forming at the end of the dispensing capillary in the gel. Incident light will pass through this profile formed by an N number of concentration shells that is the same number of pixels along the z-axis that the profile is imaged on. (Right) The light path ($Z_{k,l}$) varies through each ring of the concentration shell, but can be determined through trigonometry if a symmetric profile is assumed.

After the noise filtering is performed, the intensity images are ready to be converted into concentration images via the Beer-Lambert Law. However, it is important to realize that concentration is not homogenous in the region of interest, the space directly adjacent to the exit port of the dispensing capillary, and therefore, the path length through these regions of different concentrations are varied as well (Figure 38). Nevertheless, if one assumes that the concentration profile is symmetric and consists of N hemispherical shells of pixel width thickness, one can

determine the path length, $Z_{k,l}$, through each concentration shell (Figure 38). This can now be applied in the Beer-Lambert equation, which can be represented as a matrix of the form [40]:

$$\begin{matrix} & \text{---} & \\ & \text{---} & \end{matrix}$$

The concentration can then be solved for by inverting the matrix equation. This geometry correction technique was developed by Sindhvani et al. [40] to apply to steady state convection enhanced delivery into gels. However, this technique is modified in application to the image frames in several key ways to account for the transient effects of pulsed flow delivery. 1) The first frame just before dispensing commences is used as the reference intensity, I_0 , to calculate the concentrations for the remaining images instead of using the edge of the image as a reference intensity. 2) Since the concentration profile is growing as dispensing is occurring, the front of the concentration profile must be tracked and the profile is assumed to end where the intensity value along the centerline pixels has reached 90% of the value of the background intensity. 3) The path length, $Z_{k,l}$, is also scaled based on this criteria so that it is $N \times N$ pixels in dimension with N corresponding to the number of pixels along the centerline that was determined in 2). The corrected concentration profile along the centerline as a function of time could thus be determined after matrix inversion.

4.2.4 Results and Discussion

The centerline values (the values along the z-axis, $r = 0$, Figure 38) for the concentration profile as a function of time is plotted in Figure 39 for each of the velocity inputs. Each line plotted indicates a 100 ms time step; therefore, the five separate plots show the progression of the concentration profile into the gel over a 3.5 second time span using the five different exit velocities (flow rates). The concentration ranged from 0 to 6.3 mM, the source concentration of BRB in the capillary.

As Figure 39 reveals, and perhaps counter intuitively, the slowest exit velocity resulted in the farthest penetration into the gel for a single volume pulse in the same amount of time (3.5 seconds). However, it is important to note that the same volume (1.66 nL) was injected into the gel for each of the five separate injection velocities. Thus, if diffusion is very slow through the gel and has little influence, one would expect that after all the discrete volume pulses at different injection velocities have finished dispensing, the same concentration profile should result. The faster injection velocities will be faster in reaching this concentration profile initially, but the slow diffusion will keep this profile intact for a substantial amount of time, giving enough time for the slower advancing profiles to catch up.

Consequently, if the faster injection velocities result in smaller concentration profiles, this could indicate leakage of volume somewhere in the system. One possible source of leakage was revealed in the flow rate experiments conducted in section 3.2.5. The results showed little fluid resistance through the gel even at high flow injection velocities, which suggested that the gel was being deformed and displaced from the momentum of the injected fluid.

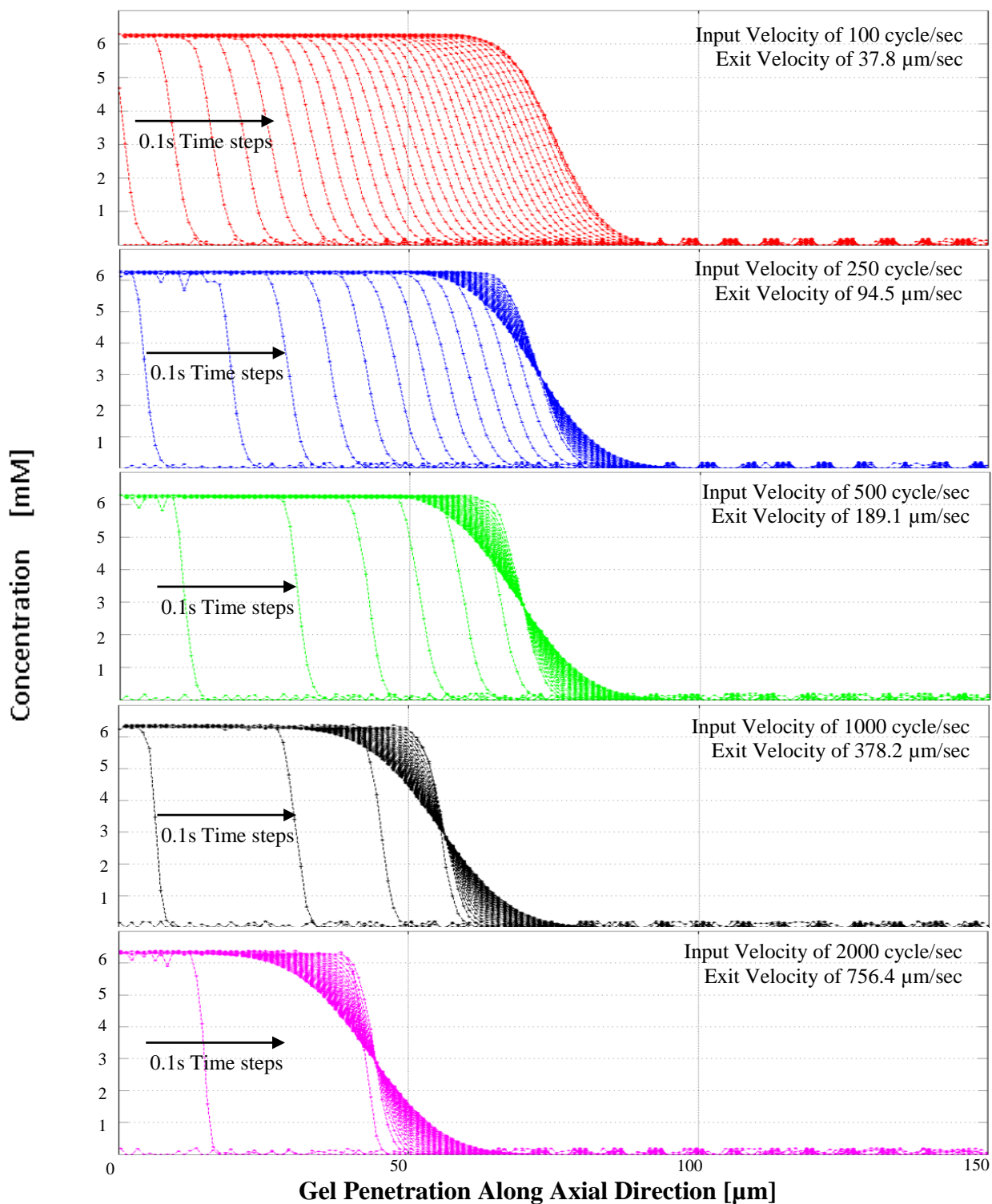


Figure 39 - Experimentally determined concentration profiles along the axial direction is plotted as a function of time (0.1s time steps). The slowest injection speed resulted in the farthest penetration into the gel even though the same volume was injected for each trial.

Also, other investigators have discovered the phenomena of reflux when delivering a species to a viscoelastic material or tissue [47]. Essentially, reflux is the propensity of an injecting fluid from a conduit inserted into a porous material to flow back down the walls of the conduit, as opposed to flowing into the porous material.

In fact, when multiple volume pulses were injected into the gel from the capillary, videos were captured of the dye solution clearly flowing up the sidewalls of the capillary. This reflux effect was much more pronounced for the higher injection velocities (378.2 and 756.4 $\mu\text{m/s}$) than the lower injection velocities (37.8, 94.5, and 189.1 $\mu\text{m/s}$) (Figure 40).

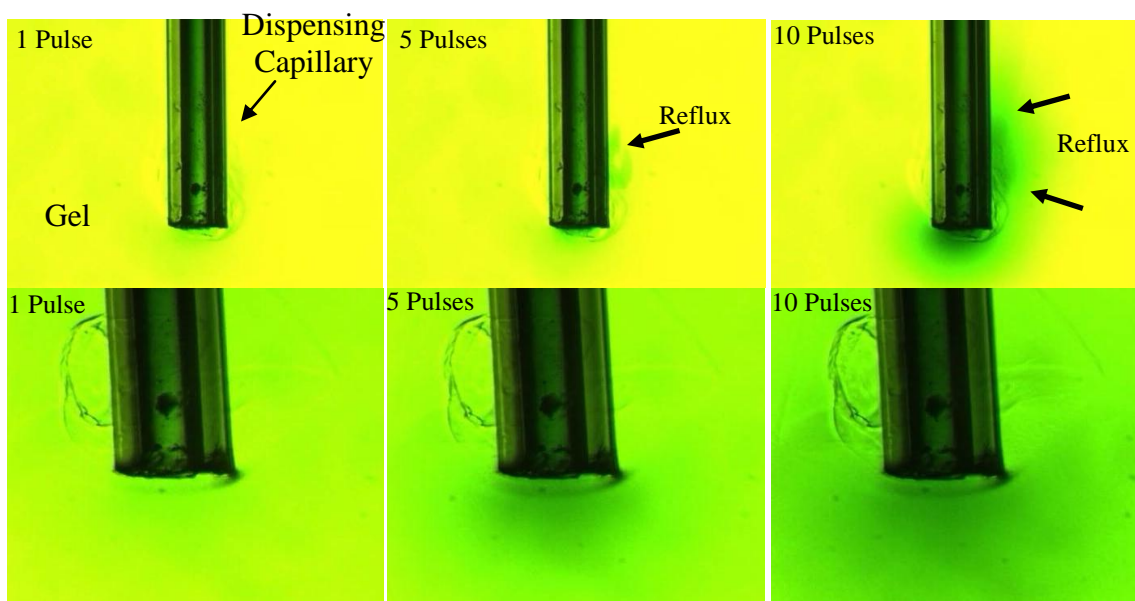


Figure 40 - Images captured during recording of multiple 1.66 nL injections from the dispensing capillary. (Top) Using an injection velocity of 378.2 $\mu\text{m/s}$, reflux occurs, resulting in volume that does not contribute to the profile at the end of the dispensing capillary. (Bottom) Using an injection velocity of 37.8 $\mu\text{m/s}$, results in a dispensing profile with significantly less reflux. The outer diameter of the capillary is 150.5 μm .

Therefore, reflux may account for most of the volume loss and the resulting shorter penetration of the species into the gel for higher velocities. Thus, the reflux action at higher injection velocities may limit the effect of using high flow rates to quickly raise the

concentration level at a distance away from the capillary. Injecting velocities at least below 189.1 $\mu\text{m/s}$ seemed to have very little reflux effects and lost volume. More insight into the physics of this effect may be gained through use of an appropriate model.

4.3 Theoretical Modeling of Concentration Profiles in Agarose Gel

The final objective of this thesis was to develop a model that would allow for prediction of ejected concentration profiles dependent upon dispenser delivery parameters, such as input velocity. Further, a model would allow for more physical insight into the dynamics of how these concentration profiles develop. To this end, a finite element approach was used to build a model in Comsol Multiphysics® that would capture both diffusion and convection effects. The model is then compared with the experimentally obtained concentration profiles through the techniques developed in section 4.2, while key differences are examined.

4.3.1 Model Space, Elements Used, and Governing Equations

The region of interest captured for this model is the three dimensional space directly adjacent the tip of the dispensing capillary (Figure 41). However, since the concentration profiles have proven to be fairly symmetric at the end of the capillary (Figure 36), the model space can be greatly simplified by taking a two dimensional slice, bounded by the axis of symmetry on one side, of the 3D space. Thus, the model space is completely in the porous agarose gel medium comprising a simple rectangle whose length and width will be determined after further refinement of the model.

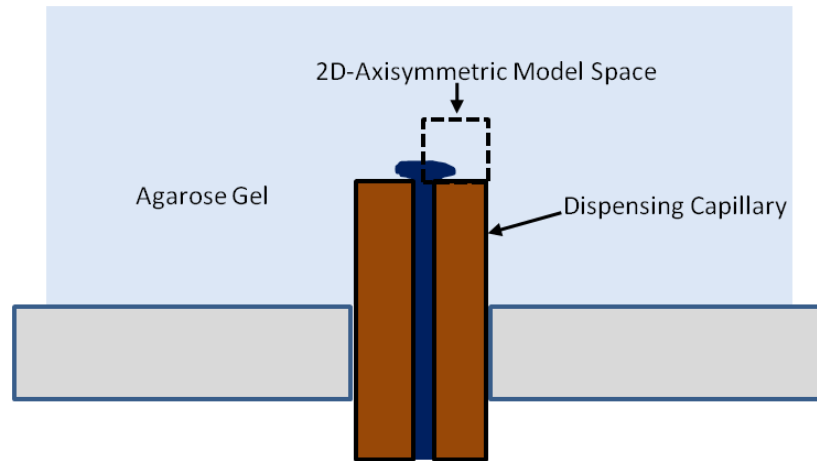


Figure 41 - The space being modeled is entirely in the gel and is the same space that was analyzed during the experiments (see Figure 37).

The model captures both the diffusion and convection components of the species transport. Two dimensional Lagrange, quadratic-based triangular elements were used to model the system. These element types are able to model mass and fluid transport coupled problems. Thus, the full mass transport equation governs how the concentration profile will form:

$$\begin{array}{c}
 \text{Mass Transport Equation} \\
 \frac{\partial c}{\partial t} + \nabla \cdot (-D_{\text{eff}} \nabla c) + \mathbf{u} \cdot \nabla c = R \\
 \underbrace{\hspace{1.5cm}} \quad \underbrace{\hspace{3.5cm}} \quad \underbrace{\hspace{1.5cm}} \quad \underbrace{\hspace{0.5cm}} \\
 \text{Storage} \quad \text{Diffusion} \quad \text{Convection} \quad \text{Generation}
 \end{array}$$

where c is the concentration, D_{eff} the effective diffusivity of the BRB dye in the agarose gel, and the generation term, R , is equal to zero. Since the convection term is reliant upon knowing the velocity field, \mathbf{u} , in the region of interest, the mass transport equation must be coupled with the Navier-Stokes (momentum) equation that determines the velocity field. In addition to the normal assumptions (incompressible, Newtonian fluid) built into the Navier-Stokes equation, an extra term (Darcy term) to account for the porous medium of the gel is used:

$$\underbrace{\rho \frac{\partial \mathbf{u}}{\partial t}}_{\text{Transient}} + \underbrace{\left(\frac{\mu}{\kappa} \right) \mathbf{u}}_{\text{Darcy Term}} = \nabla \cdot \left[\underbrace{-P \mathbf{I}}_{\text{Pressure}} + \underbrace{\mu (\nabla \mathbf{u} + (\nabla \mathbf{u})^T)}_{\text{Viscous}} \right]$$

Navier Stokes Equation

where ρ is the density, μ the dynamic viscosity, κ the permeability of the gel, and P is the pressure. Thus, these two coupled equations govern the flow of fluid and dye in the porous medium. It is important to note that the gel is rigid in this model and only transport processes are able to be modeled with these elements.

4.3.2 Physical Properties, Boundary Conditions, and Velocity Input

In this model, the fluid being investigated here is de-ionized water, the species transport is that of bromophenol blue dye in the de-ionized water, and the medium in which the fluid and species transport is taking place in is 0.6 wt% agarose gel. The isotropic physical properties of the gel, fluid, and dye are summarized in Table II.

Table II - PROPERTIES USED IN THE FEA MODEL.

Property	Symbol	Value [units]
Effective Diffusivity of Bromophenol Blue in 0.6 wt% Agarose Gel	D_{eff}	$1.6 \cdot 10^{-11} [\text{m}^2/\text{s}]$ [42]
Permeability of 0.6 wt% Agarose Gel	κ	$1.0 \cdot 10^{-14} [\text{m}^2]$ [42]
Dynamic Viscosity of Water at 20°C	μ	$1.002 \cdot 10^{-3} [\text{N}\cdot\text{s}/\text{m}^2]$ [41]
Density of Water at 20°C	ρ	$998.2 [\text{kg}/\text{m}^3]$ [41]

There are two initial conditions and ten boundary conditions (five boundaries each with two conditions for the two governing equations) that are applied to the rectangular model space. (Figure 42) The initial conditions are that the concentration, c , and the velocity, \mathbf{u} , are both zero

everywhere ($c=0$, $\mathbf{u}=0$) in the region. For the boundary conditions: one side of the rectangle is the line of symmetry and thus has a mass insulating condition (species flux = 0) and a fluid slip condition ($\mathbf{u}_{\text{radial direction}}=0$). Another two sides of the rectangle are far enough away from the dispensing capillary so that the pressure and concentration are both zero ($c=0$, $P=0$). The final side of the rectangle is the boundary with the dispensing capillary and thus, is comprised of two separate boundaries: the inner radius of the capillary ($37.5 \mu\text{m}$) that is introducing flow into the region, and the space between the inner and outer radii of the capillary that comprises the glass wall that forms the end tip of the capillary. The glass wall boundary has a mass insulating condition (species flux = 0) and a fluid no slip condition ($\mathbf{u} = 0$), while the inner diameter boundary has a uniform time varying velocity input condition, $\mathbf{u}_z = u_{\text{port}}(t)$, and mass influx condition of $c_{\text{source}} \cdot u_{\text{port}}(t)$, where c_{source} is the concentration (6.295 mM) of the BRB dye in the water that is flowing into the region.

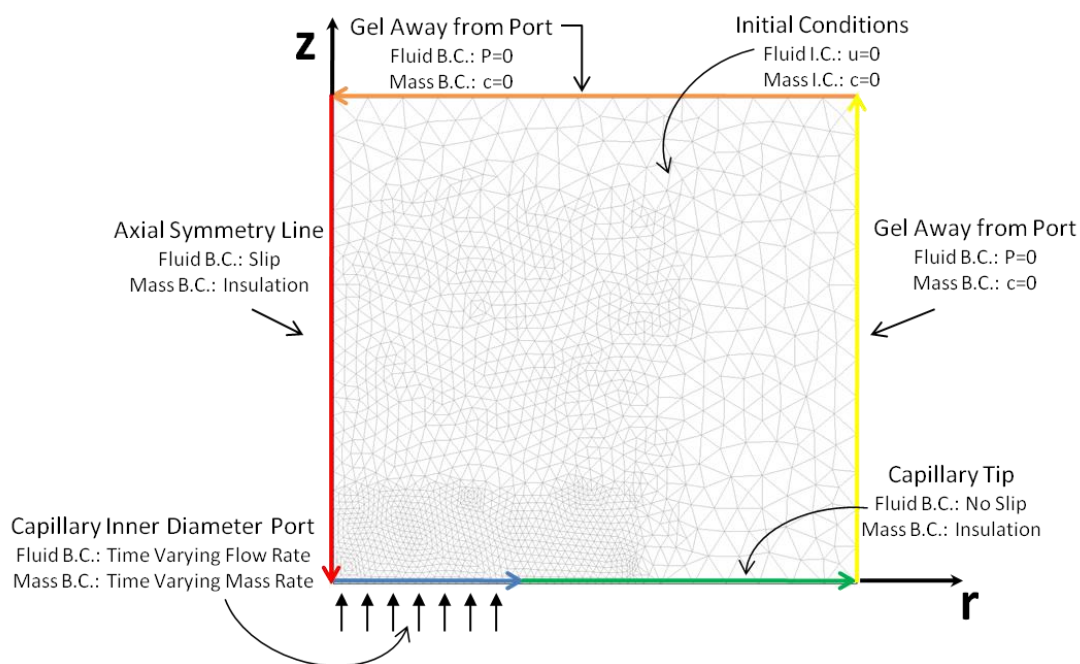


Figure 42 - Illustration of the model space with the applied initial and boundary conditions. There are a total of two initial conditions applied to the model space, one each for each governing equation, and two boundary conditions applied to each of the five boundaries.

The varying velocity input condition $u_{\text{port}}(t)$, is approximated as a logistic step function:

$$\text{—————} \quad \text{—————}$$

where a is the plateau (average exit velocity at the port of the capillary) of the step function, b controls the rise and fall times, and t_{ON} and t_{OFF} are the on and off times of the step function. Five different $u_{\text{port}}(t)$ inputs, resulting in five different concentration profiles over time, are used in this investigation. The same input velocities of 100, 250, 500, 1000, and 2000 cycles/sec that correspond to 37.8, 94.5, 189.1, 378.2, and 756.4 $\mu\text{m}/\text{sec}$ average exit velocities, respectively, used for the experimental procedure are also used for the model input as the a value for each of the five $u_{\text{port}}(t)$ equation. The b value used for all the inputs is 1000 that resulted in a rise and fall time of approximately 10 msec. For all the inputs, the step onset time, t_{ON} , is 0.05 seconds. The step off time, t_{OFF} , is accordingly adjusted for each $u_{\text{port}}(t)$ input, so that each pulse injects a volume of 1.66 nL, the same volume that was injected in the experimental studies. These step off times were found by integrating the flow rate (product of $u_{\text{port}}(t)$ and the area at the capillary exit port) over the time interval, t_{ON} to t_{OFF} , to yield a volume of 1.66 nL. This resulted in t_{OFF} times of 3.2, 1.31, 0.68, 0.41, and 0.21 seconds for the input velocities of 100, 250, 500, 1000, and 2000 cycles/sec (37.8, 94.5, 189.1, 378.2, and 756.4 $\mu\text{m}/\text{sec}$ exit velocities). Use of the logistic step function allows for easier convergence of the model and a better approximation of how the actuator and dispensing system physically responds when compared to a simple instantaneous step function of the velocity.

4.3.3 Mesh and Element Refinement

After the initial and boundary conditions have been assigned to the model, the model space is ready to be meshed. An unstructured 2D triangular mesh consisting of 9809 elements covered the 2D axis-symmetric model space (Figure 43). The number of elements in the mesh was arrived after several area applied refinements (especially near the capillary inner diameter boundary) until the concentration values varied by no more than 1% for a given node when the model was solved. A similar refinement of the vertical and horizontal scale of the model was also done [48]. The concentration values varied by less than 1% between reiterations when the horizontal and vertical scales reached a size of approximately $150\ \mu\text{m} \times 150\ \mu\text{m}$ for the rectangular model space.

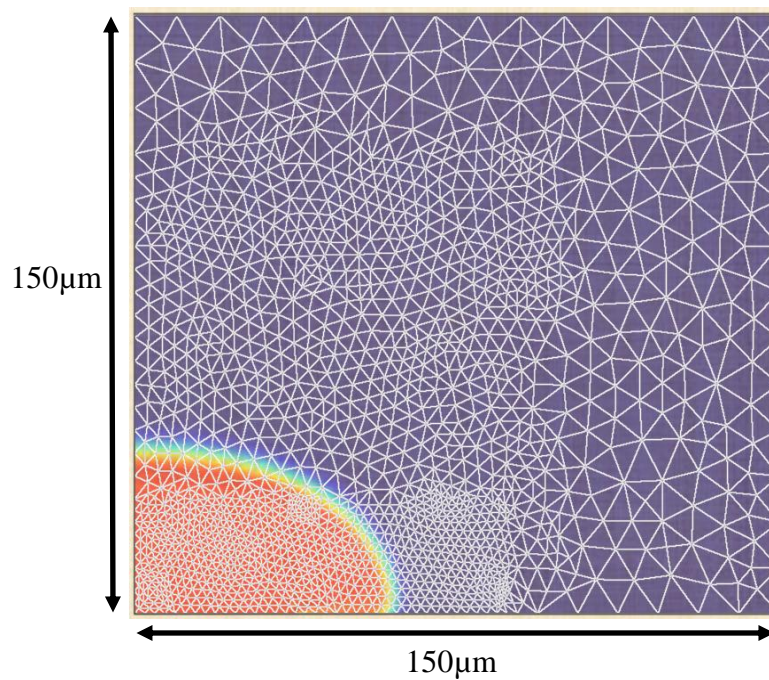


Figure 43 - An unstructured triangular mesh was used to cover the $150 \times 150\ \mu\text{m}$ model space.

Finally, the elements used in this mesh were Lagrange, quadratic-based triangles. Use of cubic or quartic based triangles resulted in longer computation time that produced similar solutions; therefore, quadratic-based triangles were used to obtain solutions.

4.3.4 Results and Discussion

With the region appropriately meshed, the model was solved over 3.5 seconds with time steps of 5 milliseconds. This time step was arrived at again through a reiterative process so that concentration values did not vary by more than 1% below this time step value. A 2-D contour plot of the concentration profile in the region of interest is shown in Figure 44 for the 100 cycle/sec input (37.8 $\mu\text{m/s}$ injection velocity) for selected time steps. The profiles obtained for the other injection velocities were very similar, except with velocity proportional growth rates. The profile proved to be asymmetric for the beginning of the flow due to the inner radius of the capillary, but quickly becomes symmetric as the profile expands. This suggests, however, that use of small volume injections and relatively large inner diameter capillaries would lead to high asymmetries and large errors if using the symmetric experimental techniques developed in section 4.2.3. Also of interest in these plots, is how steep the concentration gradient is along the expanding volume boundary, indicating the slow diffusion on these time scales. This slow diffusion rate is expected, considering the small diffusivity ($D=1.6*10^{-11} \text{ m}^2/\text{s}$) of the BRB dye in this gel. Note, however, that glutamate in the synapse is thought to have a diffusivity on the order of $\sim 1*10^{-10} \text{ m}^2/\text{s}$ [49], although the effective diffusivity could be much lower outside the synapse, since various structures and cells at the tissue level will interfere with molecular diffusion.

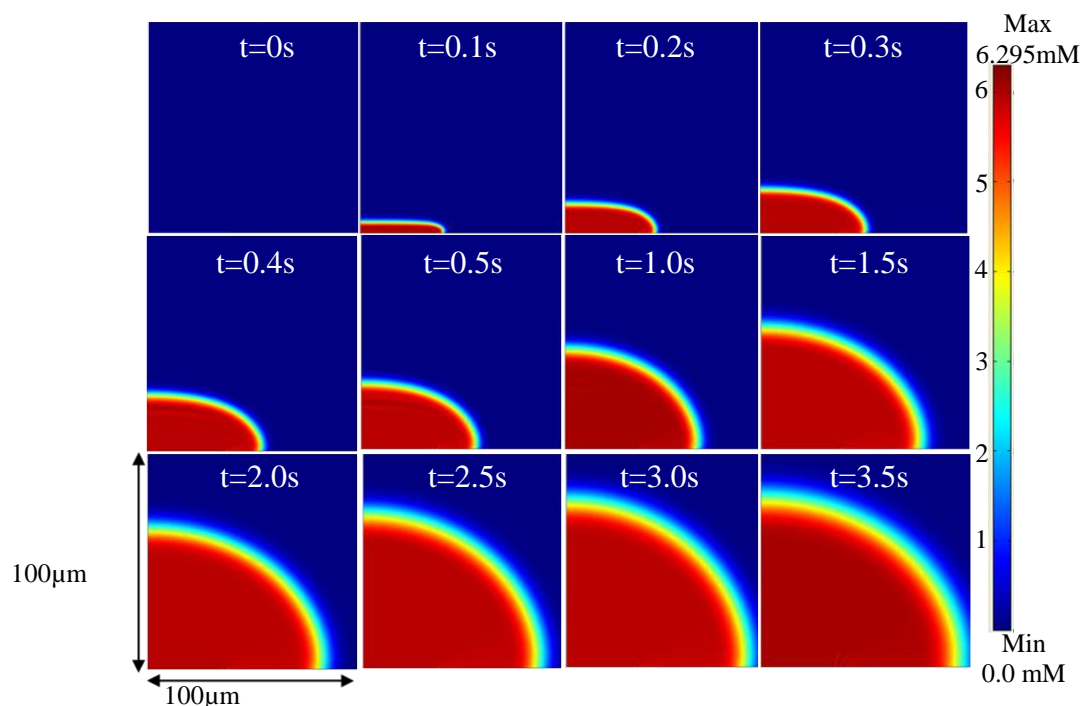


Figure 44 - A 2-D contour plot of the concentration in the model space for selected times. Although, initially asymmetric, the profile quickly becomes symmetric. The slow diffusion rate on this timescale is evidenced by the steep concentration gradient along the growing boundary.

The data from the model simulation is plotted in Figure 45 for the centerline for the concentration profile of the last time step ($t = 3.5$ sec) for each of the velocity inputs. Figure 45 reveals that the final time step for all five of the input velocities in the FEA model are essentially the same with a penetration of $63 \mu\text{m}$ at 95% of the source concentration (~ 6 mM) and a penetration of $88 \mu\text{m}$ at 50% of the source concentration (~ 3.1 mM).

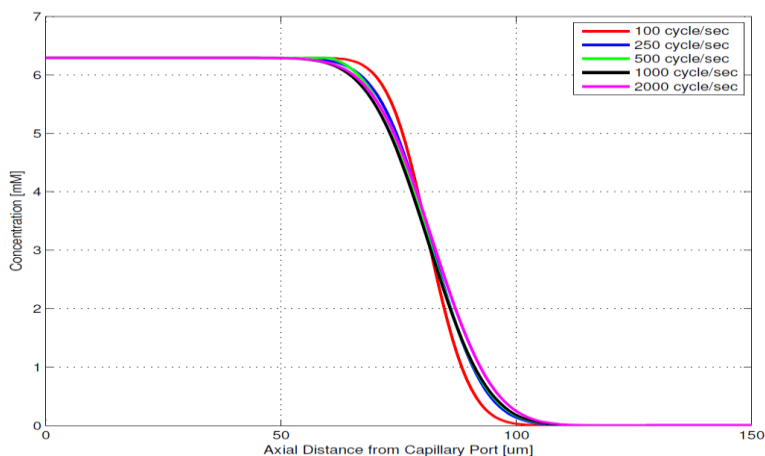


Figure 45 - A plot, obtained from the FEA model, of the concentration profiles along the axial centerline at the final time step ($t=3.5s$) for different dispenser input velocities (resulting in different injections velocities). Because the same volume was delivered during the single injected pulse, the same concentration profile was obtained for all injection velocities.

4.3.5 Experiment-Model Correlation

The result obtained in Figure 45 is quite different from the experimental plots that showed different penetration distances into the gel for different injection velocities. Figure 46 plots the experimentally obtained concentration profiles at $t = 3.5$ seconds for each of the injection velocities with an average of the concentration profiles obtained in Figure 45 for the FEA model. The amount of error between the model and the experimentally derived concentration profiles depended upon the input velocity. For the 100 cycles/sec input ($37.8 \mu\text{m/s}$ injection velocity), the error in predicting the concentration at a distance into the gel was no more than $\sim 10\%$, while for the 2000 cycles/sec input ($756.4 \mu\text{m/s}$ injection velocity) the error was greater than 50% . Again, this larger error for higher injection velocities is thought to occur because of the reflux effect (see section 4.2.4) and deformation. The FEA model assumes that the gel is a rigid porous solid that cannot account for any volume losses due to gel deformation from the momentum of the impinging fluid stream from the dispensing capillary. Therefore, this is an

expected difference between the FEM and measured profiles. Future models may couple the physics of hydrodynamics and mass transport with viscoelastic deformation of the porous gel.

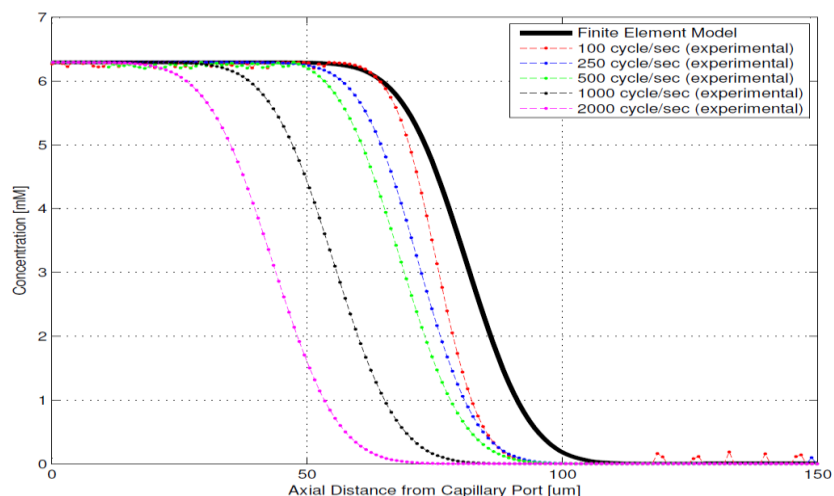


Figure 46 - A plot of the concentration profiles along the axial centerline at the final time step ($t=3.5s$) for different dispenser input velocities (resulting in different injection velocities). An average of the results obtained in Figure 45 from the FEA model is compared with the results obtained from the experiments and imaging processing. The lower injection velocities profiles from the experiment were much closer to the result obtained from the model.

As was done with the experimental data in section 4.3, the data from the model simulation is plotted for the centerline values (the values along the z -axis, $r = 0$, Figure 42) for the concentration profile as a function of time is plotted in Figure 47 for each of the velocity inputs. Very similar shaped profiles were obtained with the results from the model. The plots revealed an interesting relationship between the convective and diffusive species transport in the gel. Convection is seen to clearly dominate the growth of the profile during dispensing for these time and spatial scales. Diffusion seems to only slightly smear the front of the profile as it advances during dispensing. As speculated in section 4.2.4, the model confirms that the faster injection velocities will be faster in reaching this concentration profile initially, but the slow diffusion will keep this profile intact for a substantial amount of time, giving enough time for the slower advancing profiles to catch up.

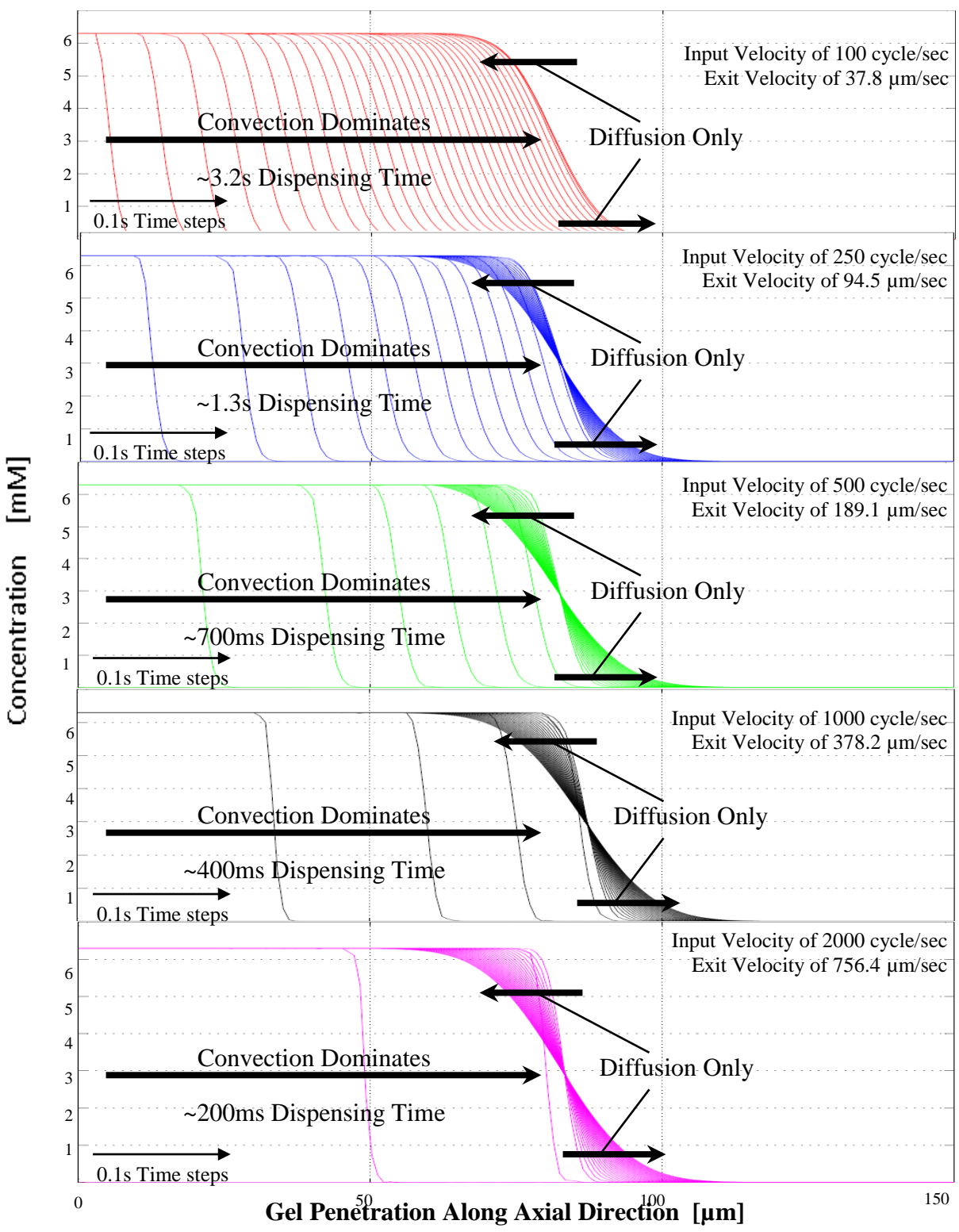


Figure 47 - Plots of the concentration profile obtained through the FEA model. The convection dominates the progression of the profile, since almost all of the penetration into the gel occurs during dispensing. The contribution of only the diffusion can be seen in the later time steps after dispensing stops.

According to the model, this leads to the conclusion that the amount of injected volume plays the biggest role in determining how far the species will penetrate into gel. Due to the sharp concentration profile as a result of the slow diffusion, using a higher source concentration would have only a very limited effect on increasing the depth of penetration. According to the experimentally obtained profiles, the injection velocity plays a secondary role in determining the penetration distance. Slower injection velocities result in farther penetration into the gel if a single pulse of the same volume is delivered. However, it is important to realize that use of faster injection velocities could deliver more volume to the gel in the same amount of time, resulting in farther penetration of the dye into the gel in short time spans. Yet, if efficient delivery of the species is desired, since there is a limited supply of the species, these faster injection velocities will experience more volume loss that does not contribute to the profile being penetrated into the gel away from the capillary.

Finally, the FEM provides some initial insights into how glutamate concentration profiles may develop in the retina. Although, it is important to keep in mind some of the critical distinctions between the isotropic agarose gel and retinal tissue: 1) glutamate in the synapse is thought to have a higher diffusivity on the order of $\sim 1 \cdot 10^{-10} \text{ m}^2/\text{s}$ (compared to $1.6 \cdot 10^{-11} \text{ m}^2/\text{s}$ for BRB dye in agarose gel), although the effective diffusivity could be much lower outside the synapse [49]; 2) the retina is anisotropic in both its diffusivity and hydraulic conductivity [41, 50-52]; 3) glutamate is actively uptaken and broken down by glutamine synthase at both the synaptic level by neurons and the tissue level by glial cells, which acts as a overall glutamate sink throughout the retina [49]. Future investigative work may quantify these effects and parameters so that a more accurate model of glutamate transport in the retina may be achieved.

CHAPTER 5 - CONCLUSIONS & FUTURE WORK

A brief summary of conclusions drawn from each approach is outlined in this chapter. In addition, improvements and future work are suggested for dispenser design and characterization methods.

5.1 Conclusions

A custom syringe pump was constructed that allowed for variability of dispensing ports through use of replaceable and interchangeable capillaries. The fused silica, polyimide coated capillaries used for this dispenser are commercially available, can be cut to any length, come in a large variety of inner and outer diameters, and their dispensing ends may be ground or etched to modify their delivery port geometry. The flexibility of choosing the delivery channel design and placement allows investigators to quickly determine which delivery port size and shape leads to most advantageous responses from the tissue being treated or signaled. Dispenser testing revealed that the volume dispensed was sufficiently accurate (only 4.1% relative error with a 100 μm inner diameter capillary in the 100 pL – 10 nL range) with respect to the predicted volume based on actuator displacement, while having excellent repeatability (low relative standard deviation). This close match between theoretical and measured volumes at this small scale illustrates that accurate alignment of the actuator and syringe, as well as a leak-proof delivery system, was achieved for capillaries of large inner diameter ($>50 \mu\text{m}$). Therefore, all the design considerations were met, including allowing for a simple interface between the syringe pump and an MEA recording system.

Experimental calibration procedures for determining dispensed volumes and flow rates were developed that can be applied to any future dispenser designs. Application of hydraulic circuit analysis also proved to be useful in calibrating the flow rate dependency on capillary resistance. Hydraulic circuit analysis may be further used to predict differences from input and output flow rates when fluid compliance effects become non-negligible. Use of this approach allows for a simple model that reduces the ability to determine the role fluid-based compliance plays into determination of a single parameter, the time constant $\tau = R \cdot C$. Since, the time constant is very small ($\sim 10 \mu\text{s}$ or less) for dispensing capillaries larger than $20 \mu\text{m}$ inner diameter, the compliance seen from the flow rate measurement experiments in these sizes of capillaries must be attributed to the mechanical compliance in the actuator and syringe plunger rod components. This was accounted for in the calibration of the flow rate dependence on hydraulic resistance and input velocity.

A pulsed flow based imaging method for applying the Beer-Lambert Law to determine diffusing dye concentration profiles in agarose gel was also developed. Even at small length scales ($< 100 \mu\text{m}$), diffusion played a minor role at time scales on the order of a few seconds or less. The amount of volume delivered played the greatest role in determining the penetration distance into the gel of delivered chemical species. Experimentally obtained time dependent concentration profiles were compared to a finite element model. The comparison helped reveal dispenser volume loss phenomena (reflux) that may provide insight into the limits of convection based delivery of chemical species to neuronal tissue.

5.2 Suggestions for Future Work & Designs

In regards to the design and construction of the syringe pump dispenser, leakage issues for capillaries of inner diameter $50 \mu\text{m}$ or less could be reduced by permanently bonding the

removable needle to the syringe barrel or purchasing a syringe that has a cemented needle already in place (Hamilton Company, Reno, Nevada). In addition, mechanical compliance could be reduced by using a shorter syringe plunger rod to reduce the amount of axial compression during actuation. Using a syringe barrel of smaller inner diameter may also be useful in reducing the amount of fluid compliance when using capillaries of inner diameter less than 20 μm . A future chip scale design with multiple dispensing ports should rely on integrated flow rate meters in microchannels [6]. This could provide the necessary real time feedback to a large array of individually controlled dispensing ports for fine tuning of dispensing volumes (integration of the flow rate over time) and injection velocities (flow rate divided by the cross sectional area of dispensing port) as they are dispensed.

Future calibration experiments for measuring volumes and flow rates could be made more accurate ultimately be improved with a microscope objective (a 1.6 X objective is available through Nikon Inc.) that provides for a microscope with higher total magnification than the one used in this work.

This concentration profile measurement technique could be improved in much the same way that the plunger and meniscus tracking techniques could be improved: through better magnification/resolution of the region close to the capillary. It could be further improved with a more accurate positioning system when the capillary is inserted into the gel, to help alignment with the field of view and so that wrinkles near the edge of the capillary are reduced during insertion. Other capillary end port geometries may also be tried in order to reduce the amount of reflux.

Finally, future FEM models may couple the physics of hydrodynamics and mass transport with viscoelastic deformation of the porous gel to obtain more accurate concentration profiles. Additionally, neuronal tissue anisotropic properties and neurotransmitter sources and sinks may be appropriately modeled to obtain more accurate concentration profiles within the tissue.

CITED LITERATURE

- [1] World Precision Instruments Inc., "UltraMicroPump III Instruction Manual", http://www.wpiinc.com/pdf/UMP3_IM.pdf.
- [2] Yokokawa, R., Saika, T., Nakayama, T., "Picoliter controllable syringes driven by parallel motions of electrostatic controlled linear inchworm actuator," *19th IEEE International Conference on Micro Electro Mechanical Systems*, 2006, pp. 798-801.
- [3] Yokokawa, R., Saika, T., Nakayama, T., "On-Chip Syringe Pumps for Picoliter-Scale Liquid Manipulation," *Lab Chip*, Vol. 6, No. 8, 2006, pp. 1062-1066.
- [4] Saika, T., Yokokawa, R., Fujita, H., "Direct Liquid Manipulation by Parallel Micro Syringe System for High Controllability with Pico-Liter Scale," *Solid-State Sensors, Actuators and Microsystems Conference*, 2007, pp. 1877-1880.
- [5] Wei, J., van der Velden, M., and Sarro, P. M., "Fabrication of Vertical Electrodes on Channel Sidewall for Picoliter Liquid Measurement," *Solid-State Sensors, Actuators and Microsystems Conference*, 2007, pp. 1613-1616.
- [6] Chang, L. Y., Li, P. Y., Zhao, L., "Integrated flow sensing for focal biochemical stimulation," *3rd IEEE International Conference on Nano/Micro Engineered and Molecular Systems*, 2008, pp. 921-926.
- [7] Liu, Y., Chen, L., and Sun, L., "Design and Fabrication of a MEMS Flow Sensor and its Application in Precise Liquid Dispensing," *Sensors*, Vol. 9, No. 6, 2009, pp. 4138-4150.
- [8] Min Hu, Lindemann, T., Gottsche, T., "Discrete Chemical Release from a Microfluidic Chip," *Journal of Microelectromechanical Systems*, Vol. 16, No. 4, 2007, pp. 786-794.
- [9] Thurow, K., Krüger, T., and Stoll, N., "An Optical Approach for the Determination of Droplet Volumes in Nanodispensing," *Journal of Automated Methods and Management in Chemistry*, Vol. 2009, No. Article ID 198732, 2009.
- [10] Nakatani, K., Sudo, M., and Kitamura, N., "A Study on Liquid-Liquid Distribution Based on Single Picoliter Droplets and in Situ Electrochemical Measurements," *Analytical Chemistry*, Vol. 72, No. 2, 2000, pp. 339-342.
- [11] Chiu, D. T., and Lorenz, R. M., "Chemistry and Biology in Femtoliter and Picoliter Volume Droplets," *Accounts of Chemical Research*, Vol. 42, No. 5, 2009, pp. 649-649-658.
- [12] Chiu, D. T., Lorenz, R. M., and Jeffries, G. D. M., "Droplets for Ultrasmall-Volume Analysis," *Analytical Chemistry*, Vol. 81, No. 13, 2009, pp. 5111-5118.

- [13] Lorenz, R. M., Edgar, J. S., Jeffries, G. D. M., "Microfluidic and Optical Systems for the on-Demand Generation and Manipulation of Single Femtoliter-Volume Aqueous Droplets," *Analytical Chemistry*, Vol. 78, No. 18, 2006, pp. 6433-6439.
- [14] He, M., Kuo, J. S., and Chiu, D. T., "Effects of Ultrasmall Orifices on the Electrogeneration of Femtoliter-Volume Aqueous Droplets," *Langmuir*, Vol. 22, No. 14, 2006, pp. 6408-6413.
- [15] He, M., Kuo, J. S., and Chiu, D. T., "Electro-Generation of Single Femtoliter- and Picoliter-Volume Aqueous Droplets in Microfluidic Systems," *Applied Physics Letters*, Vol. 87, No. 3, 2005, pp. 031916.
- [16] Corson, D. W., and Fein, A., "Quantitative Pressure Injection of Picoliter Volumes into Limulus Ventral Photoreceptors," *Biophysical Journal*, Vol. 44, No. 3, 1983, pp. 299-304.
- [17] Cai, X., Klauke, N., Glidle, A., "Ultra-Low-Volume, Real-Time Measurements of Lactate from the Single Heart Cell using Microsystems Technology," *Analytical Chemistry*, Vol. 74, No. 4, 2002, pp. 908-908-914.
- [18] Daoura M and Meldrum, D., "Precise Automated Control of Fluid Volumes Inside Glass Capillaries," Vol. 8, No. 1, 1999, pp. 71.
- [19] Rogers, R. C., "An Inexpensive Picoliter-Volume Pressure Ejection System," *Brain Research Bulletin*, Vol. 15, No. 6, 1985, pp. 669-671.
- [20] Puntambekar, A., Choi, J., Ahn, C. H., "Fixed-Volume Metering Microdispenser Module," *Lab on a Chip*, Vol. 2, No. 4, 2002, pp. 213-213-218.
- [21] Hosokawa, K., Fujii, T., and Endo, I., "Handling of Picoliter Liquid Samples in a Poly(Dimethylsiloxane)-Based Microfluidic Device," *Analytical Chemistry*, Vol. 71, No. 20, 1999, pp. 4781-4781-4785.
- [22] Steigert, J., Wangler, N., Brett, O., "Pico-injector for the discrete chemical stimulation of individual cells with a high temporal and spatial resolution," *4th European Conference of the International Federation for Medical and Biological Engineering*, Vol. 22, 2008, pp. 1434-1437.
- [23] Harris, D. L., and Mutz, M., "Debunking the Myth: Validation of Fluorescein for Testing the Precision of Nanoliter Dispensing," *Journal of the Association for Laboratory Automation*, Vol. 11, No. 4, 2006, pp. 233-239.
- [24] Young, I. T., Hjelt, K. T., Van, d. D., "Measuring liquid volumes in sub-nanoliter wells," *Biomedical Instrumentation Based on Micro- and Nanotechnology*, Vol. 4265, 2001, pp. 75-80.
- [25] Hjelt, K. T., van den Doel, R., Lubking, W., "Measuring Liquid Evaporation from Micromachined Wells," *Sensors and Actuators A: Physical*, Vol. 85, No. 1-3, 2000, pp. 384-389.

- [26] Lisec, T., Wagner, B., and Quenzer, H. J., "Microsensor for Measuring the Position of Liquids in Capillaries," US Patent No. 6,748,804, Application No. 10/088200, 2004.
- [27] Wei, J., Yue, C., van der Velden, M., "Design, Fabrication and Characterization of a Femto-Farad Capacitive Sensor for Pico-Liter Liquid Monitoring," *Sensors and Actuators A: Physical*, Vol. 162, No. 2, 2010, pp. 406-417.
- [28] Taylor, P. B., Ashman, S., Baddeley, S. M., "A Standard Operating Procedure for Assessing Liquid Handler Performance in High-Throughput Screening," *Journal of Biomolecular Screening*, Vol. 7, No. 6, 2002, pp. 554-569.
- [29] Melvad, C., Kruhne, U., and Frederiksen, J., "Design Considerations and Initial Validation of a Liquid Microflow Calibration Setup using Parallel Operated Syringe Pumps," *Measurement Science and Technology*, Vol. 21, No. 7, 2010.
- [30] Englmann, M., Fekete, A., Gebefugi, I., "The dosage of small volumes for chromatographic quantifications using a drop-on-demand dispenser system," *Focus on Sample Handling/Kinetics in Analytical Chemistry*, Vol. 388, No. 5-6, 2007, pp. 1109-1116.
- [31] Santiago, J. G., Wereley, S. T., Meinhart, C. D., "A Particle Image Velocimetry System for Microfluidics," *Experiments in Fluids*, Vol. 25, No. 4, 1998, pp. 316-319.
- [32] Cavallaro, A., and Saggere, L., "Picoliter fluidic flow characterization using ion-selective measurement," *2005 ASME International Mechanical Engineering Congress and Exposition*, Vol. 7 MEMS, 2005, pp. 117-122.
- [33] Gass, V., van, d. S., and de Rooij, N. F., "Nanofluid handling by micro-flow-sensor based on drag force measurements," *Proceedings of the 1993 IEEE Micro Electro Mechanical Systems - MEMS, February 7, 1993 - February 10, 1993*, pp. 167-172.
- [34] Su, C., Chen, T., and Yang, C., "Air piston calibrator for microflow delivery and measurement systems," *5th International Conference on Nanochannels, Microchannels and Minichannels*, 2007, pp. 731-738.
- [35] Szekely, L., Reichert, J., and Freitag, R., "Non-Invasive Nano-Flow Sensor for Application in Micro-Fluidic Systems," *Sensors and Actuators A: Physical*, Vol. 113, No. 1, 2004, pp. 48-53.
- [36] Matsuno, Y., Nakajima, M., Kojima, M., "Pico-liter injection control to individual nano-liter solution coated by lipid layer," *2009 International Symposium on Micro-NanoMechatronics and Human Science*, pp. 249-254.
- [37] Kawai, K., Fujii, M., and Shoji, S., "Precise titration microfluidic system using sub-picoliter droplet injection," *22nd IEEE International Conference on Micro Electro Mechanical Systems, MEMS 2009, January 25, 2009 - January 29, 2009*, pp. 519-522.

- [38] Reichmuth, D. S., Shepodd, T. J., and Kirby, B. J., "On-Chip High-Pressure Picoliter Injector for Pressure-Driven Flow through Porous Media," *Analytical Chemistry*, Vol. 76, No. 17, 2004, pp. 5063-5068.
- [39] Munson, B.R., Young, D.F., and Okiishi, T.H., "Fundamentals of Fluid Mechanics." John Wiley & Sons, Inc., 1998.
- [40] Sindhvani, N., Ivanchenko, O., Leushen, E., Linninger, A. A., "Methods for Determining Agent Concentration Profiles in Agarose Gel during Convection Enhanced Delivery," *IEEE Transactions on Biomedical Engineering*, Vol. 58, No. 3, 2011, pp. 626-627-632.
- [41] Chen, J., Wang, Q., Chen, S., "In Vivo Diffusion Tensor MRI of the Mouse Retina: A Noninvasive Visualization of Tissue Organization," *NMR in Biomedicine*, 2010.
- [42] Kirby, B.J., "Micro- and Nanoscale Fluid Mechanics: Transport in Microfluidic Devices." Cambridge University Press, 2010.
- [43] Dorf, R.C., and Svoboda, J.A., "Introduction to Electric Circuits." John Wiley & Sons, Inc., 2001.
- [44] Nicholas, A.; Burns, S.T.; Meiners, J.C.; Chen, H.; Kennedy, R.T., "Microfluidic chip for low-flow push-pull perfusion sampling in vivo with on-line analysis of amino acids," *Analytical Chemistry*, Vol. 77, No. 21, 2005, pp. 7067-7073.
- [45] Gabhann F.M., Demetriades, A.M., Deering, T., Packer J.D., Shah, S.M., "Protein Transport to Choroid and Retina following Periocular Injection: Theoretical and Experimental Study," *Annals of Biomedical Engineering*, Vol. 35, No. 4, 2007, pp. 615-630
- [46] Bohren, C. F. and Huffman, D. R., "Absorption and Scattering of Light by Small Particles." New York: Wiley, 1983.
- [47] Krauze et al. "Reflux-free cannula for convection-enhanced high-speed delivery of therapeutic agents," *Journal of Neurosurgery*, Vol. 103, No. 5, 2005, pp. 789-799.
- [48] Datta, A., and Rakesh, V., "An Introduction to Modeling of Transport Processes: Applications to Biomedical Processes." Cambridge University Press, 2010.
- [49] Rusakov, D. A., and Kullmann, D. M., "Extrasynaptic Glutamate Diffusion in the Hippocampus: Ultrastructural Constraints, Uptake, and Receptor Activation," *The Journal of Neuroscience*, Vol. 18, No. 9, 1998, pp. 3158.
- [50] Antcliff, R. J., Hussain, A. A., and Marshall, J., "Hydraulic Conductivity of Fixed Retinal Tissue After Sequential Excimer Laser Ablation: Barriers Limiting Fluid Distribution and Implications for Cystoid Macular Edema," *Archives of Ophthalmology*, Vol. 119, No. 4, 2001, pp. 539-544.

[51] Linninger, A. A., Somayaji, M. R., Erickson, T., "Computational Methods for Predicting Drug Transport in Anisotropic and Heterogeneous Brain Tissue," *Journal of Biomechanics*, Vol. 41, No. 10, 2008, pp. 2176-2187.

[52] Kim, H., Lizak, M. J., Tansey, G., "Study of Ocular Transport of Drugs Released from an Intravitreal Implant using Magnetic Resonance Imaging," *Annals of Biomedical Engineering*, Vol. 33, No. 2, 2005, pp. 150-164.

APPENDIX

A.1 Summary of Hydraulic/Electric Circuit Analogy

Table III - SUMMARY OF THE ELECTRICAL/HYDRAULIC CIRCUIT ANALOGY [42, 43]

Electric Circuit Analysis	Hydraulic Circuit Analogy
Basic Definitions	
Voltage or Potential, ϵ	Pressure Difference, ΔP
Current, I \xrightarrow{I}	Volumetric Flow Rate, Q \xrightarrow{Q}
Resistance, R 	Hydraulic Resistance, R_H 
Capacitance, C 	Hydraulic Capacitance, C_H 
Charge, q	Volume, V
Basic Relations	
$\epsilon = I \cdot R$	$\Delta P = Q \cdot R_H$
$I = C \cdot d\epsilon/dt$	$Q = C_H \cdot d\Delta P/dt$
Kirchoff's Current Law at a Node:	Flow Rate Law at a Node:
Kirchoff's Voltage Law for a Loop:	Pressure Difference Law for a Loop:
Resistors in Series:	Resistors in Series:
Resistors in Parallel:	Resistors in Parallel:
$\text{---} \quad \text{---}$	$\text{---} \quad \text{---}$
Capacitors in Series:	Capacitors in Series:
$\text{---} \quad \text{---}$	$\text{---} \quad \text{---}$
Capacitors in Parallel:	Capacitors in Parallel:

A.2 MATLAB code to run hydraulic circuit analysis

A.1.1 Full Hydraulic Circuit Model of the Syringe Pump Dispenser

```

%%% This function "dstate" defines all the circuit elements (resistors and
capacitors) in the hydraulic circuit and also defines the state equations
(the system of differential equations defined by the voltage at each node)
%%%

```

```

function dydt = dstate(t,y)

%% System Input %%
%Flowrate Input% units [m/s]
Velocity_input=71e-6;

%Flowrate Input% units [m^3/s]
Qplunger=(pi/4)*(460e-6)^2*Velocity_input*((1/(1+exp(-100*(t-.05)))-
1/(1+exp(-100*(t-.21)))));

%% System Constants %%
%Properties of water at room temperature
viscosity=9e-4; %units [Pa*s]
BulkModulus=2.2e9; %units [Pa]

%Elastic Moduli of conduits% units [Pa]
E_Barrel=6.2e10; %Borosilicate Glass
E_Needle=2e11; %Stainless Steel
E_Connector=3.28e9; %Ultem 1000 (plastic)
E_Capillary=7.3e10; %Fused Silica

%Radii of conduits% units [m]
r_Barrel=(460e-6)/2;
r_Needle=(165e-6)/2;
r_Connector=(250e-6)/2;
r_Capillary=(20e-6)/2;

%Length of conduits% units [m]
L_Barrel=0.01;
L_Needle=0.02;
L_Connector=0.00185;
L_Capillary=0.01;

%Hydraulic Resistances of conduits% units [kg/(s*m^4)] or [Pa*s/m^3]
R_Barrel=8*viscosity*L_Barrel/(pi*(r_Barrel)^4);
R_Needle=8*viscosity*L_Needle/(pi*(r_Needle)^4);
R_Connector=8*viscosity*L_Connector/(pi*(r_Connector)^4);
R_Capillary=8*viscosity*L_Capillary/(pi*(r_Capillary)^4);

%Hydraulic Capacitances of conduits% units [kg*m^2/s^2] or [m^3/Pa]

```

```

C_Barrel=L_Barrel*pi*(r_Barrel)^2*(1/BulkModulus+1/E_Barrel);
C_Needle=L_Needle*pi*(r_Needle)^2*(1/BulkModulus+1/E_Needle);
C_Connector=L_Connector*pi*(r_Connector)^2*(1/BulkModulus+1/E_Connector);
C_Capillary=L_Capillary*pi*(r_Capillary)^2*(1/BulkModulus+1/E_Capillary);

%% System of State Equations %%

% Preallocate the size of the vector for the number of ODEs
dydt = zeros(4,1);

% System of first order ODEs that describes the hydraulic system (enter in
the format that solves for dy/dt)
dydt(1) = Qplunger/C_Barrel-(y(1)-y(2))/(C_Barrel*R_Barrel);
dydt(2) = (y(1)-y(2))/(C_Needle*R_Barrel)-(y(2)-y(3))/(C_Needle*R_Needle);
dydt(3) = (y(2)-y(3))/(C_Connector*R_Needle)-(y(3)-
y(4))/(C_Connector*R_Connector);
dydt(4) = (y(3)-y(4))/(C_Capillary*R_Connector)-
y(4)/(C_Capillary*R_Capillary);

end

%% This function "call_dstate" calls up the "dstate" function and with an
input of the initial condition at each node and time steps and range to solve
over, the solution (pressure) is solved for at each node for each time
step%%

function [T,Y] = call_dstate()

% time range and step size with which the solution will be solved over
tspan = (0:0.0001:0.30);

% initial conditions of the pressures at each node (pressures equal zero at
t=0)
y0 = zeros(4,1);

%use ode15s numerical solver to solve the equations with defined variable in
"dstate"
[T,Y] = ode15s(@dstate,tspan,y0);

%plot the pressures at each node over time (note the output flow rate may be
solved for by dividing the voltage at the final node by the resistance of the
capillary)
hold on
plot(T,Y(:,1),'b.')
plot(T,Y(:,2),'r.')
plot(T,Y(:,3),'g.')
plot(T,Y(:,4),'k.')
xlabel('Time [s]');

```

```

ylabel('Pressure [Pa]');
title('Pressure at each node over time');

end

```

A.2.2 Simplified Hydraulic Circuit Model of the Syringe Pump Dispenser

```

%%% This function "sdstate" defines only the main circuit elements
(dispensing capillary resistor and syringe barrel capacitor) in the hydraulic
circuit and also defines the state equation (the single differential equation
for the single node in the circuit) %%%

function dydt = sdstate(t,y)

%% System Input %%
%Flowrate Input% units [m/s]
Velocity_input=71e-6;

%Flowrate Input% units [m^3/s]
Qplunger=(pi/4)*(460e-6)^2*Velocity_input*((1/(1+exp(-100*(t-.05)))-
1/(1+exp(-100*(t-.21)))));

%% System Constants %%
%Properties of water at room temperature
viscosity=9e-4; %units [Pa*s]
BulkModulus=2.2e9; %units [Pa]

%Elastic Moduli of conduits% units [Pa]
E_Barrel=6.2e10; %Borosilicate Glass

%Radii of conduits% units [m]
r_Barrel=(460e-6)/2;
r_Capillary=(5e-6)/2;

%Length of conduits% units [m]
L_Barrel=0.02;
L_Capillary=0.01;

%Hydraulic Resistances of conduits% units [kg/(s*m^4)] or [Pa*s/m^3]
R_Capillary=8*viscosity*L_Capillary/(pi*(r_Capillary)^4);

%Hydraulic Capacitances of conduits% units [kg*m^2/s^2] or [m^3/Pa]
C_Barrel=L_Barrel*pi*(r_Barrel)^2*(1/BulkModulus+1/E_Barrel);

%% System Equations %%
% ODE that describes the hydraulic system
dydt = Qplunger/C_Barrel-y/(C_Barrel*R_Capillary);

end

```

```

%% This function "call_sdstate" calls up the "sdstate" function and with an
input of the initial condition at the node and time steps and range to solve
over, the solution (pressure) is solved for at the node for each time step%%

function [T,Y] = call_sdstate()

% time range and step size with which the solution will be solved over
tspan = (0:0.0001:0.30); %

% initial conditions of the pressures at the only node
y0 = 0;

%use ode15s numerical solver to solve the equations with defined variable in
"dstate"
[T,Y] = ode15s(@sdstate,tspan,y0);

%plot the pressure at the final node over time (note the output flow rate may
be solved for by dividing the voltage at the final node by the resistance of
the capillary)
hold on
plot(T,Y,'k.')
xlabel('Time [s]');
ylabel('Pressure [Pa]');
title('Pressure at final node over time');

end

```

A.3 MATLAB code to run image processing and analysis

```

%% This program performs image processing on a collection of images
%% recorded in a video sequence. The image files may be saved with %%
similar
%% file names in the same folder so that they may be batch imported and
%% processed. The image processing done in this program includes:
%% conversion to grayscale double format, cropping, and rotation. Also
%% several filters are applied to the images that include a smoothing
%% spatial filter and a noise reduction temporal filter. Finally, the
%% image pixel intensities are converted into a concentration value via %%
the
%% Beer-Lambert Law and inversion of the matrix with a geometry %%
correcting
%% light path length term. The geometry correction term changes size %% over
%% time as the concentration profile grows, so appropriate tracking of %% the
%% profile front is also captured. The concentration profile along the
%% axial line is then plotted.

%%shows the path directory to the file in apostrophes
p = which('1nLPulses 500cycPerSec(no comp) 0342.jpg');

```

```

%%obtains the data of files with similar filenames in the above path
%%directory
filelist = dir([fileparts(p) filesep '1nLPulses 500cycPerSec(no comp)
*.jpg']);

%%builds an array of image files from the above directory
fileNames = {filelist.name}';

%%number of images equal to the number of image files in the list
nImages = length(fileNames);

%%This value is the resolution of the images
MicronPerPixel=1;

%%These are the values for cropping the image
RowStart=290;
RowEnd=RowStart+149;
ColStart=230;
ColEnd=ColStart+149;

%%This is the intensity value that will distinguish a concentration
%%wavefront corresponds roughly to a 5% increase in initial concentration
along
%%center line
WaveFrontLimit = 0.7800;

%%This is the number of frames in the set for the noise filter
NoiseSet = 10;

%%frame rate
frameRate=10; %in [frame/sec]

%%3-dimensional matrix (mrows X ncols X nImages) of all the images in
%%sequence
segmentedImageSequence = zeros(RowEnd-RowStart+1,ColEnd-ColStart+1,nImages);

%%% this for loop builds a 3-D matrix of 2D images (rows by columns) that
%%% are converted from RGB uint8 formats into grayscale double formats for
%%% manipulation with other cropping

for k = 1:nImages

    I = imread(fileNames{k}); %call current image
    I=rgb2gray(I);%Convert to grayscale
    I=im2double(I); %Convert to double format to allow mathematical
operations
    I = I(RowStart:RowEnd,ColStart:ColEnd); % Crop image
(RowStart:RowEnd,ColStart:ColEnd)
    %I = rot90(I,2); % Rotate by 2*90=180 degrees
with integer 2
    I = fliplr(I); % Flip the Image left to right
    segmentedImageSequence(:, :, k) = I; %add image to 3D-matrix

```

```

end

%%% Noise Filtering %%%

%%% This is the set of images that will be used for the noise filtering
FirstSetsegmentedImageSequence=zeros (RowEnd-RowStart+1,ColEnd-
ColStart+1,NoiseSet);

for j = 1:10

    %build a set of the first ten images pre-dispensing for noise filtering
    FirstSetsegmentedImageSequence(:, :, j) = segmentedImageSequence(:, :, j);

end

%%Define the standard deviation of the first frames for each pixel so that
%%each pixel will be filtered based on this value
STDsegmentedImageSequence=std(FirstSetsegmentedImageSequence, 0, 3);

%Define the initial intensity image before any dispensing was carried out
%(all concentrations will be dependent on the initial intensity in this
image)
I0=segmentedImageSequence(:, :, NoiseSet+1);

%%Apply Noise filters
for j = (NoiseSet+2):nImages

    m=1;
    while (m <= RowEnd-RowStart+1)
        n=1;
        while (n <=ColEnd-ColStart+1)
            %% if the value of the pixel intensity change (drop) between two
            %% images over time is not greater than the standard deviation of
the
            %% noise set, then set the pixel intensity value equal to the
            %% previous image. If it is greater than accept the value of
            %% the intensity
            if segmentedImageSequence(m, n, j) < segmentedImageSequence(m, n, j-
1)- STDsegmentedImageSequence(m, n);
                segmentedImageSequence(m, n, j)=segmentedImageSequence(m, n, j);
            else
                segmentedImageSequence(m, n, j)=segmentedImageSequence(m, n, j-
1);
            end
            n=n+1; %update column index
        end
        m=m+1;%update row index
    end

end

%%%%%%%%Spatial Smoothing and Filtering%%%%%%%%

```

```

%this filter uses conv2padded function that can be downloaded from here:
%http://www.math.ucla.edu/~getreuer/matlabimaging.html
for j = NoiseSet+2:nImages

    % Moving average filter
    WindowSize = 5;
    h1 = ones(WindowSize,1)/WindowSize;
    segmentedImageSequence(:, :, j) =
conv2padded(h1,h1, segmentedImageSequence(:, :, j));

    %%use this filter if spatially weighted averaging is desired
%     % A light smoothing filter
%     h = [1,1,1;
%         1,4,1;
%         1,1,1];
%     h = h/sum(h(:)); % Normalize the filter
%     segmentedConcentrationSequenceSmooth(:, :, j) =
conv2padded(segmentedConcentrationSequence(:, :, j), h);

end

%%%Converting Images TO Concentrations%%%

%Define the absorbtion constant (experimentally determined)
alpha =88; %%units [dB/(%wt*mm)]

%This is the molecular weight of the dye, Bromophenol Blue in these trials
molWt=669.96; %%units [g/mol]

%number of images to perform conversions on
jImages=nImages-NoiseSet-1;

%This loop finds the number of pixels (from the capillary to the edge of
% the concentration front) that should be used for the geometry correction
N=zeros(jImages,1);

for j = NoiseSet+2:nImages
    n=1;
    while segmentedImageSequence(1,n,j)< WaveFrontLimit
        n=n+1;
    end
    N(j)=n;
end

%This loop builds the path length geometry correction term that grows over
%time along with the size of the concentraion profile
Length=zeros(RowEnd-RowStart+1,ColEnd-ColStart+1,jImages);
for j = NoiseSet+2:nImages
    for k=1:N(j)
        for l=1:N(j)
            if k==l
                Length(k,l,j)=MicronPerPixel*0.001*(1^2-(k-0.5)^2)^0.5;
            end
        end
    end
end

```

```

        elseif l>k
            Length(k,l,j)=(MicronPerPixel*0.001*(l^2-(k-0.5)^2)^0.5)-
Length(k,l-1,j));
        elseif k>1
            Length(k,l,j)=0;
        end
    end
end

%%%Multiply the z "length" Matrix by 2 since there are two quarter shells
%%%to pass thru
for j = NoiseSet+2:nImages
    Length(:, :, j)=2*Length(:, :, j);
end

%%% this for loop builds a 3-D matrix of images that are converted from
%%% pixel intensity values to pixel concentration values based on the
%%% Beer-Lambert Law; this loop starts at the second image after the noise
%%% set since the first image used as the reference intensity

%%%3-dimensional matrix (mrows X ncols X nImages)
segmentedConcentrationSequence = zeros(RowEnd-RowStart+1,ColEnd-
ColStart+1,jImages);

%convert image to concentration by Beer-Lambert Law and add
%concentration image to 3D-matrix
for j = NoiseSet+2:nImages

    %concentration is converted from %wt to molarity [mM] aka [mmol/Litres]
    segmentedConcentrationSequence(1:N(j),1:N(j),j) =
(1000*1000/molWt*1/(alpha))*Length(1:N(j),1:N(j),j)\(-
log(segmentedImageSequence(1:N(j),1:N(j),j)./I0(1:N(j),1:N(j)))));
end

%build an axial position vector to plot the centerline concentration
z=zeros(RowEnd-RowStart+1);
for j = 1:(RowEnd-RowStart+1)
    z(j)=j-1;
end

%plot the concentraion profile along the axial line over time
for j = NoiseSet+2:nImages

    plot(z,segmentedConcentrationSequence(:,1,j),'g')
    hold on
end

%use this to play back videos
%implay(segmentedConcentrationSequence);

```

VITA

NAME: Brian Edward Kunzer

EDUCATION: B.S., Mechanical Engineering, University of Illinois at Chicago, Chicago, Illinois, 2004

B.S., Physics, University of Illinois at Chicago, Chicago, Illinois, 2005

M.S., Mechanical Engineering, University of Illinois at Chicago, Chicago, Illinois, 2011

TEACHING: Department of Mechanical Engineering, University of Illinois at Chicago, Chicago, Illinois: Teaching Assistant for Dynamics of Machinery, 2009-2010

PROFESSIONAL MEMBERSHIP: Biomedical Engineering Society (BMES)